

**THE FLUID HISTORY OF THE SEABEE
MESOTHERMAL GOLD DEPOSIT
NORTHERN SASKATCHEWAN**

**A Thesis Submitted to the College of
Graduate Studies and Research
in Partial Fulfilment of the Requirements
for the Degree of Master of Science
in the Department of Geological Sciences
University of Saskatchewan
Saskatoon**

By

Dale Joel Schultz

January 1996

©Copyright Dale Schultz, 1996. All rights reserved.

In presenting this thesis in partial fulfilment of the requirements for a Postgraduate degree from the University of Saskatchewan, I agree that the Libraries of this University may make it freely available for inspection. I further agree that permission for copying of this thesis in any manner, in whole or in part, for scholarly purposes may be granted by the professor or professors who supervised my thesis work or, in their absence, by the Head of the Department or the Dean of the College in which my thesis work was done. It is understood that any copying or publication or use of this thesis or parts thereof for financial gain shall not be allowed without my written permission. It is also understood that due recognition shall be given to me and to the University of Saskatchewan in any scholarly use which may be made of any material in my thesis.

Requests for permission to copy or to make other use of material in this thesis in whole or in part should be addressed to:

Head of the Department of Geological Sciences
University of Saskatchewan
Saskatoon, Saskatchewan S7N 0W0

Abstract

The Seabee deposit is a mesothermal, gold-bearing vein system hosted within mylonitic shear structures in the Glennie Domain of the Proterozoic Trans-Hudson Orogen, northern Saskatchewan, Canada. Field and underground observations indicate that shear structures nucleated at rheological contrasts at the contacts between felsic intrusive dykes, and mafic intrusive lithologies. High-grade ore is located where shear structures intersect to form zones of transtension or dilational jogs. Geochemical patterns for altered mylonites are similar to those of the primary lithologies.

Mafic host rocks proximal to the Seabee quartz veins have been altered to biotite, actinolite, epidote assemblages as the result of hydrothermal activity. Two stages of mineralization are present within quartz veins of the Seabee deposit. Stage I consists of quartz, tourmaline, K feldspar, and pyrite. Stage II is confined within microfractures that cut the Stage I assemblage. Stage II is dominated by carbonate, pyrrhotite, chalcopyrite, tellurides, and gold. Quartz adjacent to microfractures was locally recrystallized during the Stage II event. Gold is sited where Stage II microfractures intersect pyrite, whereas the microfractures that transect quartz contain only carbonate with trace quantities of chalcopyrite and tellurides. The occurrence of gold indicates that interaction of an auriferous fluid with Stage I pyrite resulted in gold deposition. In addition, gold blebs locally occur as linear arrays within pyrite proximal to Stage II microfractures, and are interpreted to represent Stage II gold grains about which Stage I pyrite recrystallized.

No primary fluid inclusions have been preserved in Stage I quartz veins, although numerous secondary inclusions are present. Secondary inclusions consist dominantly of $H_2O(g)-H_2O(l)$ or $CO_2(g)-CO_2(l)$; the occurrence of 3-phase $CO_2(g)-H_2O(g)-H_2O(l)$ is limited. Microthermometric analysis indicates that $H_2O(g)-H_2O(l)$ inclusions were trapped at 212 °C and at pressures of approximately 2.0 kb, suggesting that the Seabee vein system was emplaced at depths of 7.0 km.

Stage I barren quartz has $\delta^{18}O$ values of 8.4 - 8.9‰, whereas auriferous Stage II quartz has higher values of 10.0-10.6‰. Tourmaline is variably altered, particularly adjacent to Stage II microfractures. This alteration is reflected in the O-isotope compositions; in unaltered tourmaline the $\delta^{18}O$ is approximately 6.6‰, whereas in altered tourmaline $\delta^{18}O$ ranges from 7.2 to 7.8‰. The O-isotopic compositions of barren quartz and unaltered tourmaline are assumed to preserve the

primary isotopic composition of Stage I fluid. The average isotopic fractionation temperature for Stage I quartz-tourmaline pairs is 430 °C. The O-isotope composition of Stage II fluid is preserved by microfracture quartz and altered tourmaline. The average calculated isotopic fractionation temperatures for Stage II is 360 °C. Although the Stage I and II fluid events differed by 70 °C in temperature, the calculated $\delta^{18}\text{O}_{\text{H}_2\text{O}}$ values for both mineral pairs are in the 5.2 to 5.4‰ range.

The mineralization associated with Stage I and II crosscut all lithologies so that the $^{207}\text{Pb}/^{206}\text{Pb}$ zircon evaporation age of 1877 ± 10 Ma obtained from a late feldspar porphyry dyke provides an upper limit on the timing of hydrothermal activity. $^{40}\text{Ar}/^{39}\text{Ar}$ age spectra for hornblende, obtained from mafic rock lithologies, have disturbed patterns signifying that the minerals were reset, likely during the hydrothermal activity. Biotite from the alteration assemblage of the Seabee deposit has two different $^{40}\text{Ar}/^{39}\text{Ar}$ plateau ages of 1728 ± 5 Ma and 1769 ± 7 Ma. The 1769 Ma age is correlated with the Stage I event, whereas the 1728 Ma age may date the Stage II event. Younger step ages in both biotite spectra are associated with the distinctly younger fluid event.

The initial $^{87}\text{Sr}/^{86}\text{Sr}$ ratio of hydrothermal fluids from Stage I tourmaline is 0.702171 ± 23 , whereas $^{87}\text{Sr}/^{86}\text{Sr}_{\text{initial}} = 0.711093 \pm 87$ to 0.7078 ± 13 for Stage II sulphides and gold. These results imply that the Stage II gold bearing fluid was either tapping an older Archean source, or selectively leaching Rb-rich minerals of Paleoproterozoic age.

Collectively the field, petrographic, and geochemical results are consistent with the interpretation that the Seabee deposit is a structurally hosted mesothermal lode gold deposit, but not a sedimentary exhalative, or a copper-gold porphyry-type system.

Acknowledgements

I would like to acknowledge the members of my committee, R. Kerrich, T.K. Kyser, M. Reeves, L.C. Coleman, M. Stauffer, H. Hendry, Y. Pan, K. Ansdell, and B. Rostron, who supplied guidance, and support throughout this project.

I would especially like to acknowledge T. Sibbald, and G. Delaney from Saskatchewan Energy and Mines, who supplied both technical expertise and financial aid for this thesis.

Support from Claude Resources Inc. was highly valued, and I would like to thank the following personal past and present for their help; T. Hurley, G. Leniuk, D. Benard, H. Robertson, D. Dumaine, M. Eaid, G. Biles, R. Danielson, D. Moore, R. (Ned) Reid, G. Linassi, G. Billingsley, R. Gagnon B. McNeil.

In addition, I would like acknowledge the following people as they contributed greatly to the completion of this work; R. George, D. Pezderic, C. Swiney, K. Klassen, A. Vuletich, A. Bilanski, G. Zaluski, J. Jain, L. Xie, F. Fan, D. Chipley, K. Kotzer, M. Fayek, K. Ansdell, M. Innes, K. Richard, M. Rees, B. Novakovski. B. Morgan, S. Whittaker, K. Casidy, D. Wyman, M. Sun, J. Richards, D. O' Hanley, D. Hall, D. Greenwood, J. Douse (Thank you for giving me labs year after year, even though I never showed up for friday lab meetings), C. McCauig ("there is no Cam McCauig only a Cambell McCauig?"), B. Janser, P. Cashman, P. Field, Q. Xie, J. (Geo Joe) Dobrohoczki, K. Durocher, G. Koehler, T. Bonli, J. Fedorowich, D. Kasper, G. Bowers, T. Cadrin, M. Powell, D. Neilson, J. Hirst, B. Tuffs, B. Assmus, D. Kennard, E. Eberhardt, B. Benko, S. Gill, W. Gaskin, R. Feng, S. Matieshin, Dr. Zhu, J. Nyman, J. Long, B. Jellicoe, R. Bullis, F. Hrdy (who I would specially like to acknowledge as he always had a word of positive encouragement, and room in his apartment for me to crash), and any other members of the Ore Ganguer over the year, thanks for all the good times.

Finally, I would like to thank my family, Allen and Marilyn, and especially my Mother. For without their support none of this would be possible.

Table of Contents

Permission to use	i
Abstract	ii
Acknowledgements	iv
Table of Contents	v
List of Figures	vii
List of Tables	viii
List of Plates	ix
1.0 Introduction	1
1.1 History of the Seabee mine	1
1.2 Models for the Seabee deposit	3
1.3 Objectives and methodologies	5
2.0 Regional geology	6
2.1 Mesothermal gold deposits of the Trans-Hudson Orogen.	9
3.0 Local geology	14
3.1 General setting of the shear zones	14
3.2 Shear zones, alteration, and related host rocks	14
3.3 Structural controls for mineralization at Zone 2	18
3.3.0 Vein characteristics	19
3.3.1 Vein geometry	19
3.3.2 Hydrothermal mineralogy and paragenetic sequence	23
3.3.3 Gold precipitation mechanism	26
4.0 Protolith discrimination	28
4.1.0 Protolith discrimination	29
4.1.1 Cr vs. Zr and Hf	29
4.1.2 Cr vs. Al ₂ O ₃ - TiO ₂	30
4.1.3 Cr vs. Ni-Lu	33
4.1.4 Ni vs. Lu	33
4.1.5 REE, (La/Yb) _n and Lu	33
4.2 Discussion	36
5.0 Fluid inclusion characteristics	39
5.1 Petrography and inclusion type	39
5.2 Thermometric data	43
5.3 Interpretation of data	48

6.0	Isotope geochemistry	51
6.1	Stable isotopes	51
	6.1.1 Vein quartz	52
	6.1.2 Microfracture quartz	55
	6.1.3 Tourmaline	56
	6.1.4 Vein feldspar	57
	6.1.5 Carbonate	59
	6.1.6 Sulphides	61
6.2	Fluid events and fluids in equilibrium with minerals . .	63
6.3	Radiogenic isotopes	67
	6.3.1 Pb-Pb evaporation ages	67
	6.3.2 ⁴⁰ Ar/ ³⁹ Ar ages	68
	6.3.3 Initial strontium of hydrothermal vein phases	75
7.0	Ore genesis and fluid history of the Seabee gold deposit	79
7.1	Gold in the Glennie domain	83
7.2	Implications for exploration	85
REFERENCES		87
Appendix A: List of samples and locations		96
Appendix B: Fluid inclusion data from KRTA inc.		99
Appendix C: Analytical procedures		101
Appendix D: Summary of microprobe data		106
Appendix E: Summary of major and trace element data		108
Appendix F: Summary of trace element data for mineral seperates		114
Appendix G: Summary of fluid inclusion data		116
Appendix H: Summary of stable isotope data		118
Appendix I: Summary of radiogenic isotope data		121

List of Figures

Figure 1.1	Distribution of gold showings, and location of the Seabee deposit	2
Figure 2.1	Geological setting of the Pine Lake gold showings including the Seabee deposit	8
Figure 2.2	Geo-chronological history of the Seabee-Laonil Lake area	10
Figure 3.1	Geological map of the Seabee claim block	15
Figure 3.2	Ruptured units demonstrating non-coaxial deformation	17
Figure 3.3	Seabee Mine longitudinal section	20
Figure 3.4	Geological map of the 170 m level	21
Figure 3.5	Geological map of the 325 m level	22
Figure 3.6	Mineral paragenesis of the Seabee deposit	24
Figure 4.1-4.2	Discrimination plot of Cr vs. Zr and Hf	31
Figure 4.3-4.4	Discrimination plot of Cr vs. TiO_2 and Al_2O_3	32
Figure 4.5-4.6	Discrimination plot of Cr vs. Ni and Lu	34
Figure 4.7-4.8	Discrimination plot of Ni vs. Lu and REE patterns of various lithologies	35
Fig. 4.9-4.10	Discrimination plot of Cr vs. $(La/Yb)_n$ and Lu vs. $(La/Yb)_n$	37
Figure 5.1	Summary of fluid inclusion data from the Seabee deposit	42
Figure 5.2	Histogram of low temperature data for Type Ia and Type Ic fluid inclusions	44
Figure 5.3	Histogram of homogenization and low temperature data for Type Ib inclusions	45
Figure 6.1	Histogram of $\delta^{18}O$ values for quartz from various structures within the Seabee claim block	54
Figure 6.2	Histogram of $\delta^{18}O$ values of unaltered and altered tourmaline from the Seabee deposit	58

Figure 6.3	Histogram of $\delta^{34}\text{S}$ values for various sulphide phases from the Seabee deposit	62
Figure 6.4	Relation between $\delta^{18}\text{O}_{\text{H}_2\text{O}}$ and $\delta\text{D}_{\text{H}_2\text{O}}$ values of minerals at the Seabee deposit	66
Figure 6.5	Results of $^{40}\text{Ar}/^{39}\text{Ar}$ analyses of amphiboles for the Laonil Lake Intrusive Complex	69
Figure 6.6	Results of $^{40}\text{Ar}/^{39}\text{Ar}$ analyses of amphiboles for the Laonil Lake Intrusive Complex	70
Figure 6.7	Results of $^{40}\text{Ar}/^{39}\text{Ar}$ analyses of alteration biotite from Zone 5 of the Seabee deposit	71
Figure 6.8	Results of $^{40}\text{Ar}/^{39}\text{Ar}$ analyses of biotite from the alteration envelope around Zone 2 of the Seabee deposit	72
Figure 7.1	Temperature-time path of the Seabee deposit	82
Figure 7.2	Dependence of $K_{\text{Au}(\text{HS})_2^-}$ with temperature	84

List of Tables

Table 6.1	List of stable isotope fractionation factors	53
Table 6.2	Table of fluid events for the Seabee deposit	64
Table 6.3	Sample Rb/Sr calculation of fluids in equilibrium with Archean crust and Proterozoic K^+ bearing phases	77

List of Plates

Plate 3.1	Photomicrographs and back scattered electron images of mineral phases within the quartz dominated portion of the vein	25
Plate 3.2	Photomicrographs and back scattered electron images of mineral phases within the sulphide dominated portion of the vein	27
Plate 5.1	Fluid inclusions in quartz vein	40

1.0 Introduction

1.1 History of the Seabee mine

The region containing the Seabee deposit was first staked, trenched, and drilled by Consolidated Mining and Smelting Company of Canada Ltd. (CMSA) from 1947 to 1950 (Figure 1.1). CMSA, which became Cominco, completed further diamond drilling assessment work on the property in the mid 1960's. From the 1960's to the 1980's the property received no investigation. In 1984, Claude Resources purchased the property from Cominco and continued with additional drilling. In 1985 Claude Resources announced proven and probable reserves for Zones 2, 5, 11, and 14 of 561,548 tonnes grading 11 g/tonne gold to a depth of 182 metres (The Northern Miner, 1985). Possible reserves from 182 metres to a depth of 305 metres were estimated to be 454,000 tonnes at 11 g/tonne gold (Delaney, 1992).

In 1985 Placer Developments optioned the property, and by 1987 had completed outcrop stripping, trenching, mapping, and diamond drilling. Placer Developments estimated reserves to a depth of 366 metres at 1,982,240 tonnes grading 6.3 g/tonne gold, with high-grade reserves of 739,700 tonnes at 12.5 g/tonne gold (Northern Miner, 1987). Over 900 metres of underground development and 6200 metres of underground drilling were completed before the end of 1988. In 1988, Placer Developments terminated the joint venture agreement,

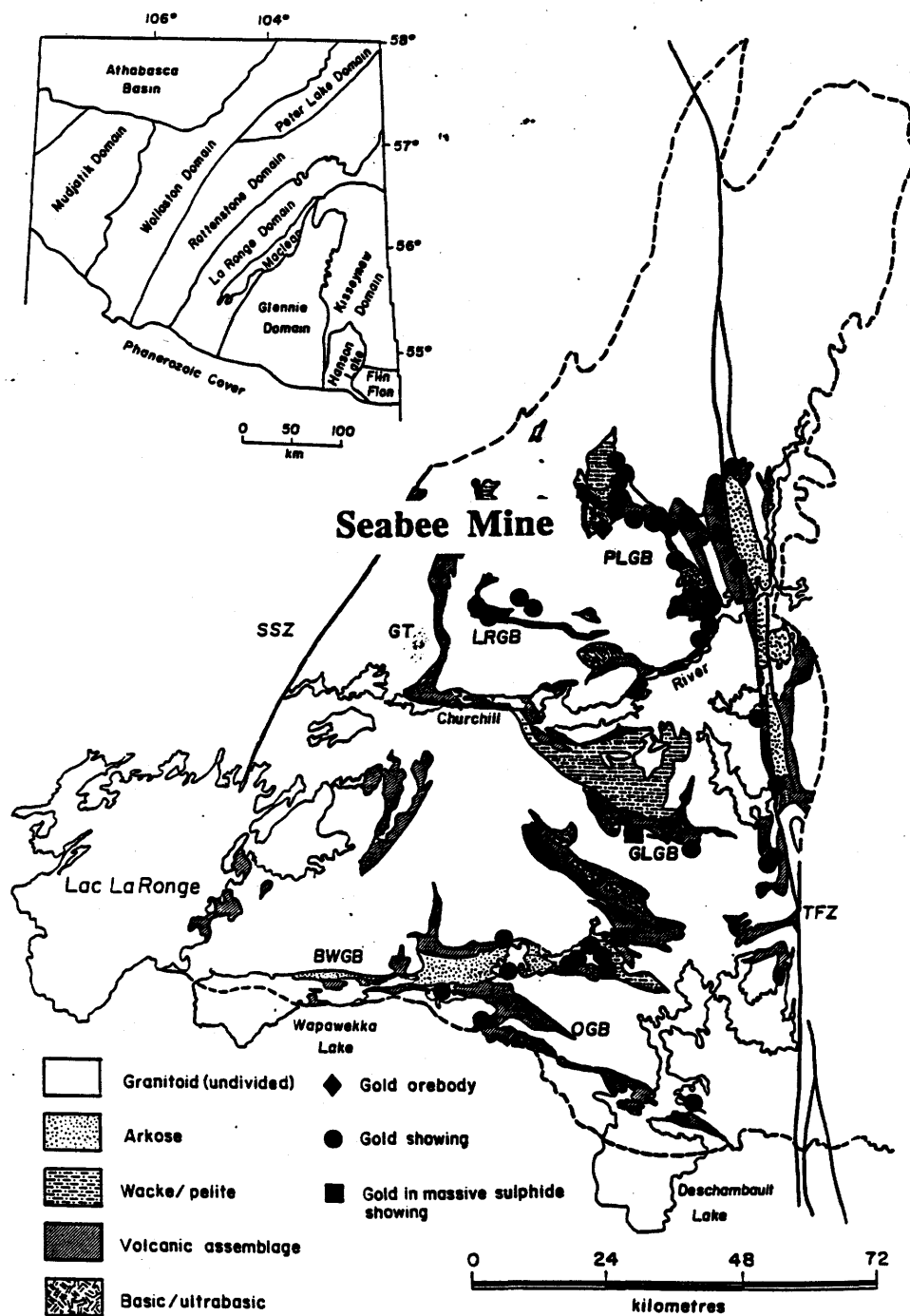


Figure 1.1 - Location of the Seabee Deposit, and distribution of gold showings in the Glennie Domain in relation to supracrustal assemblages and basic intrusions. In areas where there is a high density of showings, individual dots represent more than one showing. GT=Guncoat Thrust; LRGB=Leland-Robison Lake Greenstone Belt; PLGB =Pine Lake Greenstone Belt; GLGB=Gee Lake Greenstone Belt; BWGB=Brownell-Wapawekka Lakes Greenstone Belt; TFZ=Tabernor Fault Zone; SSZ=Stanley Shear Zone. Insert map shows lithostructural domains in the southeastern part of the Precambrian Shield of Saskatchewan (from Delaney, 1992).

and Claude Resources proceeded with development of the property.

In 1988, ACA Howe International Ltd. was commissioned to complete an ore reserve study; ACA Howe International concluded that Zones 2 and 5 contained an estimated proven ore reserve of 585,135 tonnes having an average grade of 12.5 g/tonne, with possible reserves of 332,937 tonnes grading 12.5 g/tonne gold (Delaney, 1992).

Cominco Engineering Services Ltd (CESL). was commissioned in 1987 to undertake an additional 3960 metres of drilling, 300 metres of sill development, and collection of a bulk sample. CESL reported a reserve of 1.04 million tonnes grading 13.7 g/tonne gold (Delaney, 1992). Based on these results, Claude Resources announced a decision to proceed with production on May 15, 1990. Following a period of mill construction, production commenced in November of 1991. Unfortunately, projected grades and tonnes of the CESL study were not realized, although ongoing underground and surface exploration continues to expand the ore reserve. Presently the mine produces at a rate of 5,000 oz (150,000 grams) of gold per month, and the deposit has yielded over 165,000 oz (3,100,000 grams) of gold prior to the end of the 1994 fiscal year, making the Seabee Mine the second largest gold producer in northern Saskatchewan. The region still contains sites of future potential ore development (e.g. Santoy Lake and Pine Lake)

1.2 Models for the Seabee deposit

A variety of genetic models have been proposed for the Seabee deposit. These are summarized as follows:

- (1) Mesothermal Gold Model: Lewry (1977), Schultz (1990),

Schultz and Kerrich (1991), and Delaney (1992), suggested that an anastomosing network of shear zones, with associated quartz veins represents a mesothermal gold deposit similar to deposits located in the Paleoproterozoic La Ronge domain (cf. Ibrahim and Kyser, 1991; Fayek et al., 1993; Thomas, 1993; Hrdy, 1994) and Flin Flon domain (Fedorowich et al., 1991; Ansdell and Kyser, 1992).

- (2) Lamprophyre model: Mafic dykes containing elevated gold values have been observed in drill core, and some of these are partly altered to biotite. Placer Dome classified these as lamprophyres, consistent with a lamprophyre associated gold deposit model such as proposed by Rock and Groves (1988).
- (3) Porphyry, orthomagmatic model: Felsic intrusions, termed quartz feldspar porphyries (QFP) in mine nomenclature, are also proximal to shear structures. These felsic units are known to have alteration halos consisting of pyrite with elevated gold values, and potassic alteration (Helmstaedt, 1986). Based on these field relationships, Helmstaedt (1986) suggested that the Seabee represents a porphyry magmatic style of mineralization (cf. Burrows et al., 1986; Cameron and Hattori, 1987).
- (4) Sedimentary exhalative model: Biotite, garnet, staurolite rich rocks near or within shear zones (Zone 5 and East Boundary Zone) led previous workers (Gummer, personal communication) to suggest a synvolcanic sedimentary exhalative gold deposit model for the Seabee (cf. Hutchinson and Burlington, 1984).

1.3 Objectives and Methodologies

To resolve the conflict between these models and establish a potentially viable genetic model for Seabee, this project was designed in four parts: (1) observations of geological field relationships, (2) determination of the structural controls on mineralization, (3) development of a vein paragenetic scheme for the deposit, and (4) determination of the fluid history of the deposit, utilizing trace-element geochemistry, fluid inclusion thermometry, and stable and radiogenic isotope systematics. Collectively, the data will be interpreted in order to assess the Pressure-Temperature-time-fluid history of the Seabee deposit.

2.0 Regional geology

The Trans-Hudson Orogen (Hoffman, 1981; Hoffman, 1990; Lewry and Collerson, 1990) can be divided into two distinctive zones; (1) The Cree Lake Zone, and (2) The Reindeer Zone (Stauffer, 1984). The Cree Lake Zone is composed of Paleoproterozoic miogeoclinal meta-sedimentary rocks unconformably overlying Archean gneisses. The Reindeer Zone consists mainly of mid-oceanic ridge basalts (MORB), oceanic island-arc basalts, inter-arc volcanogenic sedimentary rocks, and molasse-type sedimentary rocks; this supracrustal sequence was then intruded by plutonic rocks of various ages. All units contained within the Reindeer Zone were deformed and metamorphosed during the Hudsonian Orogeny.

The Reindeer zone is commonly subdivided into various lithotectonic domains (see inset on upper left hand corner of Figure 1.1) based on similarities of lithology, metamorphic grade and structure (Lewry and Sibbald, 1977). These include such domains as the La Ronge, Flin Flon, Glennie, Hanson Lake block, and Kisseynew. Archean rocks, or inliers, occur only within the Glennie domain (Chiarenzelli et al., 1987) and the Hanson Lake block (Bell and Macdonald, 1982; Craig, 1989).

Lewry et al., (1990) suggested that the Reindeer zone consists of folded stack of nappes, or thrust complexes, divided by ductile mylonitic zones, which were emplaced during the Trans-Hudson Orogen. This interpretation and interpretation of recent lithoprobe investigation implies that the zone is

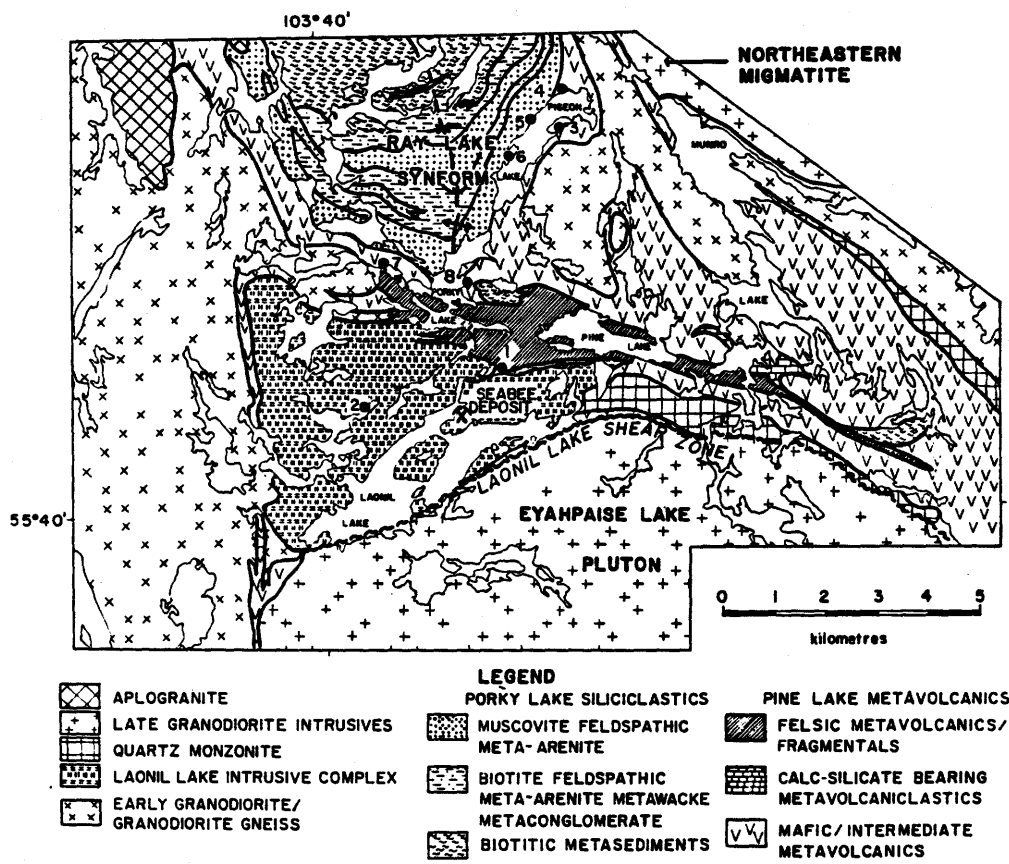


Figure 2.1 - Geological setting of the Seabee Deposit in the northern part of the Pine Lake Greenstone Belt. Numbered dots are locations of other gold showings: Currie Rose (1); Northwest Laonil Lake (2); P-1 (3); P-2 (4); P-3 (5); P-4 (6); PL-1 (7); PL-2 (8) (from Delaney, 1986).

underlain in part by Archean rocks (Lewry et al., 1990; Bickford et al., 1990; White et al., 1994).

The Glennie domain (Figure 1.1) is characterized by belts of Paleoproterozoic supracrustal rocks in a dominantly granitoid terrane. Two major structural breaks, the Stanley Shear Zone (SSZ), and the Tabbernor Fault Zone (TFZ), separate the Glennie domain from the neighbouring La Ronge and Kisseynew domains, and the Hanson Lake block (see Figure 1.1). The Seabee deposit is located in the north-central portion of the Glennie domain (Figures 1.1 and 2.1) within a mafic intrusive complex known as the Laonil Lake Intrusive Complex (Delaney, 1986).

The Seabee deposit is hosted in north-east trending shear structures within the Laonil Lake Intrusive Complex (Lewry, 1977; Gummer, 1986; Delaney, 1986). Within the mine claim block (Figure 2.1), the Laonil Lake Intrusive Complex consists of a sequence of mafic intrusive layers or sheets commonly capped by dioritic unit. A sample of the dioritic phase was dated by zircon U/Pb at 1889 ± 9 Ma (Chiarenzelli, 1989), thereby placing an upper age constraint on the timing of emplacement of the intrusive body. Mafic layering within the Laonil Lake Intrusive body varies from melanocratic gabbro to ultramafic in composition (Delaney, 1992). Intercalated rafts or xenoliths of mafic volcanic rocks, volcanoclastic rocks, and mafic to intermediate sedimentary units of variable thickness occur throughout the intrusive body (Delaney, 1992). Based on similar compositions and textures, these units may be considered equivalent to the mafic - intermediate volcanic sequence of Assemblage A of the Pine Lake metavolcanic sequence (cf. Delaney and Cuttler, 1992). Numerous later intermediate to felsic intrusive phases occur throughout the mafic intrusive body. These include intermediate dykes, quartz dioritic dykes, and feldspar porphyries dykes.

North and north-east of the Seabee deposit the Laonil Lake Intrusive Complex is unconformably overlain by felsic volcanic-volcaniclastic rocks and conglomerates of Assemblage B of the Pine Lake Group (cf. Delaney and Cutler, 1992). To the west, the intrusive complex is bounded by a sequence of earlier granodioritic to dioritic gneisses, and to the south by the younger (1859 ± 5 Ma) Eyahpaise granodioritic pluton (Van Schums *et al.*, 1987). A regional high strain zone, the Laonil Lake Shear Zone, occurs along part of the contact between the Eyahpaise Pluton and the Laonil Lake Intrusive Complex (Figure 2.1; Delaney, 1986). The geo-chronological history of the Seabee area is summarized in Figure 2.2.

In the northern part of the Glennie domain, the metamorphic grade is generally mid-amphibolite facies (Reese, 1982) and rarely granulite facies, whereas in the Laonil Lake region the rocks have lower amphibolite facies metamorphic assemblages. For rocks of the Ray Lake Synform, north of the mine, Lewry (1977) suggested that the mineral assemblages is indicative of the andalusite-cordierite-muscovite sub-facies of lower amphibolite facies metamorphism.

2.1 Mesothermal gold deposits of the Trans-Hudson Orogen.

The geological and geochemical characteristics of mesothermal gold deposits within the La Ronge Glennie and Flin Flon domains of the Trans-Hudson Orogen have been documented by several authors (Kyser *et al.*, 1986; Fedorowich *et al.*, 1991; Ibrahim and Kyser, 1991; Ansdell and Kyser, 1992; Delaney, 1992; Durocher *et al.*, 1992; Fayek *et al.*, 1993; Thomas, 1993; Hrdy, 1994). These vein deposits, in medium to high-grade metamorphic terranes, are typically hosted by shear zones. Trans-Hudson shear-zone hosted gold deposits are generally characterised by brittle-ductile deformation features, contain limited enrichment in base metals (Cu, Pb, Zn), and moderate

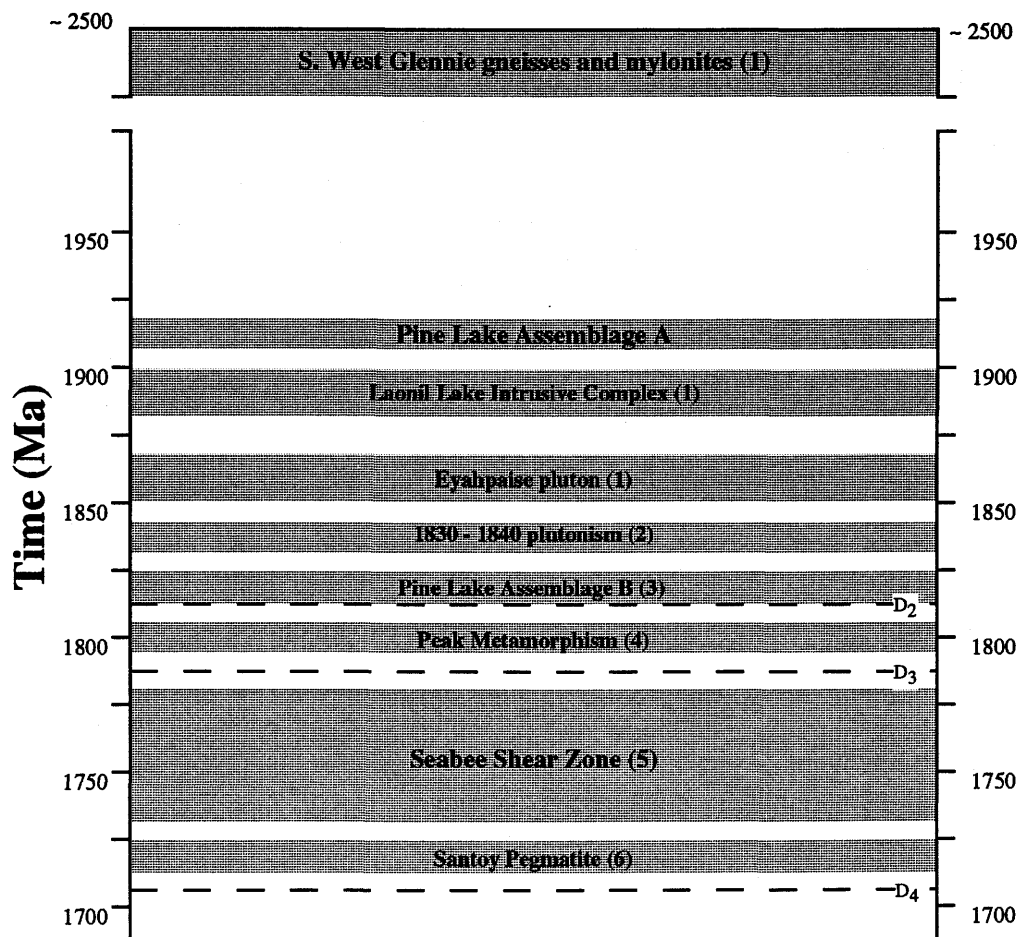


Figure 2.2 - Geo-chronological history of the Seabee-Laonil Lake region. References: (1) U-Pb zircon, Chiarenzelli, 1989; (2) U-Pb zircon, cf. Durocher, et al., 1993; (3) U-Pb zircon, Mc Nicoll, et al., 1992; (4) U-Pb monazite, Chiarenzelli, 1989; (5) Ar-Ar biotite, see chapter 6; (6) Pb-Pb zircon, Durocher, et al., 1993. D₂, D₃, D₄ as described by Durocher, et al., 1993.

enrichment in gold or gold and silver. Overall these vein systems are mineralogically dominated by quartz, chlorite, albite, potassium feldspar, tourmaline, biotite, muscovite, sericite, carbonate, and pyrite assemblages with accessory chalcopyrite, sphalerite, arsenopyrite, galena, tellurides, pyrrhotite and gold. Mineralizing fluids are characterised by lithostatic fluid pressures of less than 3 kb, moderate to low salinities (< 14.7 wt.% NaCl), $\delta^{18}\text{O}_{\text{water}} = 5$ to $9^\circ/\text{‰}$, $\delta\text{D}_{\text{water}} = -40$ to $-86^\circ/\text{‰}$, and ambient mineralizing temperatures of 300 to 550 °C (Kyser *et al.*, 1986; Fedorowich *et al.*, 1991; Ibrahim and Kyser, 1991; Ansdell and Kyser, 1992; Fayek *et al.* 1993; Hrdy, 1994).

In general, mesothermal deposits in the Paleoproterozoic Trans-Hudson are similar in style to Archean counterparts (cf. Kerrich and Allison, 1978; Kerrich and Fyfe, 1981; Kerrich, 1989a), although there are some differences. Historically, Trans-Hudson deposits tend to be small, averaging less than 1,000,000 tonnes, whereas Archean deposits may exceed 10,000,000 tonnes. Wyman and Kerrich (1988) have addressed this size differential by suggesting there exists a distinct tectonic regime in the context of the supercontinent cycle operating in the late Archean (2.7 - 2.6 Ma), but not during the early Archean or the Proterozoic. Notwithstanding the above possible tectonic distinctions, there is one large gold producer in the Paleoproterozoic, i.e. the Homestake deposit of the Black Hills, S. Dakota (Rye and Rye, 1974). The smaller tonnage deposits found in northern Saskatchewan may be a function of a shorter exploration history and less money spent on exploration, as compared to the well-explored Archean terranes of the Superior and Slave Provinces.

Many researchers have suggested that gold precipitation in Archean mesothermal deposits is predominantly early in the vein history (cf. Kerrich, 1989a), i.e. contemporaneous with

main-stage quartz vein deposition. Within the Trans-Hudson there appears to be two stages of gold mineralization. The Star Lake (La Ronge domain) and Tartan Lake deposits (Flin Flon domain) are examples of early stage gold deposition associated with main-stage quartz-chlorite-tourmaline-carbonate-albite precipitation (Fedorowich et al., 1991; Ibrahim and Kyser, 1991). In contrast, Contact Lake and Jasper deposits are examples of late-stage mineralization, and are characterized by paragenetic late assemblages consisting of recrystallized microfracture quartz-muscovite-pyrite-sphalerite-chalcopyrite-galena-gold (Fayek et al., 1993; Hrdy, 1994).

The two stages are similar in O - isotope compositions ($\delta^{18}\text{O}_{\text{H}_2\text{O}} = 5.0$ to 9.0‰), but can differ by as much as 20‰ in H - isotope composition, and by approximately 100 °C in calculated temperature. Calculated oxygen isotope temperatures of fluids associated with the main stage at Star Lake and Tartan Lake deposits range from 370 to 550 °C (Fedorowich et al., 1991; Ibrahim and Kyser, 1991), whereas the late-stage fluids at Contact Lake and Jasper deposits are typically 300 to 350 °C (Fayek et al., 1993; Hrdy, 1994).

The two stages also differ in absolute timing. At the Star Lake deposit, Ibrahim and Kyser (1991) dated the early stage gold mineralization utilizing a Rb/Sr two point isochron method (feldspar-tourmaline), and obtained an age of 1742 ± 87 (Ibrahim and Kyser, 1991). Ages of 1791 ± 4 Ma were obtained from $^{40}\text{Ar}/^{39}\text{Ar}$ analysis on early stage muscovite for the Tartan Lake deposit (Fedorowich et al., 1991). Conversely, at the Jasper and Contact Lake deposits the gold precipitation is paragenetically late (Fayek et al., 1993; Hrdy, 1994). $^{40}\text{Ar}/^{39}\text{Ar}$ analysis on late stage muscovite from both deposits produced ages of ca. 1720 , and model $^{87}\text{Rb}/^{86}\text{Sr}$ ages of ca. 1710 to 1730 Ma (Fayek et al., 1993; Hrdy, 1994). Elsewhere within

the La Ronge domain, younger age dates of 1719 ± 5 Ma were also obtained from $^{40}\text{Ar}/^{39}\text{Ar}$ plateaus on biotites from the Rush Lake veins (Kyser et al., 1992).

In summary, the gold mineralization in the Paleoproterozoic Trans-Hudson can be characterised by two distinct fluid events differing by approximately 100 °C in temperature, and by 20 to 70 Ma in timing, with gold deposition being associated with both events.

3.0 Local geology

3.1 General setting of the shear zones

Lewry (1977) suggested that the Laonil Lake Intrusive Complex was trapped, during deformation, between the core of the Ray Lake Synform and the rising Eyahpaise diapir, thus acting as a resistant mass similar to a mega-porphyroblast. In this strain regime as will be shown below, the Laonil Lake Intrusive Complex experienced both flattening (pure shear) and non-coaxial deformation (simple shear) concentrated along the margin of the intrusion, and along zones of internal weakness (Seabee Shear Structure). Thus, in addition to pure shear there is a simple shear component in the deformation history of the Laonil Lake Intrusive Complex.

3.2 Shear zones, alteration, and related host rocks

Seabee gold mineralization is hosted within the extensive network of anastomosing sub-parallel shear structures, Seabee Shear Structure, which crosscut the Laonil Lake Intrusive Complex. These structures strike between 045° and 085° , and most dip sub-vertically or steeply north (Figure 3.1). Three discrete sub-sets of structures have been recognized, trending at 070° , 085° , and 045° respectively. The 070° structures contain the auriferous veins (Zones 2B-2C, 5-1, and 161), whereas the 045° and 085° structures contain only sub-economic to barren vein systems (Zones 20, 15, 14 or 2H, 666, and East Boundary Zone).

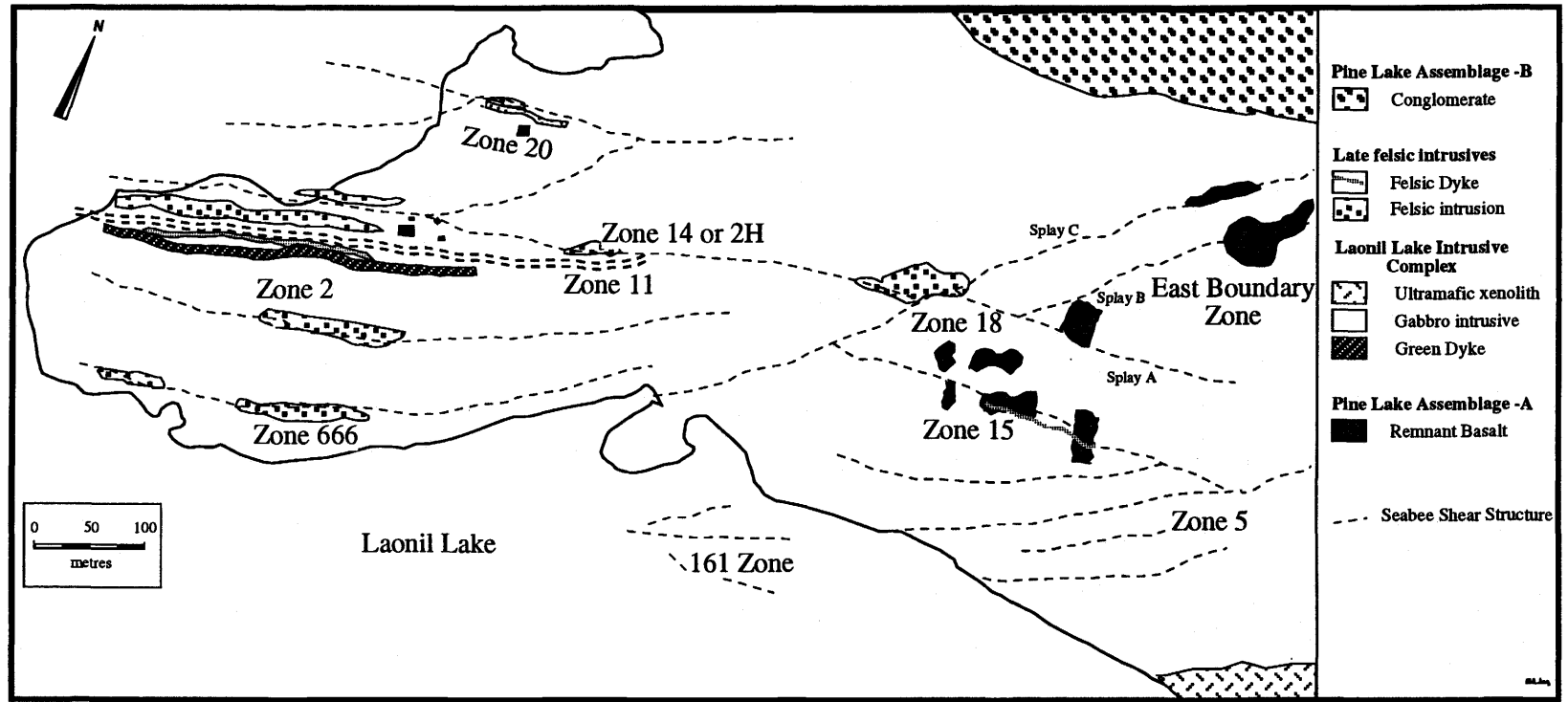


Figure 3.1 - Simplified geological map of the Seabee deposit showing distribution of major lithological units and shear structures.

Felsic-feldspar porphyritic dykes, and dioritic, intermediate, and mafic dykes occur in proximity to many of the major structures. Based on these close spatial geometric relationships, Delaney (1992) suggested that lithological heterogeneities between the feldspar porphyries and gabbros of the Laonil Lake Intrusive Complex were responsible for the formation and propagation of the shear zones at Seabee (Seabee Shear Structure).

According to Helmstaedt (1986, 1987), the Laonil Lake Shear Zone and Seabee Shear Structure were dominated by coaxial deformation, or pure shear; this interpretation stems from the absence of any clear kinematic indicators of simple shear (i.e. S-C fabrics). Structural studies in other areas (Lister and Snoke, 1984) have demonstrated that many mylonites formed in proximity to lithological boundaries, such as a pluton margin, are dominated by coaxial deformation.

Subsequent field observations determined that disrupted gabbros or mafic dykes in the vicinity of Zone 20 experienced non-coaxial deformation (Schultz, 1990). Adjacent to Zone 20, many fragments show progressive flattening and rotation passing into the deformational zone in accordance with a component of simple shear (Figure 3.2). Within the mafic host rocks an intense mineral stretching lineation, defined by the preferred dimensional and crystallographic alignment of hornblende and biotite, pitches at 80° to the west in the plane of the shear, and implies a dip-slip component to the Seabee Shear Structure.

Progressive changes in both grain size and mineralogy occur from the least-deformed lithologies to the most-deformed and metasomatized counterparts. The changes can be described in terms of four basic stages, although there is a continuous

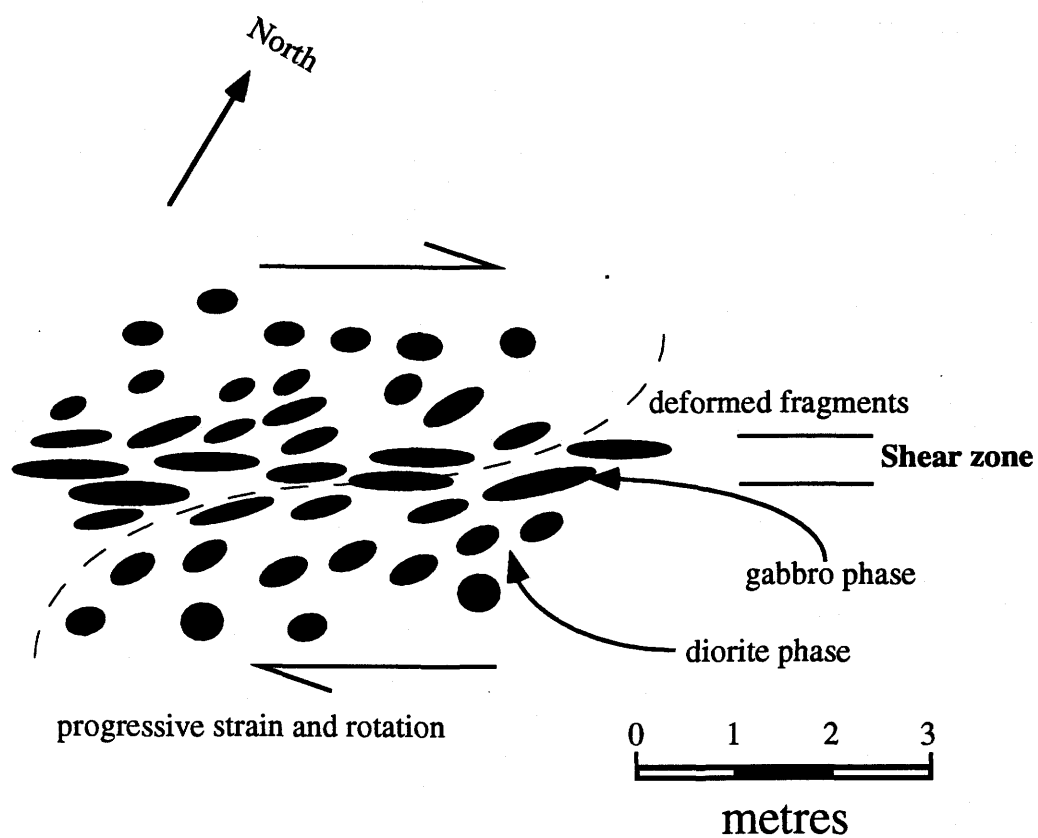


Figure 3.2 - Ruptured unit within Seabee Shear Structure showing progressive strain and rotation of fragments (i.e. non-coaxial deformation)

transition between them.

- (1) External to the shear zone: The gabbro and diorite units are massive (grain size $>500 \mu\text{m}$) and are mechanically isotropic, being relatively undeformed with little or no biotite alteration.
- (2) Margins of shear zone: Gabbro and diorite units are characterised by a pronounced decrease in grain size (300 to $200 \mu\text{m}$) and the rocks have developed a biotitic foliation.
- (3) Within shear zone: A biotite-actinolite-epidote-chlorite-carbonate alteration assemblage has developed along with a moderate to intense biotitic foliation.
- (4) Shear zone core: Segregated mafic (hornblende-actinolite-epidote-chlorite-biotite) and felsic (quartz-muscovite-feldspar) alteration assemblages are developed having an ultrafine-grained mylonitic fabric ($50 - 100 \mu\text{m}$). In rare instances hydrothermal staurolite and garnet may be developed within the mylonite.

3.3 Structural controls for mineralization at Zone 2

Significant exploration and development in the form of diamond drilling, surface, and underground mapping has been completed at Zone 2 (Figure 3.1). Consequently, the geometry and structural controls for mineralization have been well documented. Zone 2 strikes at 070° , and is continuous over a strike length of 650 metres, consisting of four sub-parallel shear structures, named 2A, 2B, 2C, and 2H respectively. These structures dip steeply to the north, and collectively have a maximum thickness of 11.5 metres, where individual shear zone locally range from 3 to 6 metres in width. The main ore body, the 2B structure, is mineralized over a strike length of 400

metres. On the surface, between mine northing of 1150 and 1250, the 2B structure splays into two separate shear structures, the 2B and 210B structures (Figures 3.3, 3.4, and 3.5).

The site of the splay-intersection represents an important location for ore formation. The shear zone thickness exceeds 5 metres at the splay-intersection, where it forms a continuous ore shoot plunging at 75° west from the surface to a depth of 400 metres. Relatively large tonnage and considerable gold production (>40,000 oz.) have been realised from this ore shoot.

Underground mapping indicates that the geometry of the splay intersection conforms to that of a deflection in the orientation of the shear structure (Figures 3.4 - 3.5). The splay-intersection probably occurs at a dilational jog, or a site of transtension along the main 070° structure. During deformation the permeability and hydraulic conductivity along the intersection would have been enhanced, allowing for significant volumes of fluid to pass up it, thereby forming the early mineralization assemblage of the deposit.

3.3.0 Vein characteristics

3.3.1 Vein Geometry

Both auriferous and barren quartz veins occur within the Seabee Shear Structure. Veins are moderately to strongly deformed, and many are isoclinally folded with the hinge lines plunging 80° west, parallel to the mineral stretching lineation. Veins are also elongate with an easterly plunge of 45-60° (Delaney, 1992). Only one stage of quartz veining appears to have occurred.

According to Delaney (1992), quartz veining formed prior to

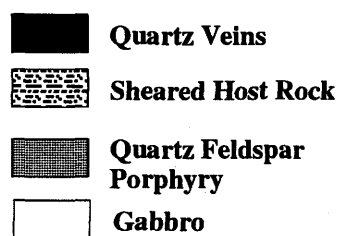
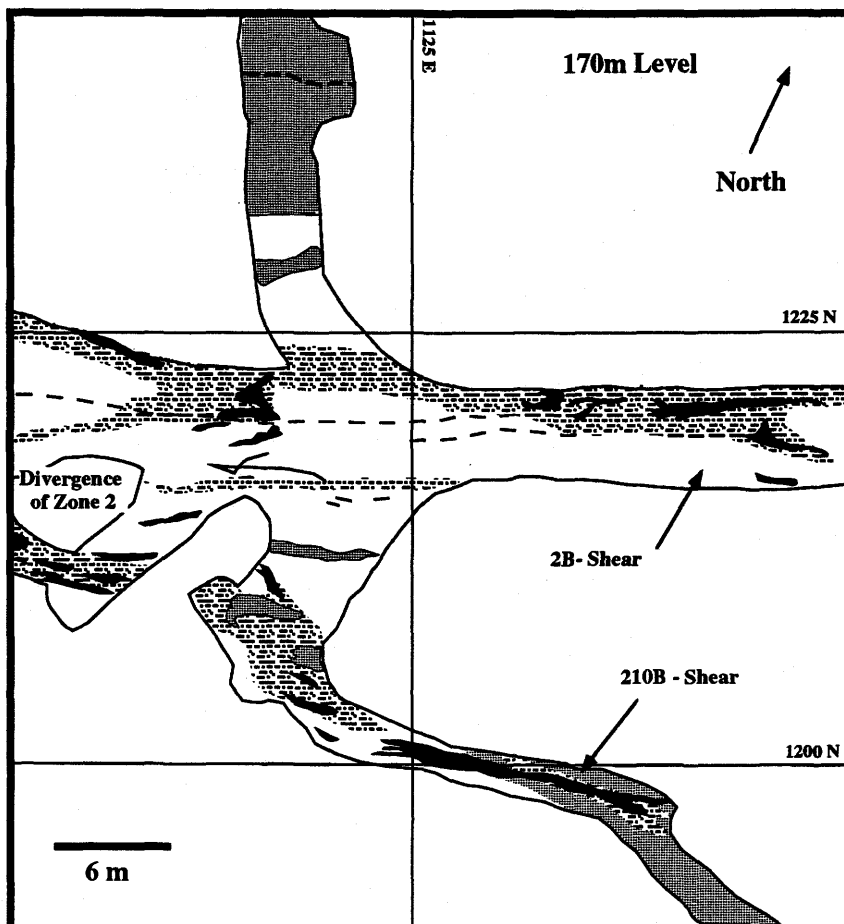


Figure 3.4 - Simplified geology map of the 170m level highlighting the divergence of Zone 2.

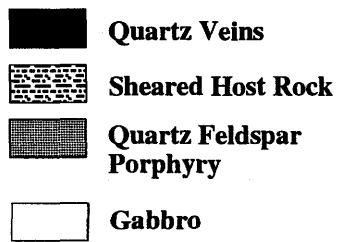
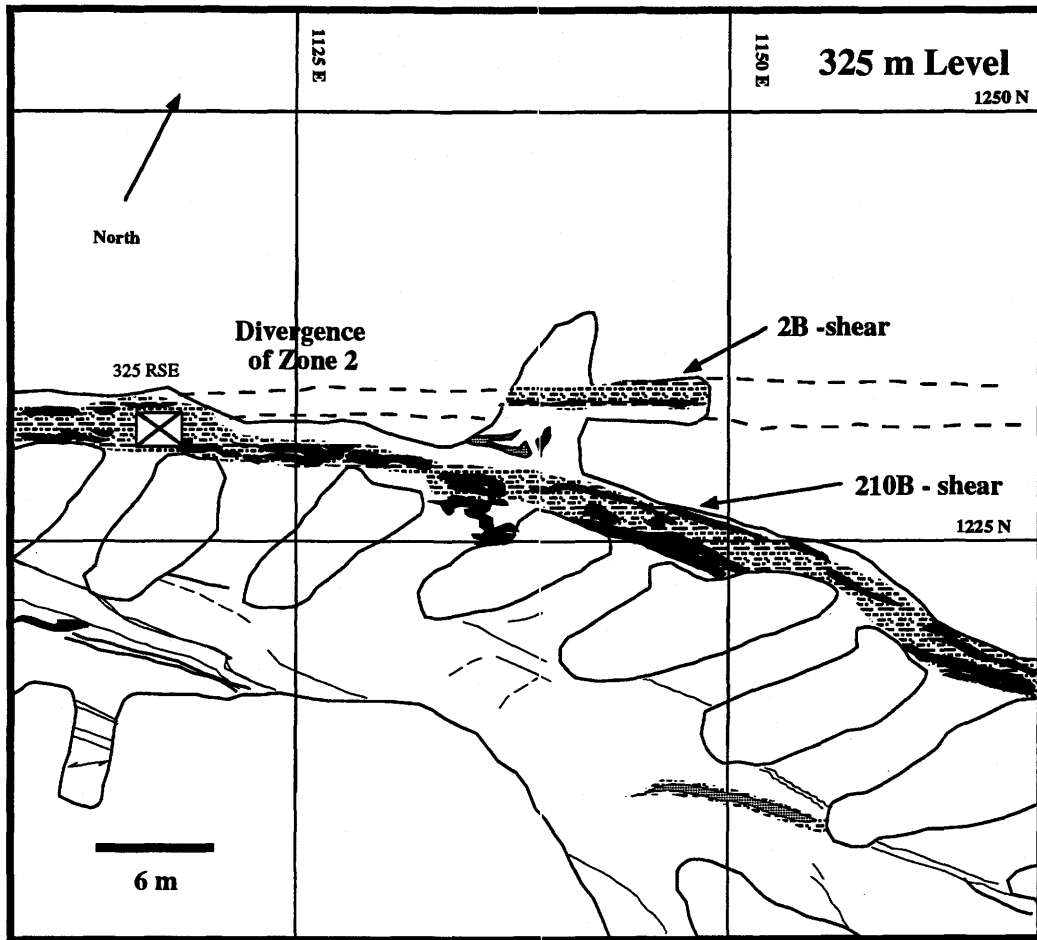


Figure 3.5 - Simplified geology map of the 325m level highlighting the divergence of Zone 2.

the last episode of shearing. Later deformational events, which post dates shearing, overprint the area, and are responsible for folding and deformation of the Seabee and Santoy Lake quartz vein systems (Durocher et al., 1992).

3.3.2 Hydrothermal mineralogy and paragenetic sequence

The Seabee veins are dominated by quartz, although they also contain numerous other hydrothermal mineral phases such as tourmaline, K-feldspar, calcite, pyrite, pyrrhotite, chalcopyrite, tellurides, and gold. Independent petrographic studies have also identified hydrothermal magnetite, sphalerite, molybdenite, and barite (Cambell, 1986; McLeod, 1983).

There are two distinct paragenetic sequences. Stage I mineral assemblage consisting of quartz-tourmaline±(K-feldspar)-pyrite was precipitated during primary vein emplacement. Complete petrographic descriptions of the primary vein mineral assemblage is reported by McLeod (1983) and Cambell (1986). These veins were then fractured and the Stage II minerals, mainly carbonate, were precipitated in the fractures. Other Stage II mineral phases, such as pyrrhotite, chalcopyrite, apatite, tellurides, and gold have precipitated in textural equilibrium with calcite. Paragenetic relationships of the hydrothermal vein minerals are illustrated in Figure 3.6

The occurrence and distribution of Stage II minerals were controlled by the composition of the vein material hosting the microfractures. Within the quartz dominated portion of the Stage I vein assemblage, Stage II minerals are mainly carbonate with only limited chalcopyrite, tellurides and apatite (Plate 3.1). Where microfractures crosscut tourmaline, the tourmaline is variably altered and has a reddish brown mottled appearance.

Paragenesis of the Seabee deposit

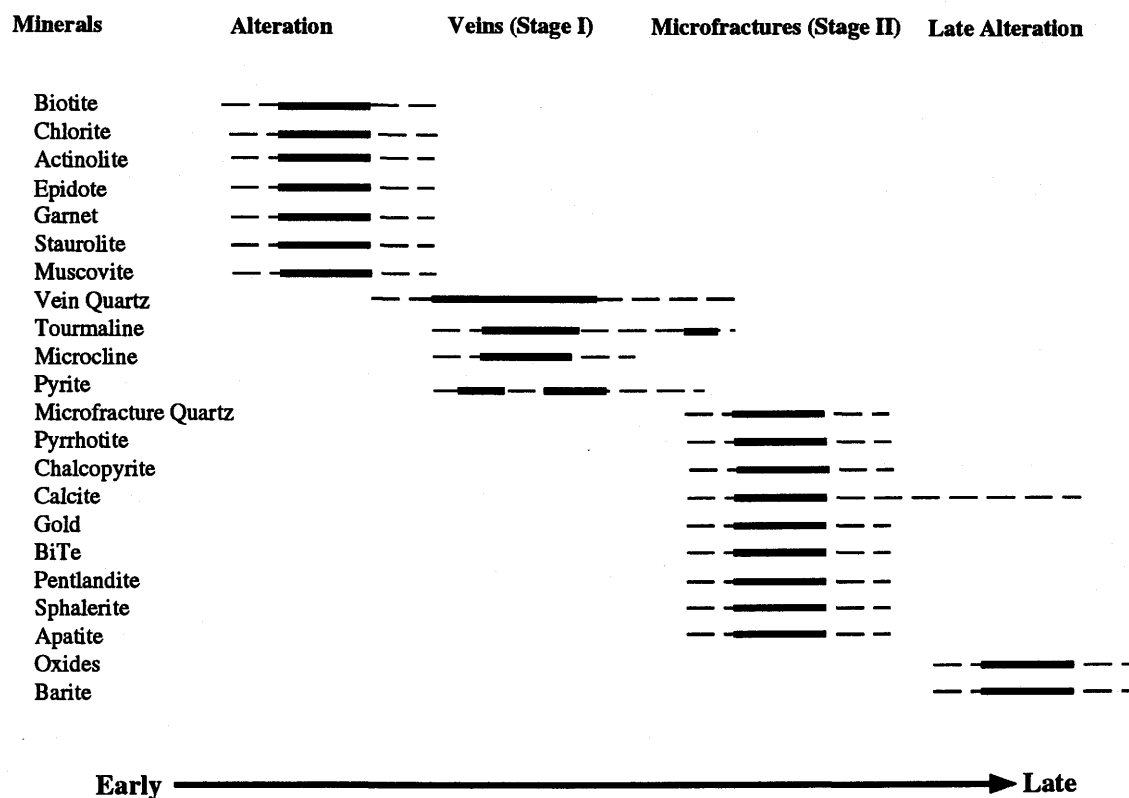
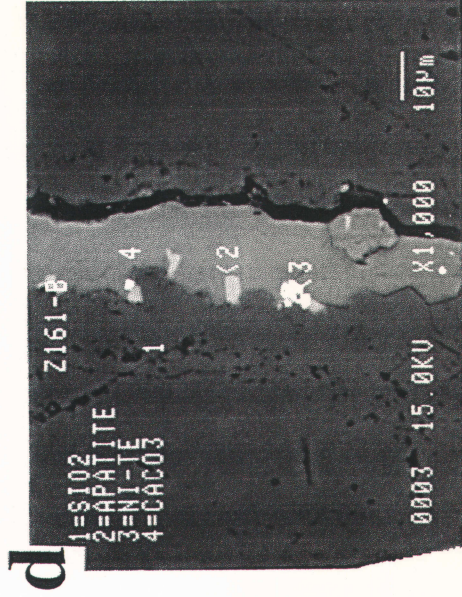
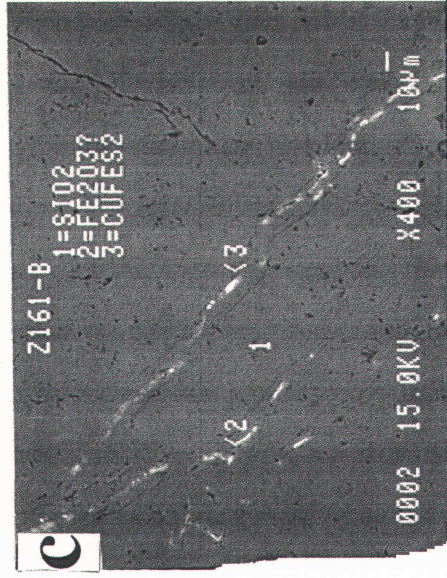
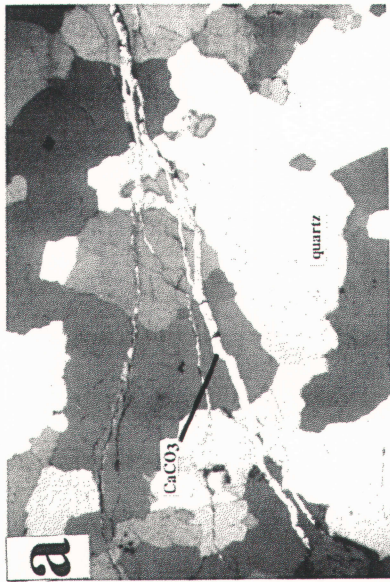


Figure 3.6 - Mineral inventory and relative paragenesis in shear zones hosting the Seabee deposit. Dashed lines represent less certain occurrence.

Plates 3.1 (a) Photomicrograph of calcite veinlets cutting vein quartz, in cross-polarized light. Horizontal field of view approximately 5 mm; (b) Photomicrograph of altered mottled tourmaline in plane-polarized light. Horizontal field of view approximately 5 mm; (c) Backscattered electron image of microfractures within the quartz-dominated portion of the vein. Fe_2O_3 is an alteration product, the result of late meteoric water interacting with the Cu - sulphide phase. (b) High magnification, backscattered electron image of the above microfracture (1000x). Note the restricted mineral assemblage dominated by CaCO_3 .

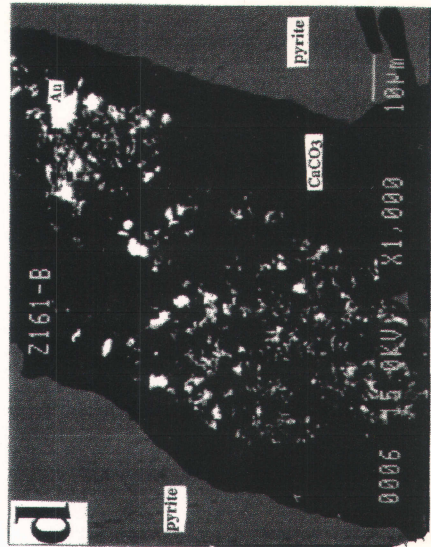
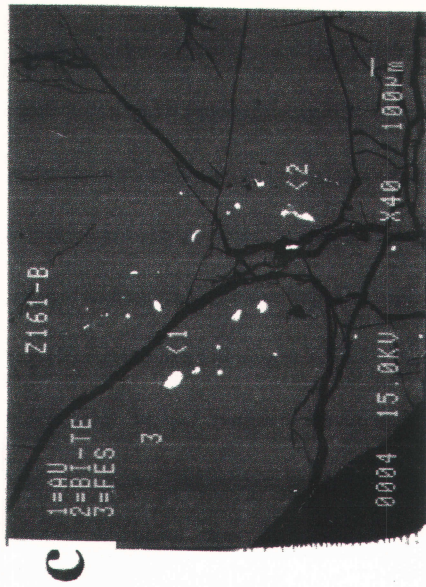
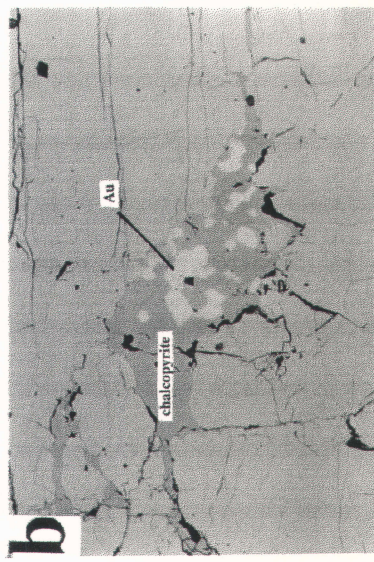
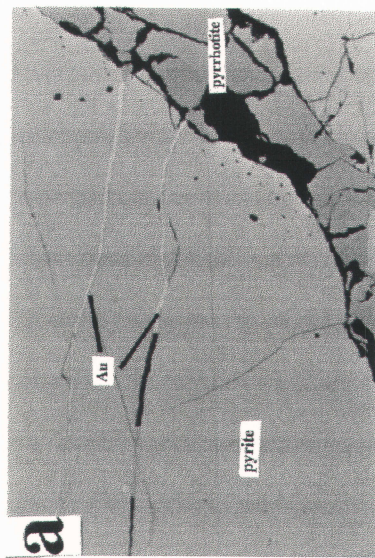


Stage II chalcopyrite, pyrrhotite and gold assemblages occur where the microfractures crosscut pyrite rich portions of the vein. In addition, calcite, minor tellurides, and apatite also occur within the pyrite hosted microfractures (Plate 3.2). Rarely, gold occurs as blebs aligned in linear arrays within pyrite (Plate 3.2). These linear patterns are similar in appearance to planes of secondary fluid inclusions (cf. Roedder, 1979), and are interpreted to represent Stage II gold deposition where Stage I pyrite has become recrystallized around the gold grains. Sulphur isotope data presented in Chapter 6 support the above interpretation of pyrite recrystallization.

3.3.3 Gold Precipitation Mechanism

A proposed precipitation mechanism for mesothermal gold is the immiscibility model, where pressure fluctuation in the vein system cause H₂O-CO₂ phase separation. During CO₂ separation from the hydrothermal fluid, gold bearing bisulphide complexes become unstable, thereby causing gold to be precipitated (cf. Bowers, 1991, and references therein). At Seabee an alternative precipitation mechanism is possible. Petrographic relationships demonstrate that gold occurs late in the vein paragenesis and is localized in fractures within pyrite, whereas no gold occurs within microfractures that traverse quartz. This relationship implies that gold precipitated in response to fluid interaction with a pre-existing pyrite phase. In detail, the mechanism may involve chemisorption, electroplating, or some other chemical reactions between the auriferous fluid and pyrite. This process would be analogous to the wall-rock interaction mechanism documented for the Contact Lake deposit where fluid interaction with mineral phases, such as pyrite, K-feldspar, biotite, and epidote, have resulted in gold precipitation (cf. Fayek *et al.*, 1993).

Plates 3.2 (a) and (b) Photomicrographs of high-grade ore from Zone 2. Note microfractures within pyrite, and the late siting of gold. The Stage II assemblage also includes chalcopyrite, pyrrhotite, and carbonate. Horizontal field of view approximately 5 mm; (c) Backscattered electron image of microfractures within pyrite. Note: gold blebs occur in a planar array parallel to microfractures. Dark background within microfractures is CaCO_3 , (d) Backscattered electron image within one of the above microfractures (1,000x). The bright points are gold rimmed by apatite. The dark background is CaCO_3 , whereas the medium grey material is the host pyrite.



4.0 Protolith discrimination

During the deformation and hydrothermal alteration that accompanied formation of the Seabee Shear Structure, the primary character of the host rocks became obscured. In an attempt to determine primary lithological types, major and trace element analyses were conducted for the least-altered primary lithologies beside the shear zone, and for mylonites within the structure. Once the primary protoliths are determined, it may be possible to interpret geological setting, structural controls, and plausible genetic models.

As described in Chapter 2.1 , a variety of mafic and felsic dykes have intruded the Laonil Lake Intrusive Complex. These are: (1) mafic dykes, (2) granodiorite-quartz diorite units, (3) diorite dykes, and (4) feldspar porphyries. In most instances, the four dyke lithologies occur as parallel intrusive sheets, and strike sub-parallel to the shear structures at approximately 070°. The dykes predate the development of the mylonitic fabric of the Seabee Shear Structure.

Mafic mylonites exhibit intense potassium enrichment marked by alteration of hornblende to biotite (Schultz and Kerrich, 1991). For the feldspar porphyries and granodiorite dykes, however, there is no pronounced potassium enrichment (i.e. limited hydrothermal biotite). Thus, the hydrothermal fluids responsible for both quartz veining and potassic alteration

appear to be in chemical (aK^+/H^+) equilibrium with felsic rocks, but not with mafic rocks. Furthermore, petrographic discrimination of deformed felsic lithologies (feldspar porphyries and granodiorite dykes) are possible due to their light colour index and high modal abundance of quartz.

Major elements were analyzed by X-Ray Fluorescence Spectrometry (XRF). Aliquots of the sample powders were analyzed by ICP-AES for Cr, Ni, Pb, Ag, and Cu, and by ICP-MS for Rb, Sr, Y, Zr, Hf, Nb and the full REE series, La to Lu (See Appendix C for complete analytical procedures).

4.1.0 Protolith discrimination

To identify if there is a single, or multiple, protolith(s) present within the structure(s), a diamond drill hole interval (S-128) that intersects Zone 2 was sampled and analyzed for specific major and trace elements listed above. Visually the rocks within the drill core traverse exhibits a marked reduction in grain size as compared to host rock lithologies external to the shear zone; drill core on the south end of the traverse appears to be dominantly felsic, whereas mafic lithologies dominate at the north end of the interval. Numerous late carbonate veins cut the core, and avoided during sample selection.

From inspection of the results (Appendix E), it is apparent that Cr values vary systematically from footwall to hanging wall. Cr concentrations are low from 45.5 to 53.5 metres, ranging from 20 to 100 ppm, but increase to 1000 ppm at 55.0 metres. Cr and Ni concentrations are coupled, with high Cr and Ni values corresponding to more mafic samples.

4.1.1 Cr vs. Zr and Hf

In accordance with standard protolith discrimination, selected major and trace elements generally considered to be

insensitive to alteration (Zr, Al_2O_3 , TiO_2 , Hf, etc.) were initially utilized for discrimination. Cr and Ni proved to be the best elemental discriminators, as there is significant variations in elemental concentration between Ni and Cr for the various host rocks and shear zone mylonites. Accordingly they are utilized in many of the discriminant plots.

Zr and Hf, which are generally considered to be immobile during many hydrothermal processes, increase in concentration in shear zone samples (Figures 4.1 - 4.2), compared to the various host rocks. Thus, the Seabee Shear Structure may have experienced a period of Zr metasomatism. Alternatively, these same results can be obtained if the rocks experienced a change in bulk volume or Cr loss. As a result, these two elements cannot be used for protolith discrimination, as Zr and Hf mobility, or volume change occurred during deformation.

4.1.2 Cr vs. Al_2O_3 - TiO_2

Plots of Cr vs. Al_2O_3 effectively separate intermediate (diorite) units from the more mafic protoliths (gabbros and mafic dyke), although the Al_2O_3 concentration does not vary sufficiently as to distinguish between the individual mafic rock types (Figure 4.4). TiO_2 shows a greater variance as a function of lithology, and if Cr is plotted vs. TiO_2 (Figure 4.3) four populations become apparent, and the mafic lithologies are readily discriminated, i.e. two different mafic dyke lithologies, and a gabbro and diorite unit.

Two populations of mafic dyke lithologies, mafic dyke A (a Cr-Ni poor unit) and mafic dyke B (Cr-Ni rich unit), are also present. This separation into two mafic dyke protoliths is common throughout most of the discrimination diagrams, although if a heavy rare earth element (HREE), such as Lu, is used as a discrimination element (Figure 4.6 and 4.7) the separation of the two mafic dyke lithologies is less evident.

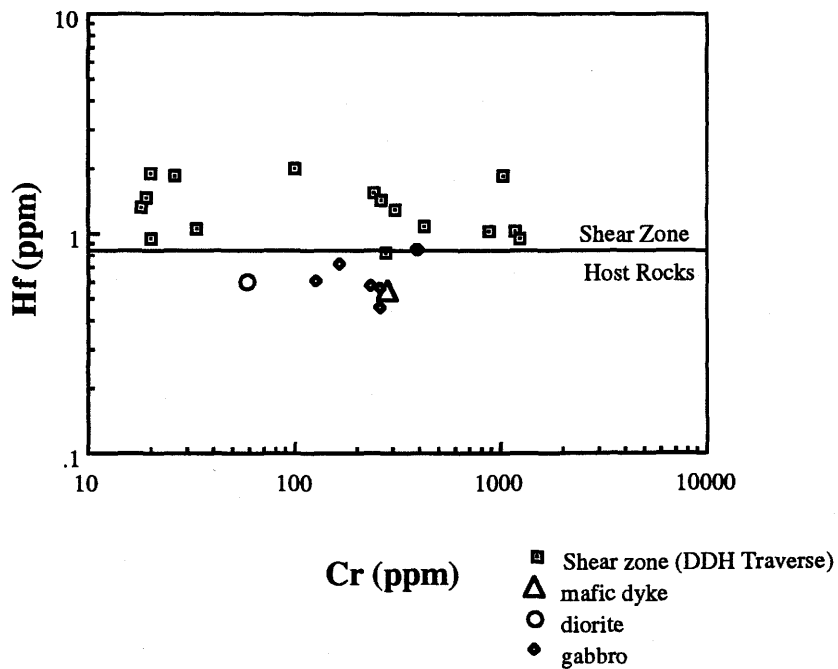
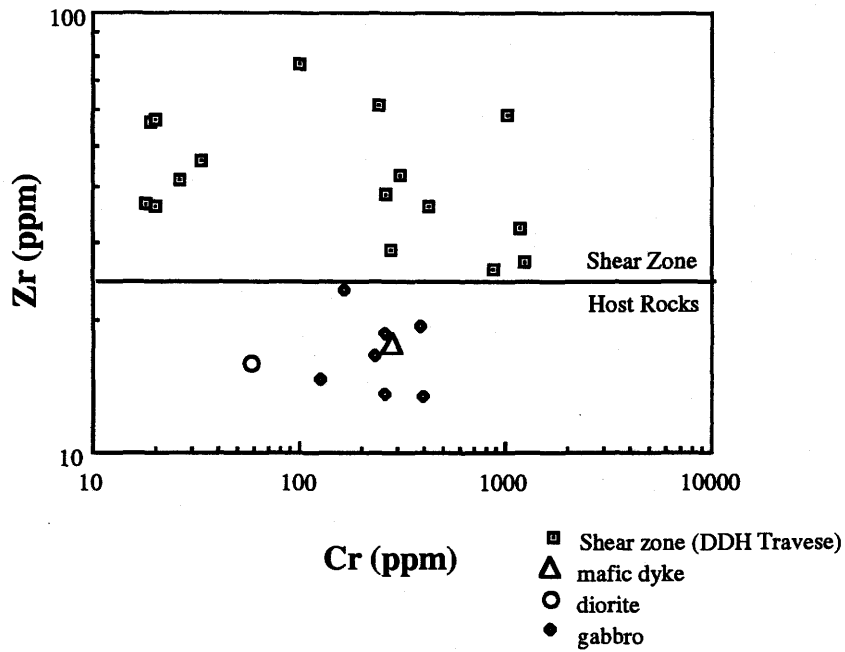


Figure 4.1 and 4.2: Cr plotted against Zr and Hf demonstrating volume change or preferential Zr and Hf enrichment in shear zone mylonites.

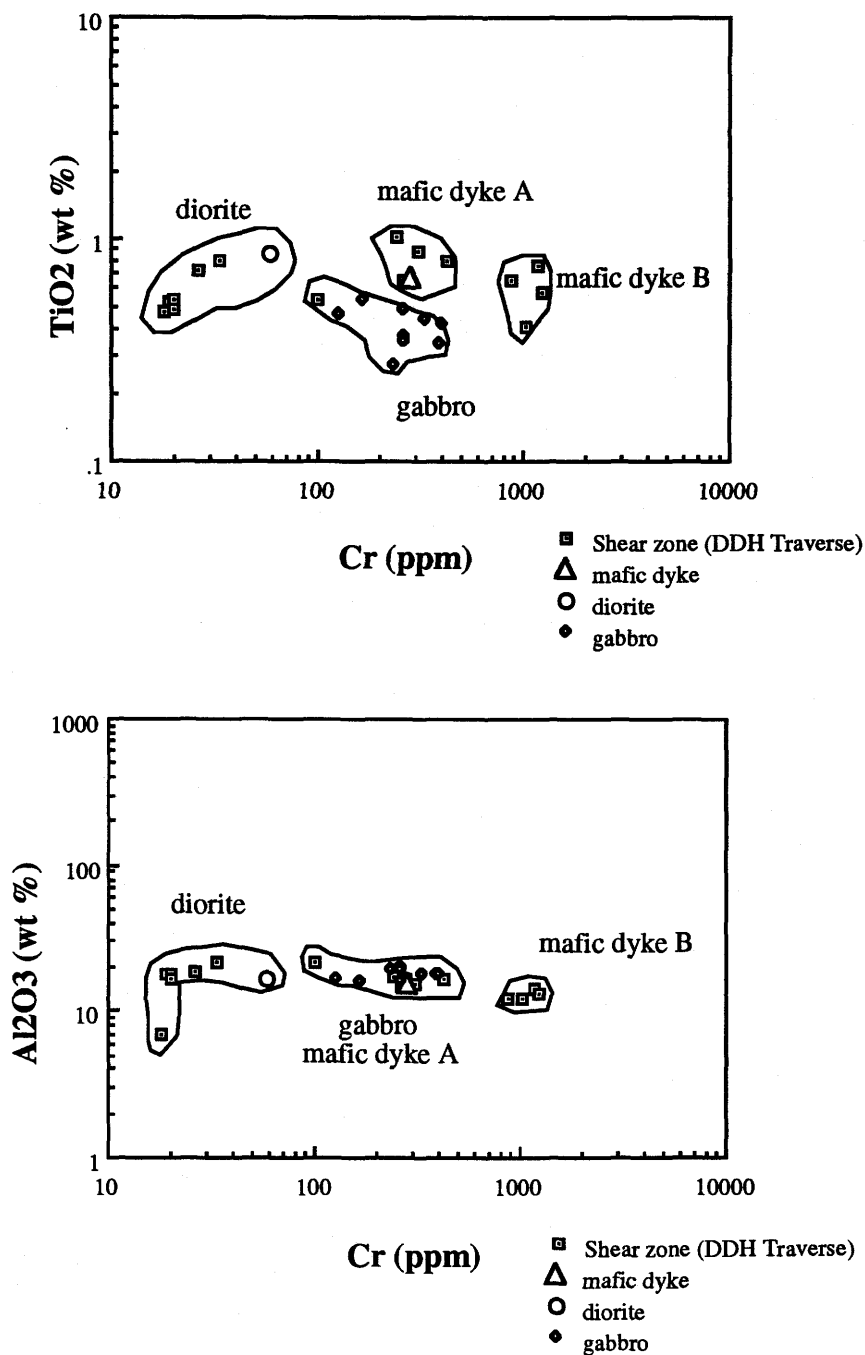


Figure 4.3 and 4.4 - Figure 4.3 illustrates protolith discrimination based on systematic variation in TiO₂ and Cr, with 4 protoliths being distinguished: (1) diorite, (2) gabbro, (3) mafic dyke A and mafic dyke B. Conversely, Al₂O₃ concentrations does not vary significantly with change in (Figure 4.4) protolith. Thus, Cr vs Al₂O₃ can only discriminate 3 lithologies: gabbro + mafic dyke A, mafic dyke B, and diorite (gabbro and mafic dyke A appear to be identical).

4.1.3 Cr vs. Ni-Lu

As with Al_2O_3 vs. Cr (Figure 4.4), the Cr vs. Ni discrimination diagram (Figure 4.5) only distinguishes three protoliths; with gabbro and mafic dyke lithologies seemingly identical. This is probably due to the similarity of Ni and Cr concentrations of the gabbros and mafic dyke A lithologies. This same relationship is also demonstrated in Figure 4.4. If an alternative discriminant element is utilized, such as an immobile HREE (Lu) (Figure 4.6) which exhibits significant variation between gabbros and mafic dykes, it is possible to distinguish the same four protoliths that are apparent on the plot of Cr vs. TiO_2 in Figure 4.3.

4.1.4 Ni vs. Lu

A comparison of Figure 4.6 and 4.7 shows that Ni and Cr vs. Lu have similar distribution pattern for various protoliths. This suggests that Ni and Cr contents are correlated, and may be substituted for one another in protolith discrimination.

4.1.5 REE, $(\text{La}/\text{Yb})_n$ and Lu

Rare Earth Element (REE) patterns for individual host rocks are depicted in Figure 4.8. The diorite and gabbros show moderate Light Rare Earth Element (LREE) enrichment, whereas the mafic dykes are less LREE enriched. With subtle but distinctive variation in REE concentrations, the individual REE patterns may be utilized as discriminants of lithologies, although a numerical representation is needed to make it possible to plot REE patterns vs. other major or trace elements.

Numerical representation is accomplished by normalizing a LREE (La) and HREE (Yb) to chondritic values. These two normalized values are in turn divided by each other [$(\text{La}/\text{Yb})_n$], thereby

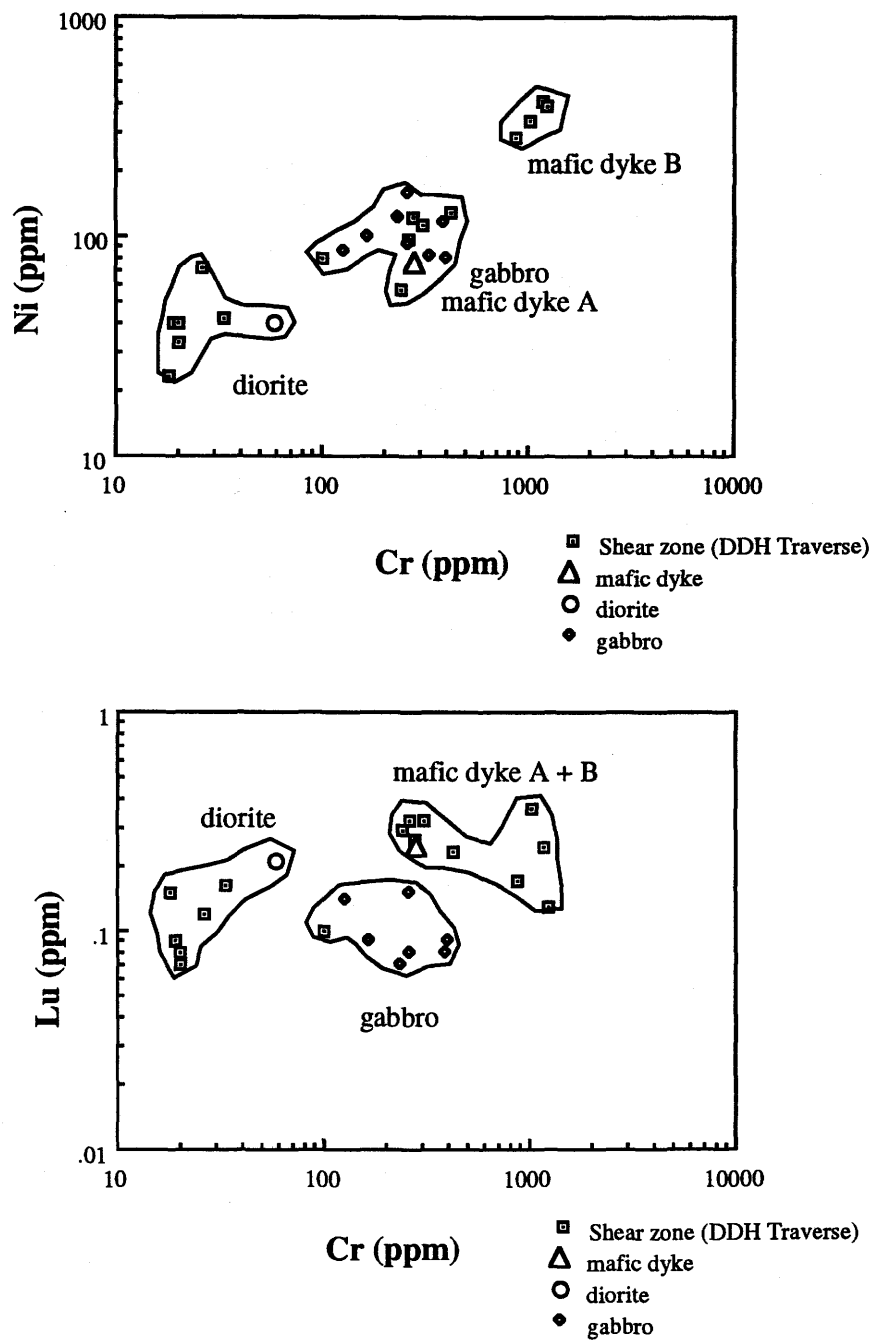


Figure 4.5 and 4.6 - Cr plotted vs. Ni and Lu. Similar to Al_2O_3 in Fig 4.4, Cr vs Ni does not vary sufficiently as to allow for discrimination of more than three protoliths. Conversely, if Cr is plotted vs. any incompatible HREE (Lu), the gabbro and the shear zone equivalents are easily distinguished from the mafic dyke A.

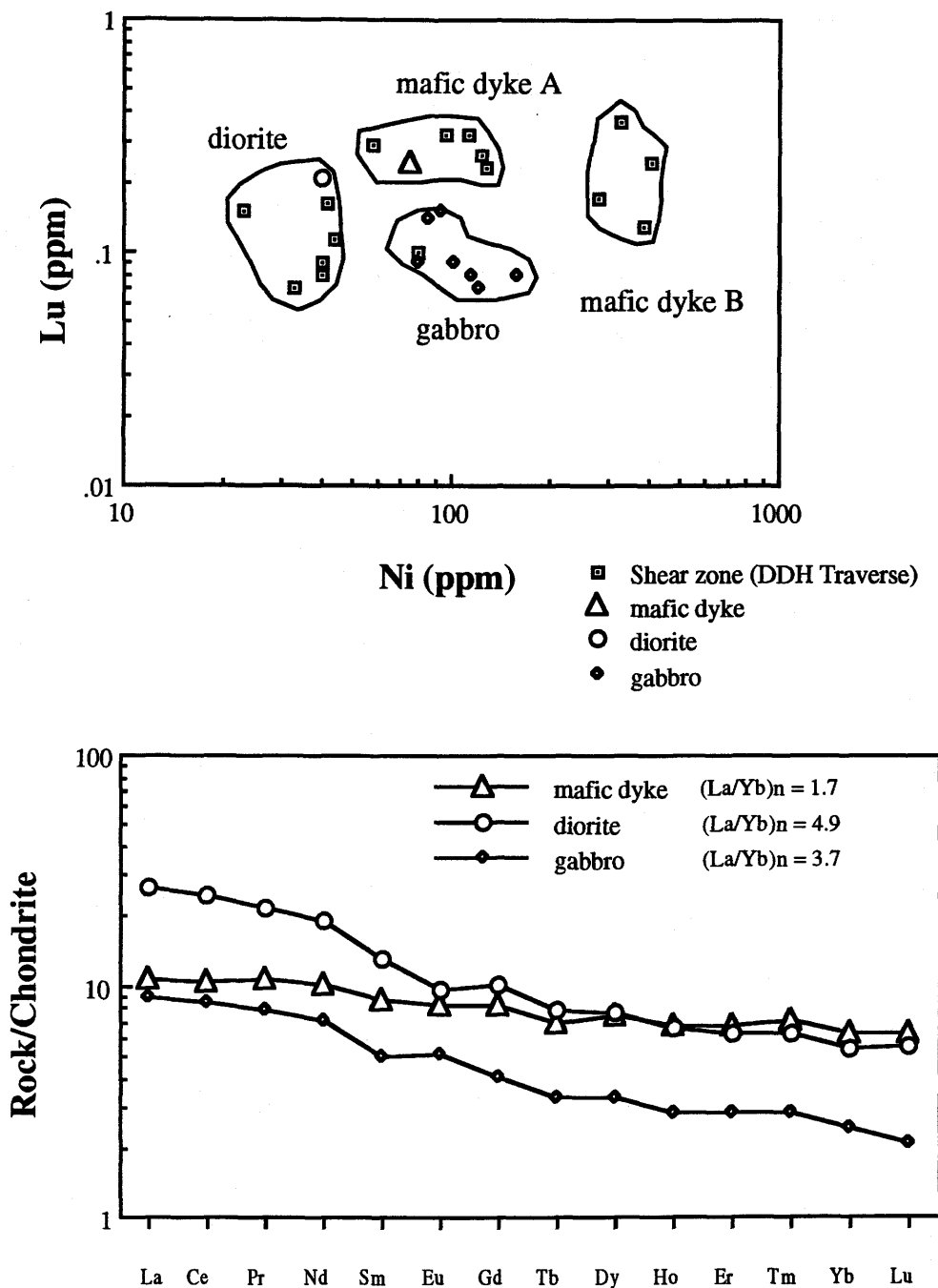


Figure 4.7 and 4.8- Fig. 4.7 illustrates how Ni may be used as a discriminating element. Fig. 4.8 shows the various REE patterns for different host rocks and their associated "slopes" or $(La/Yb)_n$ values.

representing the slope of the REE pattern for an individual sample. For example, the greater the LREE enrichment the steeper the slope of the REE line, and hence a higher $(La/Yb)_n$ ratio (diorite in Figure 4.8 has $(La/Yb)_n = 4.9$). Conversely, a sample, such as the mafic dyke (Figure 4.8), which is less LREE enriched will have a flatter REE line and a low $(La/Yb)_n$ value (1.7).

The slope of REE patterns [$(La/Yb)_n$] plotted vs. an immobile transition metal (Cr) (Figure 4.9) or an immobile REE (Lu) (Figure 4.9) readily separates the various mylonites and schists in the Seabee Shear Structure into four distinctive protoliths, similar to discrimination diagrams Figures 4.3, 4.6 and 4.7.

There are two outliers in Figure 4.9 and one in Figure 4.10 that do not cluster within any given field. This may be accounted for by sample inhomogeneity, or some variations in the analytical results. Notwithstanding minor variations in REE distributions, slopes of REE patterns can be utilized as a method of protolith discrimination for the Seabee Shear Structure.

4.2 Discussion

One of the most controversial geological aspects of the genesis of the Seabee deposit is the presence, or possible presence, of "sedimentary" or extrusive rock units. These lithological types were described as layered, sheeted volcanic or volcanogenic sediments (Gummer, 1986). One interpretation of these field observations has led to a syngenetic model for gold mineralization for the Seabee Mine; namely the concept that the "layered" sedimentary lithologies represent a synvolcanic sedimentary exhalative gold unit (Gummer, personal communication), with the Laonil Lake Intrusive Complex representing a volcanic-subvolcanic sill complex (Gummer,

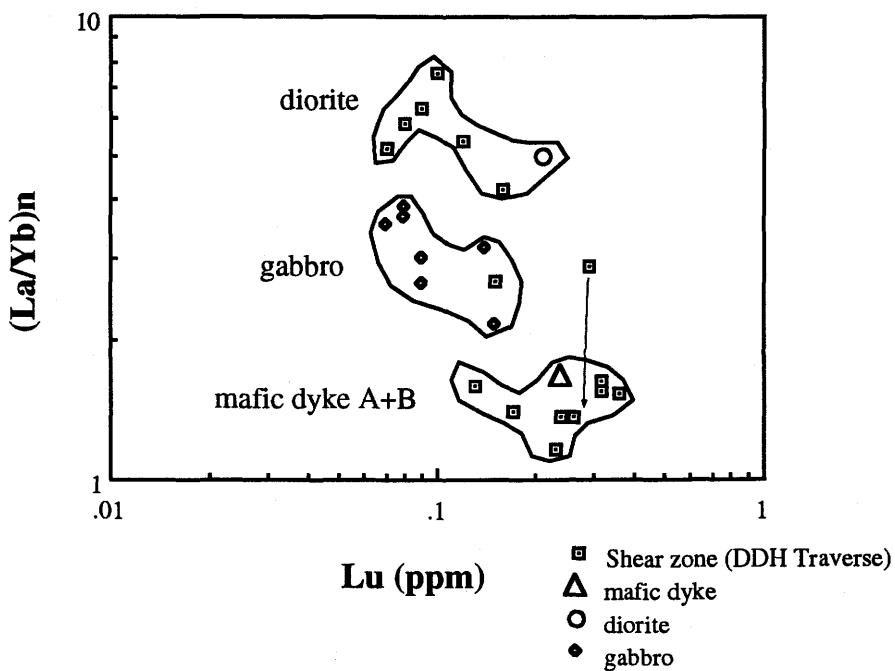
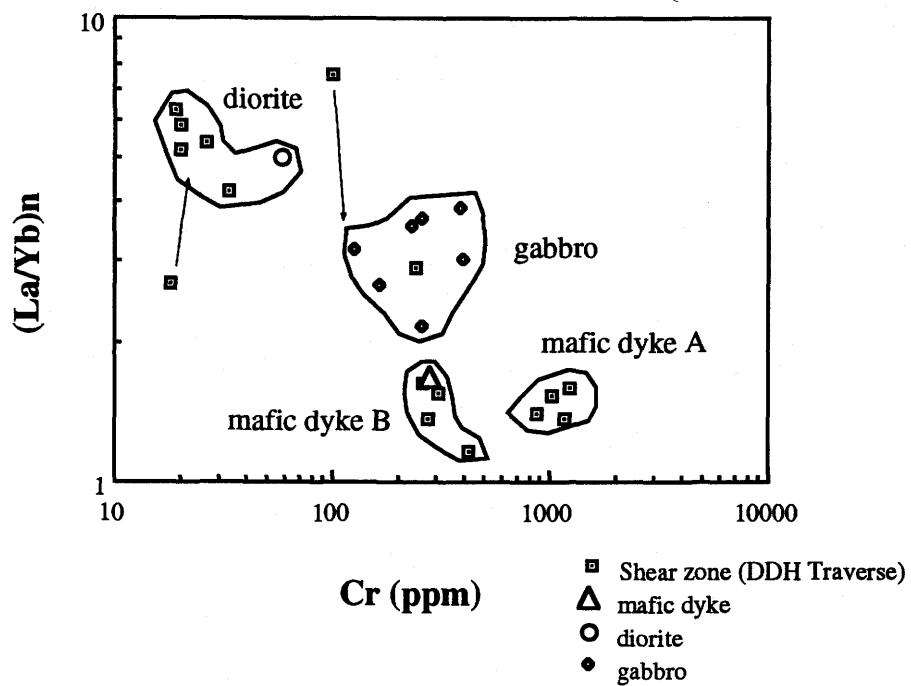


Figure 4.9 and 4.10 - Variation diagrams utilizing the "slope" of the REE pattern [(La/Yb)_n] with an immobile HREE (Lu) and a transition metal (Cr). These two diagrams have a similar protolith distribution as Figures 4.3, 4.6 and 4.7. Arrows indicate shift in Rare Earth Element distribution.

1986). Gummer concluded that the "layering", which exhibits changes in both composition and grain size, represents a primary "S₀ bedding" plane.

This protolith investigation has shown that the diamond drill hole traverse, which sampled through the shear zone at Zone 2, contains several protoliths (i.e. gabbros, mafic dykes A and B, and diorite), as illustrated by the various variation diagrams (Figures 4.3, 4.6, 4.7, 4.9 and 4.10). The drill core exhibits a markedly smaller grain size than the primary host lithologies adjacent to the shear structure. Furthermore, potassic overprinting marked by replacement of hornblende by biotite gives the sheared mafic lithologies the appearance of a fine-grained potassic sediments, similar to "sedimentary" units observed by Gummer (1986).

As a result of the above observations, the diamond drill hole interval, and other "sedimentary" units within the Seabee claims, are reinterpreted to represent a collage of protoliths (mafic + felsic), which experienced hydrothermal overprinting, and intensive deformation associated with shearing. Therefore, the genetic model suggesting that the Seabee deposit was a Sedex style of mineralization can now be ruled out. The combination of grain size reduction (via combined pure and simple shearing) and potassic metasomatism endorses the shear hosted mesothermal genetic model proposed by Schultz and Kerrich (1991). The above conclusion only refers to the Seabee deposit, and in no way does it apply to other deposit or showings within the Glennie domain (i.e. Santoy Lake system or Pine Lake showing).

5.0 Fluid inclusion characteristics

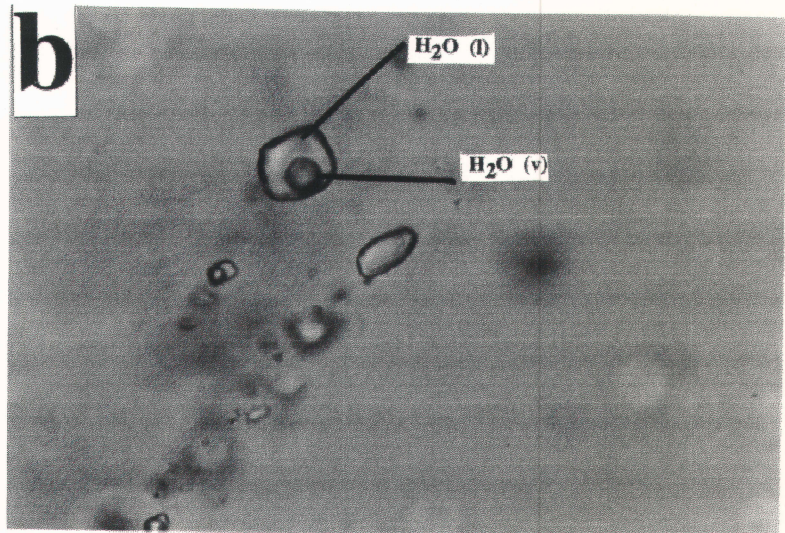
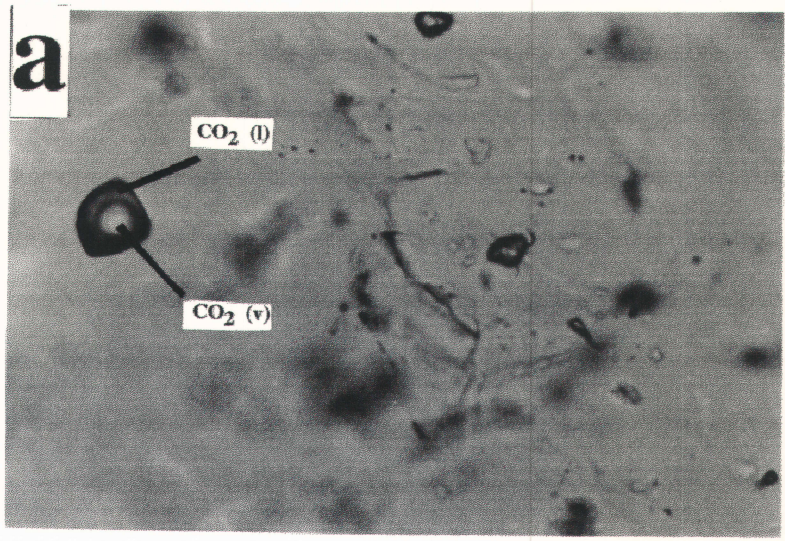
5.1 Petrography and inclusion type

Fluid inclusions have been examined within quartz and tourmaline in veins of the Seabee Shear Structure. The majority of observed inclusions are in vein quartz, although hydrothermal tourmaline also contains fluid inclusions, but these are too small ($< 3\mu\text{m}$ in diameter) to observe phase relationships. No fluid inclusions were observed in calcite or the minerals associated with gold. Planes of "secondary" and "pseudosecondary" inclusions in quartz are cut by the microfractures that host gold.

As described previously, the veins were emplaced prior to the last major episode of deformation, and were subsequently folded (Delaney, 1992). This deformation is preserved in quartz in the form of undulose extinction and limited sub-grain development. No extensive dynamic recrystallization, or full-scale dynamic recovery is evident, although trails of secondary and pseudosecondary fluid inclusions become obliterated at or near late microfracture boundaries.

Fluid inclusions can be classified as Type I (Plate 5.1) and Type II inclusions. Type I are represented by planes of secondary inclusions which may or may not cross grain boundaries. These are interpreted to be either "secondary" (S) or "pseudo-secondary" (PS) inclusions, according to the

Plates 5.1 Photomicrographs(sample S133 281.0; Stage I Quartz): Type I fluid inclusions in a linear array typical of secondary fluid inclusions observed at the Seabee deposit (cf. Roedder, 1979). (a) Type Ia $\text{CO}_2(\text{v})\text{-CO}_2(\text{l})$ inclusions ($\leq 7 \mu\text{m}$). (b) Type Ib $\text{H}_2\text{O}(\text{v})\text{-H}_2\text{O}(\text{l})$ fluid inclusions (diameters $\leq 10 \mu\text{m}$).



classification scheme of Roedder (1979). The frequency of occurrence of Type I inclusions increases at or near grain boundaries, particularly where multiple grain boundaries meet. Primary fluid inclusions were not observed in this study.

The lack of primary inclusions suggests that they were obliterated during deformation and/or hydrothermal activity that post dated the precipitation of main stage quartz, consistent with the folded and deformed nature of the veins. The "secondary" (S) or "pseudosecondary" (PS) inclusions likely record either the waning stages of the event that precipitated the quartz, or a later fluid event. Thus, fluid inclusion thermometric data would represent ambient fluid (P-T-X) conditions present during or after main stage quartz vein emplacement.

Type I (Plate 5.1) inclusions are typically 3-10 μm in diameter and consist of 3 varieties: Type Ia $\text{CO}_2(\text{v})-\text{CO}_2(\text{l})$ [Two phase CO_2], Type Ib $\text{H}_2\text{O}(\text{v})-\text{H}_2\text{O}(\text{l})$ [Two phase H_2O], and Type Ic $\text{CO}_2(\text{v})-\text{CO}_2(\text{l})-\text{H}_2\text{O}(\text{l})$ [Three phase]. Type Ic is typically CO_2 rich and was only observed in a surface sample (Sample Z2-7).

Type Ia inclusions are CO_2 rich, are rarely necked, and have a characteristically negative crystal habit. Type Ib inclusions, which often occur in the same plane as Type Ia inclusions, are characterized by high degrees of filling, and are variably "necked" (cf. Roedder, 1979). Necked inclusions are generally irregular having odd shaped protrusions such as long narrow appendages and bulbous nipples (Figure 5.1). Necking of fluid inclusions has a pronounced influence on thermometric data, resulting in variable homogenization temperatures. Necking usually has little effect on freezing thermometric data. Type Ic inclusions are rare and were only observed in sample Z2-7. These inclusions are typically CO_2 rich, having a CO_2 volume percent of 70 to 80% with a






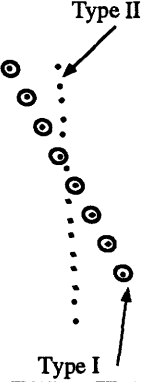
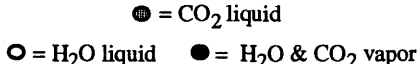
Seabee Deposit: Fluid inclusions characteristics from quartz veins in Zones 2 and 5			
Type	Pict	Thermometric Data	Location
Ia CO ₂ (l)-CO ₂ (v) PS & S		ThCO ₂ = 24 to 33.6 °C TmCO ₂ = -59.2 to 54.0 °C 100 volume % CO ₂ CO ₂ bulk density = 0.66 to 0.79 g/cm ³	Zone 2 (DDH S-133 281.0 m) Zone 5 (Z5-4)
Ib H ₂ O(l)-H ₂ O(v) PS & S	 	ThH ₂ O = 110 to 354 °C TmH ₂ O = -1.3 to -4.8 °C wt % NaCl eq. average 3% (1.5 to 7.5%)	Zone 2 (Z2-7)
Ic CO ₂ -H ₂ O PS & S	 	70 to 80 volume % CO ₂ TmCO ₂ = -55.2 to 54.2 °C wt% NaCl eq. average 3% (2.8 to 3.3 %) CO ₂ bulk density = 0.66 to 0.68 g/cm ³	Zone 2 (Z2-7)
II H ₂ O S		Type II inclusions are small (< 3.0 μm), thus reliable thermometric data could not be obtained.	Zone 2 (DDH S-133 281.0 m) Zone 5 (Z5-4) Zone 2 (Z2-7)
PS=Pseudosecondary S = Secondary	 ● = CO ₂ liquid ○ = H ₂ O liquid ● = H ₂ O & CO ₂ vapor		

Figure 5.1 - Summary of fluid inclusion data from the Seabee gold deposit (Zones 2 and 5). All data are summarized in text, and shown here for reference only. Representations of fluid inclusions are schematic, and not to scale.

correspondingly limited amounts of H₂O.

Type II inclusions are small (< 3 μ m) and occur in planes which crosscut Type I inclusions. No phases relationships or thermometric data could be obtained due to their small size.

5.2 Thermometric data

Phase changes that occur during the heating of inclusions that are first frozen to -196 °C provide information on fluid composition (low temperature data). These phase changes are as follows:

T _{mCO₂}	melting point of CO ₂
T _e	eutectic, or first melting temperature of ice
T _{m_{ice}}	last melting temperature of ice
T _{clath}	melting point of clathrate (CO ₂ · 5.75 H ₂ O)

Low temperature data from the Seabee deposit are presented in Appendix G. The results from Appendix G and data from KRTA Inc. (1986) from Appendix B are shown in Figures 5.2 and 5.3. The thermometric data was evaluated utilizing the computer program Flincor ver. 1.2.3 of Brown and Lamb (1989), and equations derived by Brown and Lamb (1986) .

Types Ia and Ic inclusions contain dominantly pure CO₂ which is reflected by CO₂ melting temperatures close to -56.6°C. Some lower T_{mCO₂} measurements of -57.0 to -58.8 °C were obtained, suggesting that minor amounts of other gases, such as N₂, H₂S, SO₂, or CH₄ are present (e.g. Shepherd, 1985). The presence of such impurities in inclusions with T_{mCO₂} < -56.6 °C has been documented from inclusions studies of other vein deposits utilizing laser Raman, or gas chromatography. (cf. Roedder, 1984).

Although Types Ia and Ic inclusions both record median T_{mCO₂} of

Type Ia and Ic inclusions: $\text{CO}_2(\text{v})\text{-CO}_2(\text{l})$ and $\text{CO}_2(\text{v})\text{-CO}_2(\text{l})\text{-H}_2\text{O}(\text{l})$

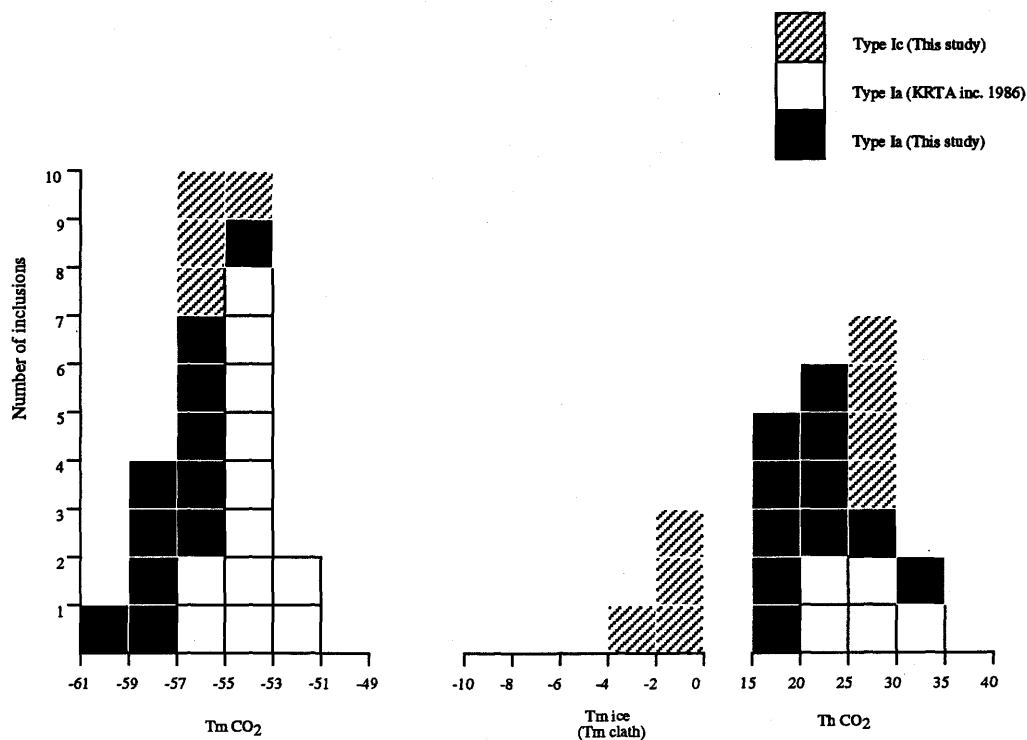


Figure 5.2- Histogram of Type Ia and Ic low temperature microthermometric data from the Seabee deposit. $T_m(\text{CO}_2)$ -melting of CO_2 ice, $T_m(\text{ice})$ - last melting of H_2O ice, $T_h(\text{CO}_2)$ - homogenization temperature of CO_2 liquid and vapor to liquid.

Type Ib inclusions : H₂O(v)-H₂O(l)

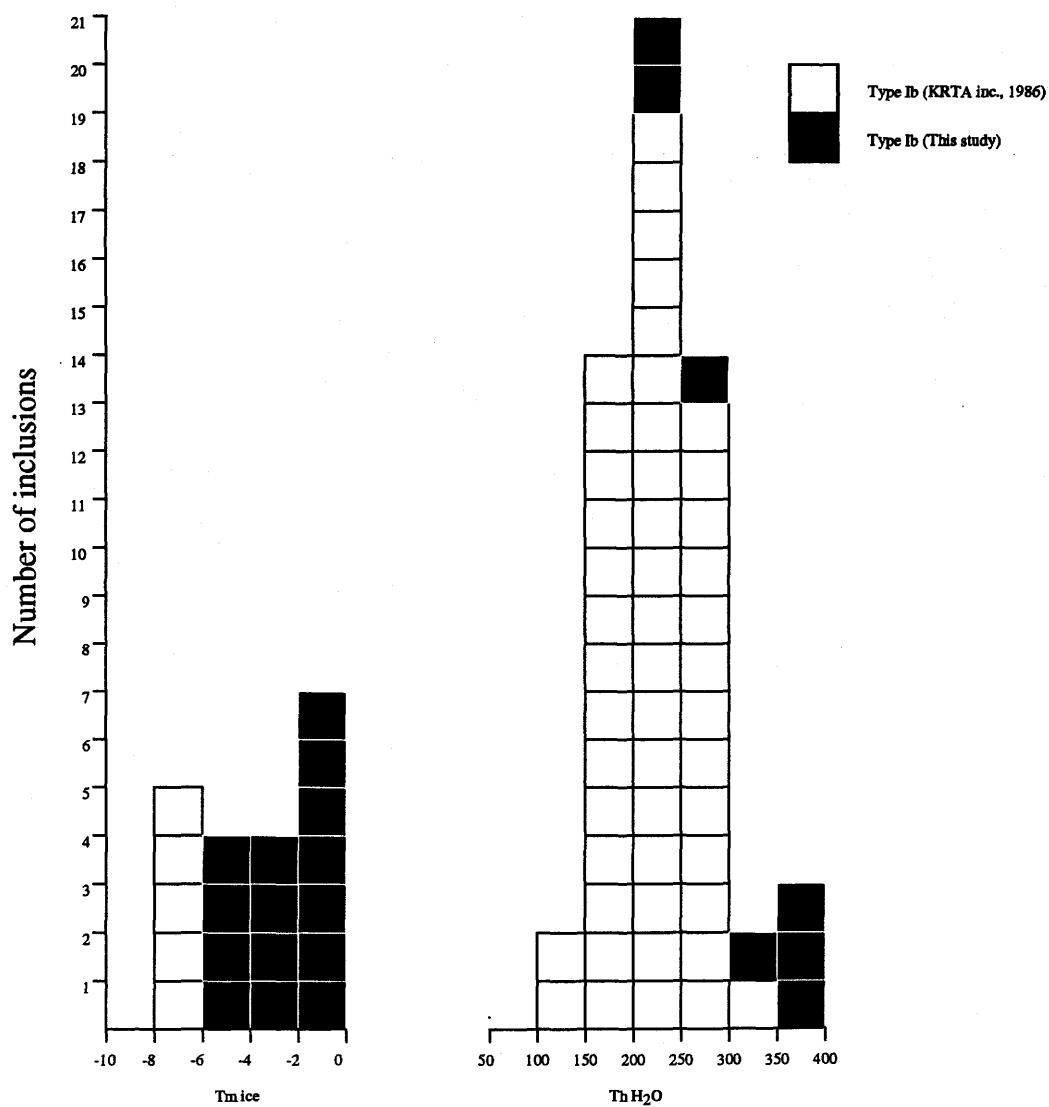


Figure 5.3 - Histogram of homogenization temperatures and low temperature microthermometric properties of Type Ib inclusions from the Seabee gold deposit. Tm (ice) - last melting of H₂O ice, Th (H₂O) - homogenization temperatures of liquid and vapor H₂O.

-56.6 °C, there is significant scatter in the data; many inclusions record $T_{m_{CO_2}}$ as high as -54.0 °C (KRTA Inc., 1986; see Appendix B). Given the small inclusion size (3-10 μm), metastable effects may occur and this is interpreted to be the cause of CO_2 melting above -56.6 °C (cf. Roedder, 1984).

First melting, or the eutectic melting phase change was difficult to observe due to the small size of the inclusions. In two instances (S-133 281.0), a grainy tinge to the ice phase was observed at -10.0 and -6.9 °C respectively. This phase change was taken to represent the T_e temperature. Alternatively, this temperature may represent a period at which the phase changes were most visible rather than the true T_e . According to Crawford (1981), in the system of H_2O -NaCl-KCl, the eutectic point is -22.9 °C. Thus, if the phase changes described above are taken to represent T_e , then the observed temperature does not conform either to this three component system, or the H_2O -NaCl system which has $T_e = -21$ °C. For a system consisting of H_2O -KCl, the eutectic temperature is -10.6 °C (Crawford, 1981). This temperature is closer to the T_e temperature recorded for the Seabee deposit and may indicate that the two inclusions from S-133 281.0 may contain significant concentrations of KCl.

The aqueous phases in Type Ib inclusions have relatively low salinities as given by $T_{m_{ice}}$ of -4.8 to -0.9 °C, corresponding to salinities of 1.5 to 7.5 wt% NaCl equivalent. KRTA Inc. (1986) documented inclusions with $T_{m_{ice}}$ as low as -7.7 °C, equivalent to 11 wt% NaCl (Appendix B).

Salinities for Type Ic inclusions were difficult to assess, as the inclusions were too small to allow for accurate identification of clathrate formation. The phase change that occurred between -1.5 to -2.0 °C was taken to represent the last melting of ice ($T_{m_{ice}}$). This places only a upper

constraint on the salinity of the inclusions. Calculated salinities (Appendix G) would represent only a maxima because during clathrate formation NaCl remains in the aqueous solution, thereby enriching the residual fluid in NaCl, and causes the solution to appear more saline (Collins, 1979). The $T_{m_{ice}}$ temperatures of -1.5 to -2.0 °C would correspond to maximum salinities of 2.5 - 3.3 wt% equivalent NaCl, a salinity similar to Type Ib inclusions. Alternatively, if -1.5 to -2.0 °C phase change is taken to represent the last disappearance of clathrate ($T_{m_{clath}}$), the calculated salinities become considerably higher, i.e. in the 16.5 to 20.0 wt% range. In this case, the data would indicate that the Seabee vein system had interacted with a brine during the geologic evolution of the area.

The density of CO_2 , and the minimum temperatures at which inclusions were trapped, can be determined by measuring the temperature of the following phase changes:

Th	homogenization of liquid plus vapour to liquid only
Th CO_2	homogenization of CO_2 liquid and vapour phases to CO_2 liquid

In Types Ia and Ic inclusions, Th CO_2 ranged from 18.0 to 33.6 °C, and the CO_2 phase always homogenized to a liquid. Calculated CO_2 densities are restricted to a narrow range from 0.663 to 0.795. Data reported by KRTA Inc. (1986) shows the same distribution of CO_2 homogenisation temperatures between 20 and 30 °C (Appendix B).

Only a few homogenization temperatures were obtained for Type Ib inclusions, as there was considerable scatter in the Th of inclusions analyzed. In sample S-133 281.0, the temperatures ranged from 209 to 366 °C. A similar wide distribution of homogenization temperatures was also documented by KRTA

Inc. (1986) ranging from 110 to 340 °C, with an median Th of 212 °C (Appendix B). Given the large amount of data obtained by KRTA Inc. (1986) only a limited number of homogenization measurements were obtained in this study.

5.3 Interpretation of data

As described in the inclusion petrography section, no primary inclusions were observed, and consequently no information can be obtained as to the conditions of primary quartz precipitation. However, ambient fluid conditions after quartz deposition may be determined utilizing data from observations of secondary and pseudo-secondary inclusions, thereby providing constraints on the hydrothermal fluid properties prior to gold deposition.

There are two methods by which ambient fluid pressures can be determined. The first method utilizes the homogenization temperatures of aqueous fluid inclusions, combined with an independent temperature estimate, such as a stable isotope temperature of vein formation (cf. Shepherd, 1985). Equations derived by Brown and Lamb (1986) can then be applied to determine the pressures at which the inclusions were trapped.

The second method for calculating inclusion trapping pressure utilizes the temperature at which CO₂ homogenizes to a liquid combined with an independent temperature estimate. Lamb and Brown (1986) derived phase equilibrium equations which can be used to calculate the trapping pressures for CO₂ rich inclusions (Type Ia). Necking does not place the same limitations on pressure calculations utilizing CO₂-densities as it does for the homogenization of aqueous fluid inclusions. During necking and re-sealing of the inclusion, which generally occurs at temperatures greater than 100°C (Roedder, 1979), the CO₂ fluid remains a single phase. Consequently, there is no possibility of trapping variable CO₂ phases. Thus,

the necking of CO₂ rich inclusions should not cause a variation in measured ThCO₂, as is the case for Th of aqueous or H₂O-CO₂ inclusions

By utilizing the microthermometric data for aqueous and CO₂ inclusions, and the temperatures derived from stable isotope thermometry, constraints can be placed on the trapping pressure of Type I inclusions. Although stable isotopic data does not exist for the fluid inclusions event, data prior and post fluid inclusion formation allows for an estimation of the trapping pressure of Type I inclusions. Petrographic examinations sited in this chapter and Chapter 3, and stable isotopic data from Chapter 6 illustrate that Type I inclusions were trapped at a period of time prior to the gold mineralizing event (Stage II), but after main stage quartz deposition (Stage I; See Chapter 6 for full details on Stage I and II events). By utilizing the Stage I (430°C) and Stage II (360°C) fractionation temperatures (Chapter 6) it can be assumed that Type I inclusions formed at temperature bracketed between 360 to 430 °C. If this temperature range is utilized together with Type Ib inclusions median homogenization temperature of 212 °C, and salinities of 1.5 to 7.5 wt% equivalent NaCl (Appendix B and G), a 2.1 - 3.2 kb range of pressures can be calculated using equations of Brown and Lamb (1986). This corresponds to a depth of 7.3 - 11.2 km for lithostatic conditions.

For the CO₂ system, trapping pressures should be calculated utilizing the lowest ThCO₂ observed. This would represent the greatest trapping pressure, whereas higher ThCO₂ may represent the pressure of leakage and re-healing. Similar to the Type Ib inclusions, the Type Ia CO₂ inclusions were trapped at a temperature bracketed by Stage I and Stage II. This indicates that the trapping temperature for Type Ia can also be constrained to within the 360 - 430 °C range. For this

temperature range (360 - 430 °C), using the lowest ThCO_2 (18.0 °C), and by utilizing the equations of Brown and Lamb (1986), the trapping pressure can be constrained to between 1.7 - 2.0 kb. This pressure corresponds to a depth of 6-7 km for lithostatic conditions.

Based on the limited occurrence of high pressure metamorphic minerals (e.g. kyanite) within the region (Lewry, 1977), a 2 kb pressure is the most reasonable estimate of the trapping pressures of Type I inclusions, suggesting that the Seabee vein system was emplaced at a depth of approximately 7 km.

6.0 Isotope geochemistry

This chapter presents the results of stable and radiogenic isotope studies of the Seabee deposit. In the first part, the H,C,O and S stable isotope compositions of gangue minerals in the vein system are documented. In an attempt to constrain the age of vein formation and the Sr-isotope compositions of fluids, the second part reports $^{40}\text{Ar}/^{39}\text{Ar}$ ages for biotite and hornblende, and Sr-isotope data for hydrothermal vein phases.

In the discussion, the origin of the fluids and solutes are considered in the context of the temporal evolution of magmatism, metamorphism, and mineralization. Comparisons between the petrogenesis of the Seabee deposit, and other mesothermal gold deposits in the Trans-Hudson Orogen are discussed.

6.1 Stable isotopes

Stable isotope compositions of vein minerals were determined to constrain their temperature of formation, and to trace the origin of fluid(s) which precipitated the gangue minerals, and potentially the gold. As demonstrated in the section on vein petrography, the Seabee vein system contains two paragenetically distinctive sets of hydrothermal minerals; the first stage (Stage I) consists of quartz-tourmaline-pyrite, whereas the second stage (Stage II) consists of calcite-pyrrhotite-chalcopyrite-gold. Given the cross-cutting relationships of these mineral assemblages, each stage was

precipitated from distinct fluid events.

Resetting of the primary O and H isotope values of hydrothermal minerals by exchange with secondary fluids has become increasingly well documented. Hrdy (1994) demonstrated that the oxygen isotope composition of vein quartz may become reset during dynamic recrystallization in the presence of an isotopically distinct hydrothermal fluid. Similarly, Kerrich (1987) and Kerrich and Kamineneni (1988) have documented isotopic overprinting of carbonates in Archean vein deposits by post-Archean fluids. Kyser and Kerrich (1991) have shown that the hydrogen isotope compositions of fine grained hydroxysilicate minerals may undergo selective H-isotopic exchange with meteoric water at low temperatures, while still retaining the primary O-isotopic signature. This process generates distinctive vertical trends on δD vs. $\delta^{18}O$ diagrams. Accordingly, stable isotope compositions of minerals must be carefully evaluated for possible secondary exchange. Minerals which are highly resistant to H and O isotope exchange will preserve the isotopic character of the primary fluid, whereas phases that are easily reset record the isotopic composition of later fluid events.

Equilibrium stable isotope fractionations between cogenetic minerals may yield an approximation of the ambient temperature of mineral formation. Errors may stem from uncertainties in the calibration of mineral-water fractionation factors, analytical errors, or absence of equilibrium. Fractionation factors utilized in evaluating isotopic data are listed in Table 6.1. All stable isotope data are summarized in Appendix H.

6.1.1 Vein quartz

The $\delta^{18}O$ values of the quartz (Stage I and II) from various structures throughout the Seabee area are shown in Figure 6.1.

Table 6.1 - List of isotopic fractionation factors utilized in evaluating stable isotopic data. qtz=quartz; tourm=tourmaline; plag=plagioclase; py=pyrite; po=pyrrhotite; cpy= chalcopyrite

Mineral pair	1000 ln α	Reference
qtz-tourm	$1.0(10^6/T^2) + 0.39$	Kotzer et al., 1994
tourm-water	$-27.2(10^6/T^2)+28.1$	Kotzer et al., 1994
qtz-water	$4.10(10^6/T^2) - 3.7$	Bottinga and Javoy, 1973
qtz-water	$3.38(10^6/T^2) - 3.4$	Clayton et al., 1972
qtz-calcite	$0.60(10^6/T^2)$	Clayton et al., 1972 and O'Neil et al., 1969
qtz-plag	$0.5(10^6/T^2)$	Matthews, et al., 1983
calcite-water	$2.78(10^6/T^2) - 3.39$	O'Neil et al., 1969
py-cpy	$0.45(10^6/T^2)$	Kajiwara and Krouse, 1971
py-po	$0.3(10^6/T^2)$	Kajiwara and Krouse, 1971
po-cpy	$0.15(10^6/T^2)$	Kajiwara and Krouse, 1971

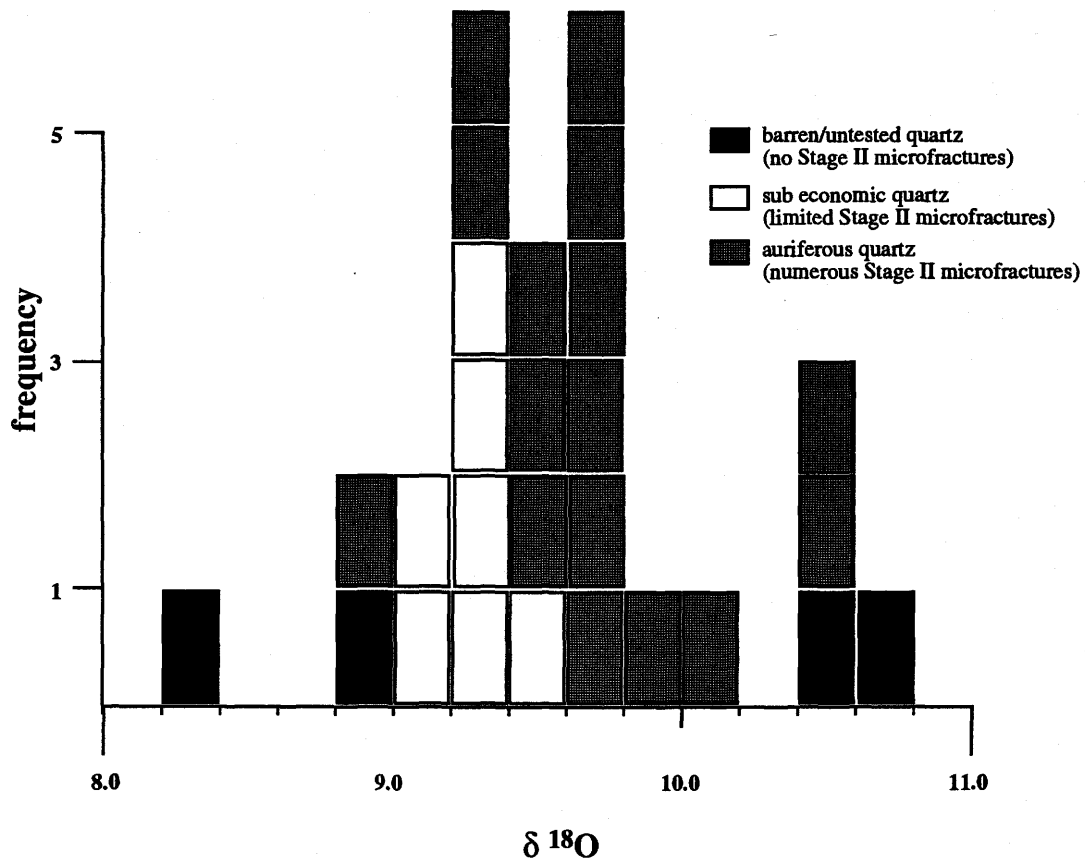


Figure 6.1 - Histogram of $\delta^{18}\text{O}$ quartz values from various structures within the Seabee mine claim block. Samples are grouped as to their economic potential, i.e. Barren or untested, sub economic, or auriferous. Data from Appendix H.

The veins can be classified into three types based on gold content of the shear structures: barren or untested (East Boundary Splay A and C, and Zone 666) containing limited or no Stage II microfractures, sub-economic (Zones 11,14,15) containing sparse Stage II microfractures, and auriferous (Zones 2 and 5) containing numerous Stage II microfractures. Generally, auriferous quartz ranges from 9.0 to 10.6‰, sub-economic quartz varies from 9.0 to 9.5‰, and barren/untested ranges from 8.4 to 8.9‰ and 10.4 to 10.6‰.

Quartz from one untested intersection, the East Boundary Splay C, has $\delta^{18}\text{O}$ values of 10.4 and 10.6‰. These values are similar to the auriferous $\delta^{18}\text{O}$ values, and may indicate the interval represents an economic intersection. Drill core gold assays from nearby drill holes are in excess of 50 g/tonne. In addition, the quartz is associated with biotite-chlorite-albite-pyrite-pyrrhotite with minor Stage II microfractures, an assemblage indicative of gold mineralization. Thus, auriferous fluids may have been passed throughout portions of the East Boundary structures.

Four replicate analyses of vein quartz from the Zone 2b-100 stope showed a total variation of 0.4‰, which is greater than the reproducibility of ± 0.2 ‰ expected for the BrF_3 silicate extraction line. This isotopic variation is the result of small scale isotopic heterogeneities within the vein quartz. Such variations in $\delta^{18}\text{O}$ quartz within a single mesothermal gold vein has been attributed to changes in fluid temperature, or variations in the $\delta^{18}\text{O}_{\text{H}_2\text{O}}$, or some combination of the two (Kerrick, 1987).

6.1.2 Microfracture quartz

Numerous microfractures were documented throughout the Seabee vein structure, especially in the high grade intersections. Quartz from a Stage II microfracture from Zone 2 (Zone 2b-100

stope) has a $\delta^{18}\text{O}$ value of 10.6‰ . This is the highest $\delta^{18}\text{O}$ value for vein quartz from the Seabee deposit, and compares to the range of 9.3 to 10.0‰ for vein quartz in ore bodies elsewhere in the deposit. Four samples of quartz from within 2 to 10 cm of the microfracture have values of 9.4 to 9.8‰ , suggesting a "distinct" fluid was present in the fracture in terms of temperature, or $\delta^{18}\text{O}_{\text{H}_2\text{O}}$. During microfracture formation, in the presence of a distinct fluid, there was localized re-crystallization of the quartz vein system. This distinct fluid event resulted in quartz with elevated $\delta^{18}\text{O}$ values of 9.6 to 10.5‰ . Systematic sampling shows variations in the $\delta^{18}\text{O}$ values of quartz within a sample, most likely because microfractures represent only a limited volume ($< 10\%$) of the total quartz in the vein system. Thus, 1 to 2‰ variation in $\delta^{18}\text{O}$ values can be expected from quartz randomly collected from the vein, as a greater percentage of microfracture quartz may be present in any given sample.

Micro-sampling of vein material from a single sample (Zone 2b-100 stope) showed Stage I quartz may be as much as 1.0‰ depleted relative to microfracture quartz. Thus, primary quartz, or Stage I quartz, is approximately 9.0‰ , whereas microfracture quartz, or Stage II quartz, has values greater than 10.5‰ .

6.1.3 Tourmaline

Tourmaline occurs in two distinct varieties based on petrographic characteristics: Stage I tourmaline is coarse grained, unaltered, opaque, euhedral and occurs only in the wider portions of the Zone 2, whereas Stage II tourmaline is fine grained, altered, translucent, prismatic, and occurs in samples containing numerous Stage II microfractures.

Both stages of tourmaline are variably zoned. Proximal to microfractures, Stage I tourmaline becomes significantly

altered (brown-blue in plane polarized light) to form Stage II tourmaline, whereas Stage I tourmaline distal from the fractures is less altered, having a green-blue appearance in plain polarized light.

This variation in tourmaline mineralogy is also reflected in their oxygen isotope compositions (Appendix H). The differences in oxygen isotope composition of tourmaline from specific structures are illustrated in Figure 6.2. The histogram groups tourmaline as unaltered tourmaline from surface and Zone 2 (2b-100 stope), and altered tourmaline collected from throughout the deposit.

Dark unaltered tourmaline (Stage I) has $\delta^{18}\text{O}$ values ranging from 6.5 to 6.9‰, whereas the translucent altered tourmaline (Stage II) has distinctively higher $\delta^{18}\text{O}$ values from 7.2 to 7.8‰. Unaltered tourmaline has a δD value of -50‰, whereas samples of altered tourmaline have values of -61, -66, and -80‰. These results suggest that the primary stable isotope composition of tourmaline from the Seabee deposit was variably reset by a later fluid event. Assuming that coarse grained minerals are more likely to retain their primary isotopic signature (Kyser and Kerrich, 1991), the opaque, unaltered tourmaline from the Zone 2b-100 stope would represent the oxygen isotope composition of Stage I fluid, whereas translucent tourmaline records the oxygen isotopic composition of a later fluid event (Stage II).

6.1.4 Vein feldspar *

Certain sub-economic structures, such as Zones 11 and 14, contain a significant modal proportion of hydrothermal feldspar. The feldspar appears to be perthitic microcline having lamella twinning, however X-ray diffraction analysis of mineral separates indicate that some of the feldspar may be albitic in composition. Accordingly, this type of feldspar may

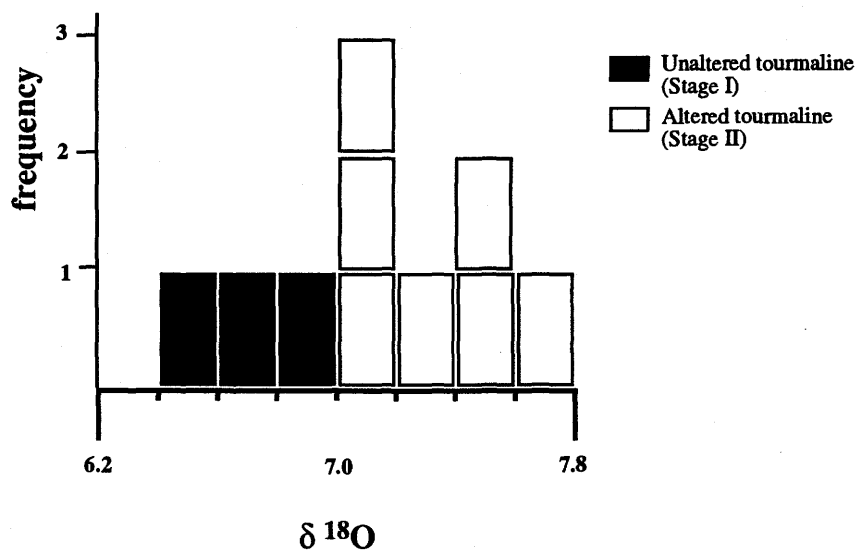


Figure 6.2 - Histogram of $\delta^{18}\text{O}$ values of unaltered and altered tourmaline from the Seabee deposit. Data from Appendix H

be "checker board albite".

The isotopic composition of albite from Zones 11 and 14 range from 8.9 to 9.6‰ (Appendix H). Quartz-albite fractionation correspond to a temperatures of 950 °C for Zone 14, based on the equations of Matthews et al., (1983), which is far too high for typical mesothermal systems. Zone 11 has a negative quartz-albite fractionation. Hence the negative fractionation, and high fractionation temperature for quartz and feldspar from Zones 11 and 14, indicate that the two mineral phases are not in isotopic equilibrium, and are not useful in evaluating hydrothermal conditions. Furthermore, albite $\delta^{18}\text{O}$ values are more scattered than the uniform $\delta^{18}\text{O}$ values for quartz, indicating that albite probably has undergone preferentially exchange with later fluids.

6.1.5 Carbonate

Carbonates are generally associated with Stage II mineralization of chalcopyrite-pyrrhotite and gold (Plate 3.1).

If hydrothermal temperatures from 300 to 400 °C can be assumed for typical mesothermal deposits (cf. Kyser et al., 1986; Fedorowich et al., 1991; Ibrahim and Kyser, 1991; Ansdell and Kyser, 1992; Fayek et al., 1993; Hrdy, 1994), then the corresponding $\delta^{18}\text{O}$ values for carbonate in equilibrium with the Stage II microfracture quartz (10.5‰) should be 8.4 to 9.3‰.

Two types of carbonate were observed at the Seabee deposit: (1) pink coarse grained euhedral carbonates commonly seen at greater depths (Zone 2b-325 stope), although pink calcite may occur at shallower depths (Zone 14, or Zone 2h25 stope) and (2) white fine grained carbonate typically seen at shallow

depths (Zone 2b-100 and Zone 5-1-60 stopes).

The pink carbonates have values from 8.4 to 8.9‰, whereas white carbonates (Zone 2b-100 stope) have $\delta^{18}\text{O}$ values of 21.6 to 21.7‰. Pink carbonates have $\delta^{18}\text{O}$ values within the estimated range to be in isotopic equilibrium with microfracture quartz (Stage II). In contrast, the fine grained white carbonates are distinctly more $\delta^{18}\text{O}$ -rich, suggesting that these carbonates were either precipitated by, or equilibrated with post mineralizing fluids. Similar isotopic overprinting of vein carbonates has also been documented in Archean deposits (cf. Kerrich, 1989b).

The $\delta^{13}\text{C}$ values for white and pink calcite are constrained to narrow ranges of -11.2 to -11.3‰, and -5.9 to -7.8‰ respectively. The 5‰ difference in the C-isotopic composition between pink and white calcite indicates that, like the O-isotopic composition, white calcite was precipitated by, or equilibrated with a post-mineralizing fluid. Consequently, pink carbonate may have preserved the C-isotopic composition of the hydrothermal event (Stage II), whereas white calcite represents a later post-hydrothermal fluid event(? Stage III ?).

Different lithological reservoirs have distinct but sometimes overlapping C isotope compositions. For example, the average $\delta^{13}\text{C}$ of igneous, metamorphic and sedimentary lithologies is approximately -7.0‰ (Hoefs, 1987). Precambrian sedimentary rocks range from -14 to -15‰ (Faure, 1986), and mantle carbon varies from -3 to -8‰ (Kyser, 1986). Average crustal C is considered to be -5 ± 3 ‰ (Ohmoto and Rye, 1979). Pink carbonate from the Seabee deposit with values of -5.9 to -7.8‰ indicates that the sources of the carbon was either mantle or crustal, or a mixture of the two. White carbonate, with $\delta^{13}\text{C}$ values of -11‰ indicates that the post mineralizing

fluid partly or fully equilibrated with Precambrian lithologies or acquired depleted C from surface organic material (cf. Kerrich and Kamineni, 1988).

6.1.6 Sulphides

Sulphur isotope compositions of vein sulphides from the Seabee deposit were measured. The results are recorded in Appendix H and summarized in Figure 6.3. Separates of pyrite, chalcopyrite and pyrrhotite were obtained from the Zone 2b-100 stope and from various drill holes that intersected mineralization. Petrographically, pyrite exists in textural equilibrium with Stage I quartz and tourmaline, whereas chalcopyrite-pyrrhotite is sited in Stage II microfractures, particularly where the fractures crosscut the pyrite. Thus, it is assumed that chalcopyrite and pyrrhotite precipitation is contemporaneous with gold mineralization, and that the pyrite is related to the primary silicate paragenetic assemblage of quartz-tourmaline.

Pyrite $\delta^{34}\text{S}$ values are variable ($\delta^{34}\text{S} = -0.9$ to 3.2), return negative fractionations values compared with chalcopyrite and pyrrhotite, and hence appear not to be in isotopic equilibrium with chalcopyrite-pyrrhotite (Figure 6.3). This variation of S-isotope composition, as compared to the tight grouping of $\delta^{34}\text{S}$ for chalcopyrite and pyrrhotite, is interpreted to result from resetting and re-crystallization of pyrite during Stage II gold mineralizing event.

$\delta^{34}\text{S}$ values for chalcopyrite and pyrrhotite range from 3.4 to 3.7‰ . This narrow range suggests that both sulphide minerals precipitated in isotopic equilibrium (Figure 6.3). Coexisting chalcopyrite and pyrrhotite would have near identical $\delta^{34}\text{S}$ values at temperatures of greater than 360 °C , because the equilibrium fractionation between the two phases would be approximately 0.37‰ (cf. Kajiwara and Krouse, 1971). These

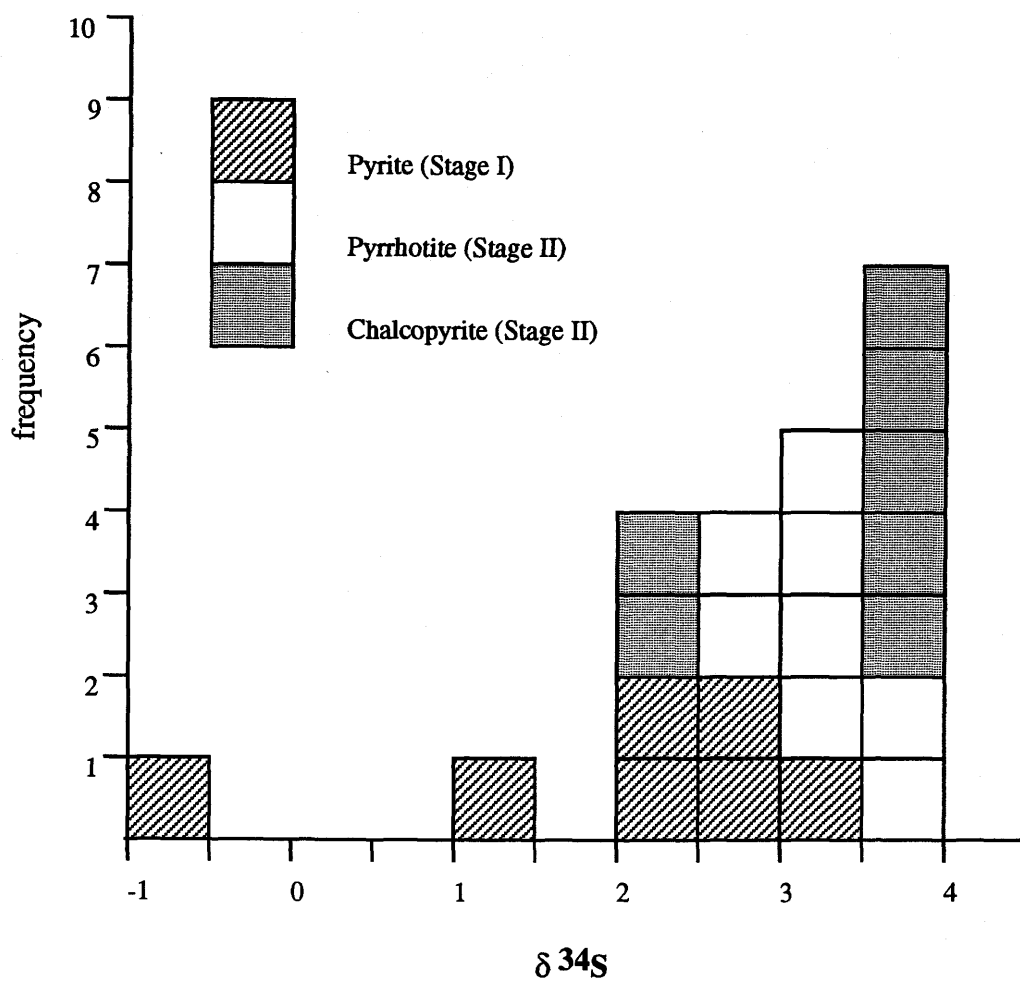


Figure 6.3 - Histogram of $\delta^{34}\text{S}$ values for various sulphide phases from the Seabee deposit.

similar $\delta^{34}\text{S}$ values would further suggest that chalcopyrite and pyrrhotite precipitated at a minimum temperature of 360°C.

6.2 Fluid events and fluids in equilibrium with minerals

As discussed in the previous section, numerous phases within the hydrothermal mineral assemblage of the Seabee vein system have been partly or wholly reset during subsequent fluid events. This section attempts to determine the number, temperature, and isotopic compositions of the various fluid events preserved within the Seabee deposit.

Table 6.2 summarizes sequential development of mineral phases, which in turn may record the various fluid events. Individual fluid events are classified as Stages I and II, based on textural and isotopic overprinting of earlier mineral assemblages. Events are listed in order of relative time.

Hydrothermal quartz from barren structures (i.e. Zone 666, East Boundary A), which appears not to have interacted with the Stage II fluid, is assumed to represent the primary Stage I hydrothermal activity ($\delta^{18}\text{O}_{\text{qtz}} = 9.0\text{‰}$). Likewise, coarse, unaltered tourmaline is interpreted to represent Stage I tourmaline mineralization ($\delta^{18}\text{O}_{\text{tour}} = 6.6\text{‰}$, $\delta\text{D}_{\text{tour}} = -50\text{‰}$). The quartz-tourmaline and tourmaline-water isotope fractionation factors of Kotzer *et al.* (1994), and quartz-water fractionation factor of Bottinga and Javoy (1973) indicate an isotope equilibrium temperature of 430°C and a calculated $\delta^{18}\text{O}_{\text{H}_2\text{O}}$ of 5.2‰ and $\delta\text{D}_{\text{H}_2\text{O}}$ of -24‰ for the fluid associated with the Stage I minerals.

As was illustrated in sections 6.1.2 and 6.1.3, Stage II fluid interaction with Stage I quartz and tourmaline has changed their primary O-isotopic composition. If microfracture quartz ($\delta^{18}\text{O}_{\text{qtz}} = 10.5\text{‰}$) and altered tourmaline ($\delta^{18}\text{O}_{\text{tourm}} = 7.6\text{‰}$, $\delta\text{D}_{\text{tourm}} = -65\text{‰}$) are assumed to be in isotopic equilibrium,

Table 6.2 - Table of fluid events including the related mineralogy, O, H - compositions of individual phases, isotopic equilibrium temperatures for given fluid event, O, H - composition of fluids in equilibrium with minerals; Note: qtz=quartz; tour=tourmaline; cal=calcite; po=pyrrhotite; cpy= chalcopyrite.

Fluid Stage	Minerology	$\delta^{18}\text{O}$	δD	$\delta^{34}\text{S}$	T ($^{\circ}\text{C}$)	$\delta^{18}\text{O}_{\text{water}}$	$\delta\text{D}_{\text{water}}$
I	Primary Quartz	9.0			430 (qtz-tour)	5.2(1)	
	Primary Tourmaline	6.6	-50				
II	Microfracture Quartz	10.5			360 (qtz-tour)	5.4(1)	
	Altered Tourmaline	7.6	-65				
	Sulfide (Po-Py)			3.5	340*		
	Pink Carbonate	8.5			240-360(qtz-cal)	5.2(2)	

qtz-tour= quartz-tourmaline temperature calculated from fractionation factor derived by Kotzer et al., 1994

qtz-cal = quartz-calcite temperature calculated from fractionation factors derived by Clayton et al., 1972 and O'Neil et al., 1969

* = minimum fractionation of pyrrhotite-chalcopyrite calculated from fractionation factors derived by Kajiwara and Krouse, 1971

1= $\delta^{18}\text{O}_{\text{water}}$ calculated from quartz-water fractionation factor derived by Bottinga and Javory, 1973

2= $\delta^{18}\text{O}_{\text{water}}$ calculated from calcite-water fractionation factor derived by O'Neil et al., 1969

3= $\delta\text{D}_{\text{water}}$ calculated from tourmaline-water fractionation factor derived by Kotzer, et al., 1994

then a temperature of 360°C may be calculated by applying the quartz-tourmaline fractionation factor of Kotzer et al. (1994). Similarly, values of $\delta^{18}\text{O}_{\text{H}_2\text{O}} = 5.4\text{‰}$, and $\delta\text{D}_{\text{H}_2\text{O}} = -25\text{‰}$ can be calculated if the quartz-water and tourmaline-hydrogen isotope fractionation factors of Bottinga and Javoy (1973), and Kotzer et al. (1994) are applied.

Pink carbonate $\delta^{18}\text{O}$ values range from 8.4 to 8.9‰ and appears to be in isotopic equilibrium with Stage II quartz. If the combined isotopic fractionation factor for quartz-calcite (Clayton et al., 1972 and O'Neil et al., 1969) is applied, then a temperature range of 260 to 340 °C may be calculated. This is comparable to the 360 °C Stage II temperatures calculated using quartz-tourmaline fractionation factor of Kotzer et al., (1994). This indicates that there exists isotopic concordance between the mineral triplet of Stage II quartz, tourmaline, and carbonate.

In summary, Stage I and Stage II have similar O and H isotopic compositions, but the temperature between the two stages differs by approximately 70°C. Figure 6.4 illustrates the similarity of O and H isotope compositions of Stage I and Stage II. Also plotted on Figure 6.4 are the estimates of δD and $\delta^{18}\text{O}$ values of other mesothermal gold fluids (cf. Kyser et al., 1986; Fedorowich et al., 1991; Ibrahim and Kyser, 1991; Ansdell and Kyser, 1992; Fayek et al. 1993; Hrdy, 1994).

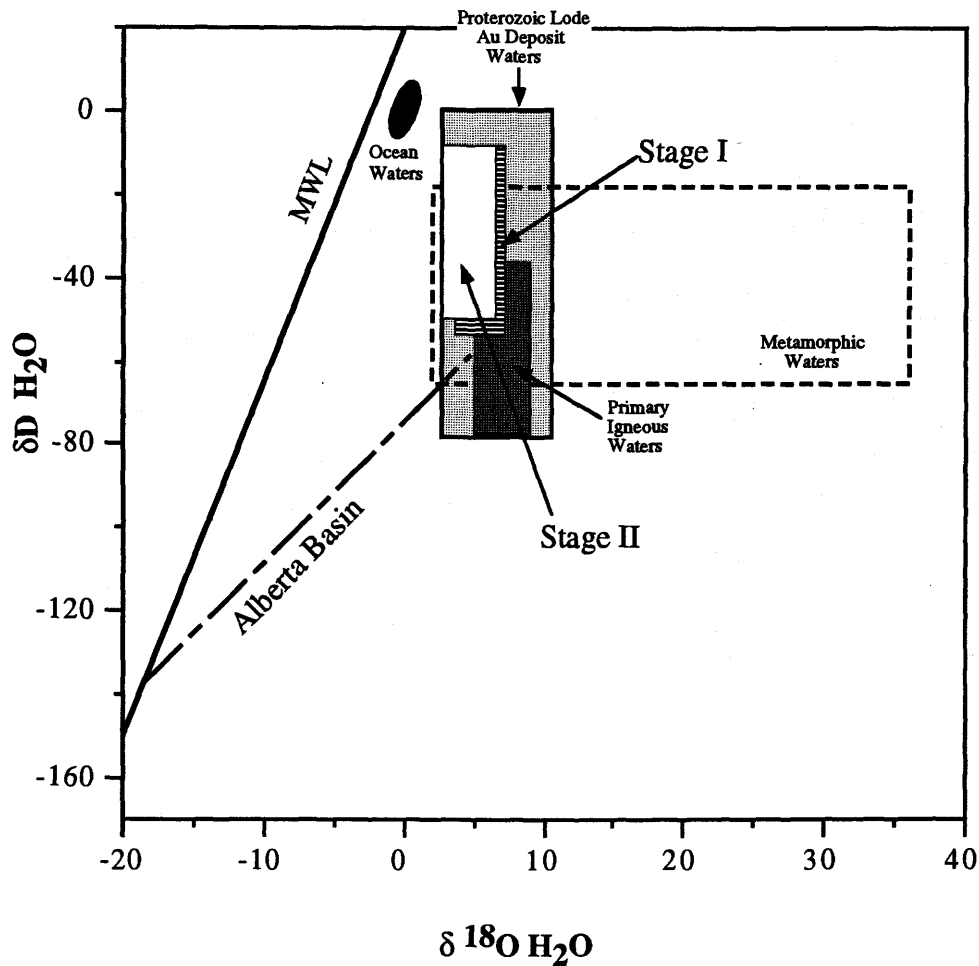


Figure 6.4 - Plot of $\delta^{18}\text{O H}_2\text{O}$ vs. $\delta\text{D H}_2\text{O}$. The dashed box outlines the isotopic composition of metamorphic waters, whereas the dark grey box represents the field of Primary Igneous Waters (from Taylor, 1987). Proterozoic mesothermal waters fall within the light grey box (cf. Kyser et al., 1986; Fedorowich et al., 1991; Ibrahim and Kyser, 1991; Ansdell and Kyser, 1992; Fayek et al., 1993; Hrdy, 1994). Plotted are the calculated δD , $\delta^{18}\text{O H}_2\text{O}$ values, including analytical error, for quartz-tourmaline mineral pairs of Stage I (striped box) and Stage II (white box).

6.3 Radiogenic isotopes

Pb-Pb, Ar-Ar, and Rb-Sr isotope compositions were measured to constrain the timing, and source characteristics of the gold mineralization. Zircons from the feldspar porphyry unit were used to determine the crystallization age of the latest known intrusive event and assess any possible genetic links between the feldspar porphyries and gold mineralization. Amphibole separates from gabbros of the Laonil Lake Intrusive Complex and biotite from the Seabee Shear Structure were analyzed by the $^{40}\text{Ar}/^{39}\text{Ar}$ step heating method to constrain timing of peak metamorphism and shear zone development. Initial Sr-isotope compositions were determined for vein mineral separates allowing potential source reservoirs of the gold mineralization to be identified.

6.3.1 Pb-Pb evaporation ages

Zircons were separated from a feldspar porphyry unit and analyzed using the modified Kober (1986,1987) Pb-evaporation technique of Ansdell and Kyser (1990). The $^{207}\text{Pb}/^{206}\text{Pb}$ ages of four zircons were measured (Appendix I). Three of the four zircons have $^{207}\text{Pb}/^{206}\text{Pb}$ ages ranging from 1886 ± 4 to 1872 ± 28 Ma, resulting in an average of 1877 ± 10 Ma. The fourth zircon has a higher $^{207}\text{Pb}/^{206}\text{Pb}$ age of 1911 ± 14 Ma.

Regional geochronology by Chiarenzelli (1989) indicates that quartz diorite phase of the Laonil Lake Intrusive Complex occurred at 1889 ± 9 Ma. Thus, the older zircon obtained for the feldspar porphyry most likely represents inheritance from the Laonil Lake Intrusive Complex, whereas the age of 1877 Ma represents the age of emplacement and crystallization of the porphyry.

6.3.2 $^{40}\text{Ar}/^{39}\text{Ar}$ ages

Amphiboles

Two amphibole separates were obtained from gabbro samples collected 50 metres from the shear zones (HbGb3, Amph-S128), and were analyzed by the $^{40}\text{Ar}/^{39}\text{Ar}$ step heating technique (Hanes, 1991). The $^{40}\text{Ar}/^{39}\text{Ar}$ spectra for the amphiboles are presented in Figures 6.5 and 6.6. Both samples illustrate disturbed spectra. Sample Amph-128 has an age of 1721 ± 17 Ma (Figure 6.5), whereas Sample HbGb3 has a maximum plateau age of 1634 ± 7 Ma (Figure 6.6).

Metamorphic titanites from various granitoid phases within the Glennie domain have U-Pb ages from 1780 to 1773 Ma (Chiarenzelli, 1989). Based on the closure temperature of 550 °C for titanite (Hanes, 1991), Chiarenzelli suggested that the Glennie domain passed below amphibolite facies conditions at ca. 1780 Ma, potentially constraining the time of peak-metamorphism for the Glennie domain to ca. 1800 Ma. With a similar 500 °C closure (Hanes, 1991) to that of titanite, amphibole $^{40}\text{Ar}/^{39}\text{Ar}$ ages of approximately 1780 Ma were expected, however both samples are 60 to 150 Ma younger. Younger ages and higher Ca/K ratios (Figure 6.7) indicate that the amphiboles may contain other minerals, or interacted with hydrothermal fluids during Stage I or II. Thus, amphiboles proximal to the Seabee deposit may not record the timing of peak-metamorphism, but rather indicate that the envelope of hydrothermal activity and alteration extends up to 50 metres from the shear zone.

Hydrothermal Biotite

To constrain the timing of mineralization, $^{40}\text{Ar}/^{39}\text{Ar}$ ages of biotite samples from the centre of Zone 5 (Biot-Sed; Figure 6.7), and from an uneconomic portion of the potassic alteration halo of Zone 2 (Biot-S128; Figure 6.8) were

Amph-S128

Run: JF-53 103/4
Date: December 19 1992

Mass: 20.6 mg
J Value: 0.02311

Total ^{39}Ar : 0.851 E-8 cm³ NTP Approx. 0.25% K
Integrated Age 1661.7 +/- 23.4 Ma
Plateau Age: 1703.2 +/- 20.2 Ma (96.1% of ^{39}Ar , steps marked by *)

Temp C	40/39	36/39	37/39	Vol 39A E-8 cm ³	Fraction ^{39}Ar	% ^{40}Ar Rad.	Age Ma	+-	Error 2 sigma
600	37.072	0.0629	0.540	0.033	0.039	46.63	641.8	+-	103.5
* 700	71.734	0.0249	0.641	0.066	0.077	66.73	1644.6	+-	24.6
* 800	72.827	0.0161	3.543	0.032	0.038	63.46	1711.2	+-	122.8
* 900	72.004	0.0131	8.016	0.147	0.173	64.62	1720.9	+-	17.0
* 1000	69.160	0.0061	14.021	0.474	0.557	66.53	1710.4	+-	10.3
* 1200	72.831	0.0263	11.923	0.096	0.115	66.33	1678.3	+-	35.7

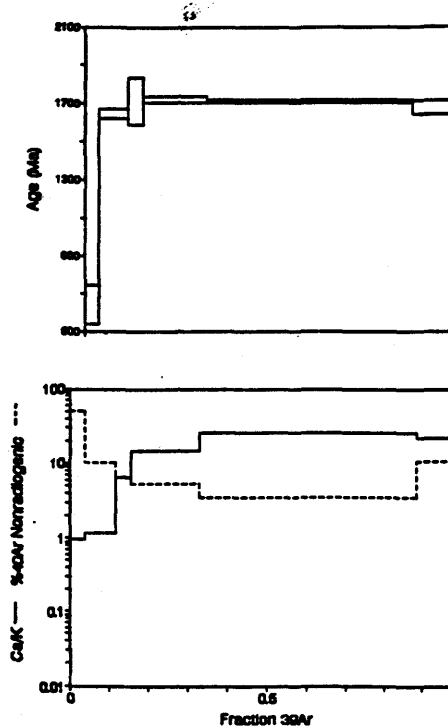


Figure 6.5 - $^{40}\text{Ar}/^{39}\text{Ar}$ data for amphibole obtained from meta-gabbro from the Laonil Lake Intrusive Complex near Zone 2 of the Seabee deposit.

HbGb3

Run: JF-52 103/35
 Date: December 19 1992

Mass: 60.6 mg
 J Value: 0.023 ± 2

Total ^{39}Ar : 1.472 E-8 cm³ NTP
 Integrated Age 1491.8 ± 16.1 Ma

Approx. 0.15% K

Temp C	40/39	36/39	37/39	Vol ^{39}Ar E-8 cm ³	Fraction ^{39}Ar	% ^{40}Ar Rad.	Age Ma	±	Error 2 sigma
600	58.418	0.0183	1.382	0.288	0.182	80.28	1445.3	±	8.3
700	58.438	0.0333	8.907	0.088	0.058	72.08	1213.0	±	32.1
800	48.514	0.0352	10.728	0.079	0.054	78.55	1183.1	±	47.9
850	48.489	0.0440	14.788	0.045	0.031	72.02	1087.0	±	80.9
900	52.814	0.0234	28.284	0.088	0.080	88.93	1394.8	±	39.9
950	58.244	0.0314	31.432	0.151	0.102	84.08	1437.3	±	13.6
1000	64.799	0.0152	29.554	0.473	0.321	93.08	1633.9	±	6.8
1200	64.900	0.0198	32.010	0.282	0.192	91.07	1617.9	±	8.8

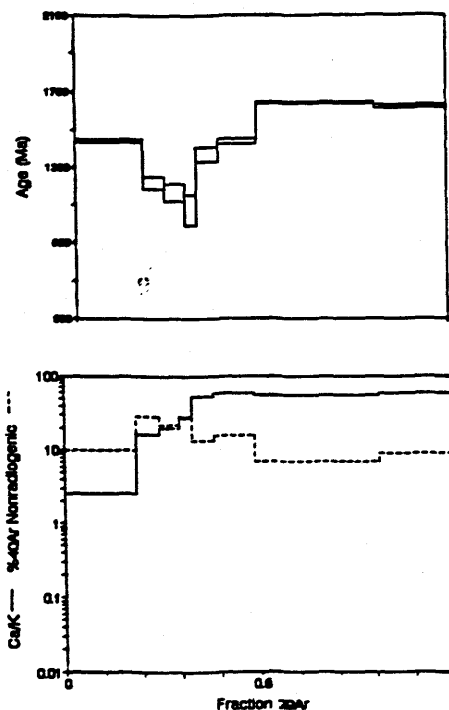


Figure 6.6 - $^{40}\text{Ar}/^{39}\text{Ar}$ data for amphiboles obtained from meta-gabbro from the Laonil Lake Intrusive Complex near Zone 2 of the Seabee deposit.

Biot-Sed

Run: JF-38 103/5
Date: December 5 1992

Mass: 24.6 mg
J Value: 0.02312

Total ^{39}Ar : 23.199 E-8 cm³ NTP Approx. 5.8% K
Integrated Age 1733.1 +/- 3.9 Ma
Plateau Age: 1735.7 +/- 3.6 Ma (98.6% of ^{39}Ar , steps marked by *)

Temp C	40/39	38/39	37/39	Vol ^{39}Ar E-8 cm ³	Fraction ^{39}Ar	% ^{40}Ar Rad.	Age Ma	+-	Error 2 sigma
500	68.442	0.0321	0.109	0.319	0.014	98.15	1551.3	+-	20.4
* 600	70.078	0.0017	-0.007	4.727	0.204	98.30	1729.5	+-	2.1
* 650	69.801	0.0013	-0.004	4.092	0.178	98.43	1728.6	+-	2.9
* 700	69.871	0.0011	-0.027	2.220	0.098	98.55	1729.0	+-	5.0
* 750	72.038	0.0029	-0.033	0.844	0.036	98.81	1754.8	+-	7.9
* 800	73.712	0.0059	0.023	0.825	0.036	97.82	1767.1	+-	10.5
* 850	74.184	0.0010	0.015	1.224	0.053	98.61	1797.2	+-	6.5
* 900	70.472	0.0008	0.004	3.293	0.142	98.88	1740.1	+-	3.7
* 1000	69.607	0.0007	-0.001	5.180	0.223	98.70	1728.5	+-	2.2
* 1200	71.189	0.0056	0.108	0.478	0.021	97.87	1728.8	+-	7.3

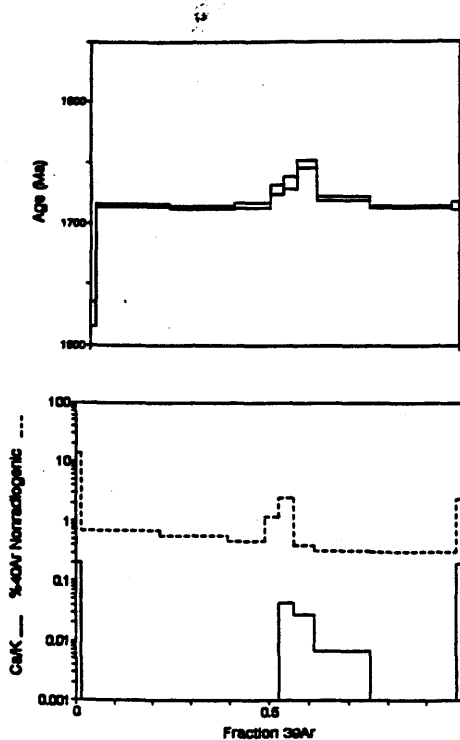


Figure 6.7 - $^{40}\text{Ar}/^{39}\text{Ar}$ data for biotite from an economic portion of Zone 5 of the Seabee deposit.

Biot-S128 Bt 60120

Run: JF-45 103/3
Date: December 17 1992

Mass: 11.7 mg
J Value: 0.02307

Total ^{39}Ar : 11.944 E-8 cm³ NTP Approx. 6.2% K
Integrated Age 1705.0 +/- 4.3 Ma
Plateau Age: 1738.4 +/- 3.7 Ma (85.1% of ^{39}Ar , steps marked by *)

Temp C	40/39	36/39	37/39	Vol ^{39}Ar E-8 cm ³	Fraction ^{39}Ar	% ^{40}Ar Rad.	Age Ma	+-	Error 2 sigma
500	28.491	0.0438	0.298	0.087	0.007	54.57	552.8	+-	77.9
600	60.637	0.0028	0.008	1.693	0.142	98.63	1583.5	+-	4.1
* 650	69.721	0.0033	0.008	1.049	0.088	98.60	1713.5	+-	5.2
* 700	70.254	0.0011	0.000	1.025	0.088	98.53	1732.3	+-	3.0
* 800	71.874	0.0013	0.000	1.708	0.143	98.45	1758.5	+-	3.5
* 850	73.013	0.0027	0.000	0.749	0.063	98.91	1768.5	+-	6.7
* 900	72.486	0.0020	0.000	1.552	0.130	98.18	1763.5	+-	2.7
* 950	70.002	0.0008	0.000	2.282	0.191	98.65	1729.7	+-	3.3
* 1000	69.314	0.0021	0.048	0.724	0.061	98.10	1712.8	+-	5.3
* 1200	69.621	0.0027	0.022	1.078	0.090	98.65	1714.7	+-	2.0

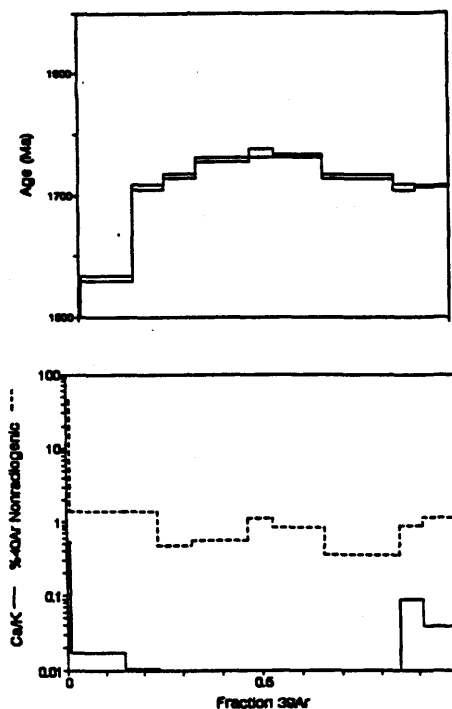


Figure 6.8 - $^{40}\text{Ar}/^{39}\text{Ar}$ data for biotite from the alteration envelope a few 100 metres from Zone 2 of the Seabee deposit.

determined. The spectra are disturbed, but much less so than those of the amphiboles. Sample Biot-Sed has a plateau age of 1736 ± 4 Ma, although a much older age is obtained from the centre of the spectra. This older $^{40}\text{Ar}/^{39}\text{Ar}$ age also corresponds to an anomaly in the Ca/K ratio, which is much higher than the low Ca/K ratio for pure biotite. These results are compatible with the interpretation that Ar was being liberated from a mineral phase other than biotite. Hornblende is likely the phase causing the outlier in the spectra, as biotite is an alteration product of the metamorphic hornblende (Cambell, 1986). The 1797 ± 7 Ma upper age of the anomaly is within the expected age range for post-peak metamorphism (ca. 1800 Ma), so that the outlier may represent a mineral phase that approximates the age of peak metamorphism. Recalculation of the plateau age excluding the outlier indicates a date of 1728 ± 5 Ma.

A different, more disturbed, age spectra is evident for biotite (Biot-S128) obtained from the alteration envelope of Zone 2. The 850 °C step has an $^{40}\text{Ar}/^{39}\text{Ar}$ age of 1769 ± 7 Ma, whereas adjacent high temperature and low temperature steps have younger ages. This is interpreted to be the result of partial resetting of the K/Ar systematics for the biotite, such that the older age represents the approximate age of closure of the biotite, and the younger age represents the time of resetting.

Ages of 1877 ± 10 were obtained for feldspar porphyries from $^{207}\text{Pb}/^{206}\text{Pb}$ evaporations of single zircons. The $^{40}\text{Ar}/^{39}\text{Ar}$ biotite ages obtained from the alteration assemblage are ca. 1769 and 1728 Ma, so that mineralization post dates porphyry crystallization by ca. 150 Ma, indicating that the porphyries were emplaced prior to the peak of hydrothermal activity. Therefore, a genetic link between the porphyries and mineralization as proposed by Helmstaedt (1986,1987) is

unlikely.

Timing of fluid events

Two major fluid events, Stage I and II, are recognized to have influenced the Seabee deposit. The timing of metamorphism, or post-peak metamorphism is constrained by the oldest age (1797 Ma) recorded in the Biot-Sed spectra, whereas hydrothermal activity (Stages I, and II) post dates metamorphism. However, placing absolute limits on the timing of these hydrothermal event(s) is less tractable.

Biotite samples from different locations within the shear zone system have distinctly different $^{40}\text{Ar}/^{39}\text{Ar}$ ages. Sample Biot-Sed from within the economic portion of Zone 5 has a calculated plateau age of 1728 ± 5 Ma. The corresponding stable isotope data for economic zones at Seabee indicate that these structures were overprinted by Stage II fluids, and the less robust mineral phases preserved the isotopic characteristics of the Stage II. Similarly, biotite from the economic portion of the shear zone is interpreted to have been affected by Stage II fluids, as it is also a less robust mineral phases. As a result, the age spectrum would then approximate the timing of Stage II (ca. 1730 Ma). Biotite from the barren portion of the alteration halo yielded an older upper plateau age of 1769 ± 7 Ma, although this $^{40}\text{Ar}/^{39}\text{Ar}$ spectrum also recorded partial resetting. Stable isotopic evidence (section 6.2) has shown that the barren portions of the structures preserve properties of the Stage I fluid event. Thus, the $^{40}\text{Ar}/^{39}\text{Ar}$ age of 1769 Ma would approximate the timing of the Stage I fluid event.

Of interest in both biotite $^{40}\text{Ar}/^{39}\text{Ar}$ spectra are the ages recorded by the lower temperature (500 to 600 °C) steps. In sample Biot-S128 the 600°C step yielded an age of 1564 ± 4 Ma,

whereas the 500 °C step for Biot-Sed returned an age of 1551 ± 20 Ma. These younger ages may represent the timing of a possible Stage III fluid event. Late resetting of the biotite by meteoric waters may have also occurred resulting in the 553 ± 78 Ma age for the 500 °C step for sample Biot-S128. Thus, hydrothermal biotite from the Seabee deposit records various ages from multiple fluid events.

6.3.3 Initial Strontium of hydrothermal vein phases

Systematic multi-element analyses of vein sulphides, such as pyrite, chalcopyrite, and pyrrhotite, by ICP-MS revealed that these phases contained measurable concentrations of strontium (0.58-0.61 ppm) with unmeasurable levels of Rb (see Appendix F). The source of the Sr is assumed to be from solid or fluid inclusions that are coeval with the precipitation of the hydrothermal vein phases. It is further assumed that these phases are pristine, and were not overprinted by late or secondary events. Because of the relatively low Rb/Sr ratios, it can be assumed that no significant radiogenic Sr was produced over geological time, and that the measured $^{87}\text{Sr}/^{86}\text{Sr}$ ratio would approximate the initial ratio of the hydrothermal fluid(s). Five phases comprising one tourmaline, one gold, two pyrrhotite, and one chalcopyrite were selected for Sr isotope analysis. The Sr isotope data is summarized in Appendix I

Tourmaline

A $^{87}\text{Sr}/^{86}\text{Sr}$ ratio of 0.702171 ± 23 (2σ) was obtained for Stage I tourmaline, and is taken to be representative of the initial Sr isotope ratio of Stage I fluids. Similar initial ratios have been obtained from other Trans-Hudson mesothermal deposits (cf. Ibrahim and Kyser, 1991; Ansdell and Kyser, 1992; Fayek et al., 1993; Hrdy, 1994).

Sulphides and gold

Stage II mineral phases such as pyrrhotite-chalcopyrite-gold yielded initial Sr isotope ratios from 0.711093 ± 87 to 0.7078 ± 12 (2σ), which are consistently higher than values expected for fluids in equilibrium with typical early Proterozoic (ca. 2000 Ma) rocks. Potential processes that could be responsible for the differences are as follows: (1) Fluids were derived from an older source region within the terrane, as the Glennie domain contains numerous windows of Archean material (Iskwatikan Lake gneisses 2748 - 2343 Ma, Hunter Bay Dome 2900 - 2486 Ma; Chiarenzelli, 1989), and/or (2) fluids may have selectively leached radiogenic Sr from Rb rich potassic phases resulting in elevated initial $^{87}\text{Sr}/^{86}\text{Sr}$ ratios.

In order to produce $^{87}\text{Sr}/^{86}\text{Sr}$ ratios greater than 0.7111, assuming an Archean source having $\text{Rb}/\text{Sr} = 0.15$ (Faure, 1986) and initial Sr ratio of 0.7010, the corresponding age of that Archean material in equilibrium with the Stage II fluid would be approximately 3500 Ma (Table 6.3). Given that prolific gold enrichment occurs in many Archean terranes, this older crustal material within the Glennie is an attractive source for Paleoproterozoic mesothermal gold.

In most Paleoproterozoic terranes of northern Saskatchewan, including the La Ronge, Glennie, and Flin Flon domains, petrographic observations of volcanic, sedimentary, and intrusive lithologies show that potassic and calcic phases (dominantly feldspars) generally show some retrograde alteration to a saussurite-muscovite assemblage. This implies that there were fluids active regional within the Trans-Hudson (i.e. Stage II). In this model, elevated Sr isotope ratios of 0.7111 could have been generated if auriferous fluids of Stage II leached Rb rich phases having a Rb/Sr ratio of > 0.9 (Table 6.3). This suggests that the source of the gold for the Seabee

Table 6.3 - Sample Rb/Sr isotope calculation of fluids in equilibrium with Archean Crustal material and fluid preferentially leaching Proterozoic K+ phases. All equations and data obtained from Faure (1986).

- $^{87}\text{Sr}/^{86}\text{Sr} \cong (^{87}\text{Sr}/^{86}\text{Sr})_i + (^{87}\text{Rb}/^{86}\text{Sr})\lambda t$ (8.11; Faure, 1986)

- $^{87}\text{Rb}/^{86}\text{Sr} = (\text{Rb}/\text{Sr}) \times \frac{\text{Ab } ^{87}\text{Rb} \times \text{WSr}}{\text{Ab } ^{86}\text{Sr} \times \text{WRb}}$ (8.4; Faure, 1986)

-or $^{87}\text{Rb}/^{86}\text{Sr} \cong (\text{Rb}/\text{Sr}) \times \frac{\text{Ab } ^{87}\text{Rb}}{\text{Ab } ^{86}\text{Sr}}$

-then $^{87}\text{Sr}/^{86}\text{Sr} \cong (^{87}\text{Sr}/^{86}\text{Sr})_i + [\text{Rb}/\text{Sr} \times (\text{Ab } ^{87}\text{Rb}/\text{Ab } ^{86}\text{Sr})]\lambda t$

-or $t \cong \frac{^{87}\text{Sr}/^{86}\text{Sr} - (^{87}\text{Sr}/^{86}\text{Sr})_i}{[\text{Rb}/\text{Sr} \times (\text{Ab } ^{87}\text{Rb}/\text{Ab } ^{86}\text{Sr})]\lambda}$

-if $\text{Ab } ^{87}\text{Rb} = 27.8346$; $\text{Ab } ^{86}\text{Sr} = 9.87$ or $\text{Ab } ^{87}\text{Rb}/^{86}\text{Rb} = 2.82012$ (Faure, 1986)

-then $t \cong \frac{^{87}\text{Sr}/^{86}\text{Sr} - (^{87}\text{Sr}/^{86}\text{Sr})_i}{[\text{Rb}/\text{Sr} \times 2.82012]\lambda}$

Archean Crust

-given: $\text{Rb}/\text{Sr} = 0.15$, $(^{87}\text{Sr}/^{86}\text{Sr})_i = 0.701$, $^{87}\text{Sr}/^{86}\text{Sr} = 0.711632$, $t_{\text{crust}} = t_0 + t_{\text{fluid event}}$, $t_{\text{fluid event}} = 1730 \text{ Ma}$

$$t_0 \cong \frac{(0.711632) - (0.701)}{(0.15) \times (2.82012) \times (1.42 \times 10^{-11})}$$

$$t_0 \cong 1770 \text{ Ma}$$

$$t_{\text{crust}} = 1770 \text{ Ma} + 1730 \text{ Ma}$$

$$t_{\text{crust}} = 3500 \text{ Ma}$$

Fluids leaching Proterozoic K+ phases

-given: $\text{Rb}/\text{Sr} = 0.9$, $(^{87}\text{Sr}/^{86}\text{Sr})_i = 0.702$, $^{87}\text{Sr}/^{86}\text{Sr} = 0.711731$, $t_{\text{crust}} = t_0 + t_{\text{fluid event}}$, $t_{\text{fluid event}} = 1730 \text{ ma}$

$$t_0 \cong \frac{(0.711632) - (0.702)}{(0.9) \times (2.82012) \times (1.42 \times 10^{-11})}$$

$$t_0 \cong 268 \text{ Ma}$$

$$t_{\text{crust}} = 268 \text{ Ma} + 1730 \text{ Ma}$$

$$t_{\text{crust}} = 1998 \text{ Ma}$$

deposit may have been Paleoproterozoic host rocks of the Glennie domain.

7.0 Ore genesis and fluid history of the Seabee gold deposit

The objective of this study was to determine the geological framework of the Seabee deposit, apply various techniques of analytical geochemistry in order to formulate an appropriate genetic model for gold mineralization of the deposit, and then to ascertain the P-T-fluid history within the north-central Glennie domain.

Numerous lines of evidence for establishing a genetic model were present at all levels of the geological investigation. The evidence is summarized as follows:

- (1) Numerous shear structures were delineated during routine lithological mapping of the Seabee claim block (Figure 3.1), all of which contain high gold content. To a first approximation zones of high strain control the distribution of gold.
- (2) Underground mapping showed that economic zones of mineralization have a steep westerly plunge, and ore is focused at intersections of shear structures, or dilational jogs.
- (3) On surface, in proximity to shear structures, deformed dykes or intrusive units have been progressively rotated, demonstrating that the shearing involved components of both coaxial and non-coaxial deformation.

- (4) Trace-element systematics of the least-altered and deformed dykes outside the shear zones confirmed a felsic, intermediate, and two varieties of mafic dykes, based on Cr, Ni Al, and HREE inter-element relationships.
- (5) Information from fluid inclusions, together with stable isotope data have shown that the quartz and related gangue minerals precipitated at temperatures of > 360 °C, and at depths of approximately 7 km.
- (6) Radiometric dating of zircons from host rock (porphyries), and dates obtained from alteration minerals demonstrates that gold mineralization post-dated the felsic intrusive events by ca. 150 Ma, and peak metamorphism by 70 Ma. These age relationships indicates that felsic porphyries were solidified host rocks by the onset of hydrothermal activity, and were not genetically involved in ore genesis via an orthomagmatic process.

All the above points, i.e. gold hosted by shear zones, ore focused at dilational jogs, lithologies focusing shearing, high fluid pressures, and post-peak metamorphic timing, collectively are consistent with the mesothermal lode gold model (cf. Colvine, 1988; Groves *et al.*, 1988; Hodgson and Hamilton, 1988; Kerrich, 1989b). Other proposed genetic models listed in Chapter 1 can be ruled out with a high degree of confidence.

In addition to helping to determine a genetic model for gold mineralization at the Seabee deposit, fluid inclusion, stable isotope, and radiogenic data allow for constraints to be placed on the fluid history of the area. Mineral phases from host rocks, alteration assemblages, mineralization, and post alteration assemblages give a "record" of fluid events which have affected the region over time. This study has shown that

mineralization was not due to a single hydrothermal event after which the deposit became a closed system. Rather, the mineralogy and isotope data demonstrate that the deposit was a dynamic open system with the various vein mineral phases recording fluid events depending on: (1) volume of fluid present, (2) dynamic deformation in the presence of a fluid, (3) grain sizes of hydrothermal minerals, (4) the closure temperature of the given phase, and (5) the resistance that minerals have to re-equilibration with subsequent fluid activity.

Stable isotope analyses of quartz and tourmaline show that the primary minerals were locally altered. For example, Stage I and II quartz differ by approximately 2‰, although the isotope fractionation factors show that the $\delta^{18}\text{O}_{\text{H}_2\text{O}}$ values of Stage I and II fluids are similar. This isotopic resetting, together with the lack of any definable primary fluid inclusions suggest that hydrothermal activity and deformation continued after precipitation of the primary phases of Stage I, and that fluids continued to be active in the structures (Stage II) during cooling and uplift of the Glennie domain.

From the data collected during the course of this research a Temperature-time (Tt) path can be constructed for the north central Glennie domain, which includes the crystallization age of the youngest host rock through to the latest fluid event (Figure 7.1). The Tt path demonstrates that hydrothermal (Stage I and Stage II) activity was post-peak metamorphic, and that hydrothermal fluid(s) continued to be active in the shear zones over a 30 Ma year period. Stage I can be characterised by $T = 430 \text{ }^\circ\text{C}$, $\delta^{18}\text{O} = 5.2\text{‰}$, $\delta\text{D} = -30\text{‰}$ and $^{87}\text{Sr}/^{86}\text{Sr} = 0.702171 \pm 23$. The Stage II event has similar T, P, $\delta^{18}\text{O}$, and δD values, but differs in temperature ($T=360 \text{ }^\circ\text{C}$) and the $^{87}\text{Sr}/^{86}\text{Sr}$ initial ratio (0.711-0.707).

The O - isotope composition of white carbonate, and lower

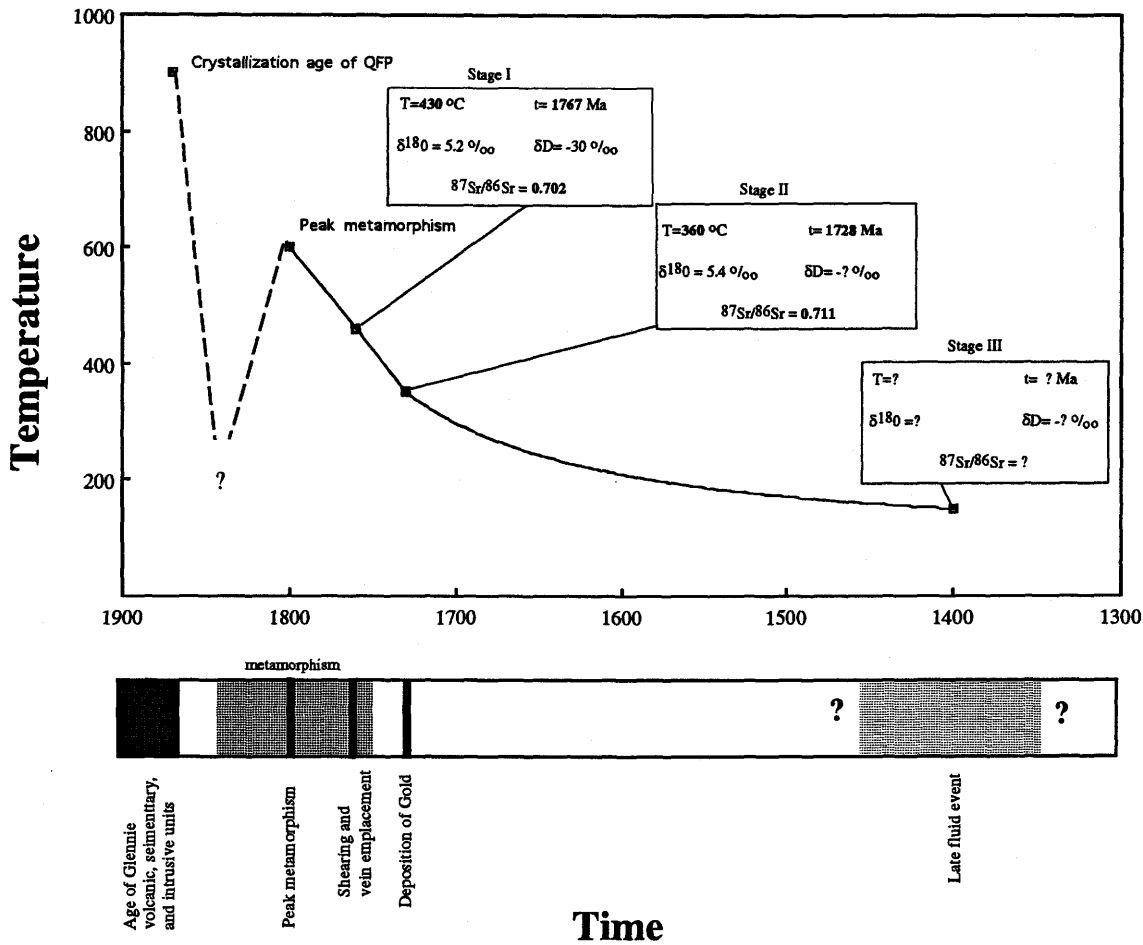


Figure 7.1 - Temperature-time path for the Seabee deposit. Included are three fluid events with the characteristics of each obtained from stable and radiometric isotope data. Dashed line indicates that the region under went cooling prior to metamorphism, although to an undetermined temperature and at an unknown time.

temperature step Ar-Ar ages in the biotite, suggest that a later low temperature Stage III fluid event occurred 240 Ma after the Stage I events.

7.1 Gold in the Glennie domain

The above fluid history, when interpreted in terms of the siting of gold, has far-reaching implications for the style of mineralization at Seabee, and the potential for other gold deposits in the Glennie domain. As was demonstrated in Chapter 3, gold is associated with minerals that occur late in the paragenetic sequence (Stage II microfracture quartz-tourmaline-sulphides-gold). The temperature, timing, and fluid characteristics of gold precipitation can thus be linked to the characteristics of the Stage II fluid event.

As was demonstrated in the Tt diagram, Stage I and II differ by less than 80 °C in temperature (Figure 7.1). This raises the question as to why gold is not associated with Stage I at the Seabee deposit. The higher temperature of Stage I may be a clue to the absence of gold. Typically gold is thought to be transported as a bisulphide $\text{Au}(\text{HS})_2^-$ complex (Mikucki and Groves, 1990; and references therein), and the stability of this complex peaks at 350 °C (Figure 7.2; Shenberger, and Barnes, 1989; Hayashi and Ohmoto, 1991). Above temperatures of 350°C the thermodynamic data base becomes limited, but Mikucki and Groves (1990) suggested that the gold bisulphide complex becomes less important at higher temperatures, due to the divergence of $\text{pK}_{\text{H}_2\text{S}}$ (stability constant for bisulphide complexes) from the neutral pH values. They go on to suggest that an increase in alkalinity is needed to maintain gold solubility at higher temperature. Based on fluid inclusion studies of mesothermal gold deposits (cf. Colvine, 1988; Groves et al., 1988; Hodgson and Hamilton, 1988; Kerrich, 1989b), high alkalinity is not a typical characteristic. An alternative gold complex, such as chloride-complexes, is

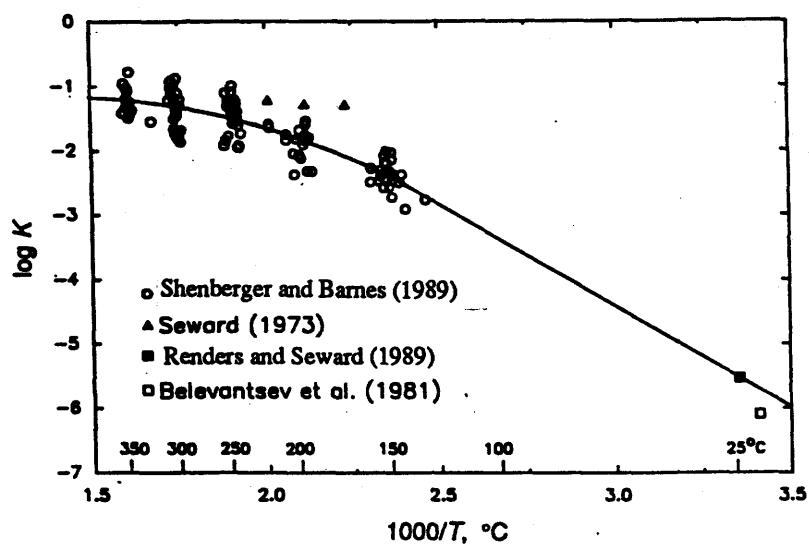


Figure 7.2 - The dependence of $K_{\text{Au}(\text{HS})_2^-}$ on temperature. Each data point (open circles) from Shenberger and Barnes (1989) represents an equilibrium constant calculated from individual or replicate measurements of gold solubility at the given temperature. The data of Seward (1973), Renders and Seward (1973), and Belevantsev *et al.* (1981) are their averaged equilibrium constants at each temperature (after Shenberger and Barnes, 1989)

required to transport gold at higher temperatures (Mikucki and Groves, 1990).

At the Seabee deposit this temperature effect on bisulphide complexes can be used to explain the absence of gold associated with the Stage I event. During Stage I, ambient temperatures were approximately 430 °C, which places the fluid beyond the peak stability for gold-bisulphide complexes. Thus, the temperature of Stage I was not amenable to gold transport. By the onset of Stage II, the fluid temperatures subsided to 360°C, which is close to the maximum stability constant for gold complexing (Figure 7.2). In a ca. 350 °C environment the potential for gold transport is high, and this cooler auriferous fluid would be capable of forming a significant deposit, given a suitable precipitation mechanism.

7.2 Implications for exploration

The above conclusion has major implications for exploration for gold in the Glennie domain. This thesis would suggest that hydrothermal fluids must cool to within a limited thermal range before becoming "auriferous". As a result, explorationists should be conscious of the geo-thermal history of the Glennie before planing an exploration programs.

In addition to a gold enriched fluid, the system needs an effective precipitation mechanism or "trap" to form a gold deposit. Petrographic relationships have shown that auriferous fluid interacting with pyrite was the mechanism by which the gold was precipitated. Furthermore, pyrite tends to be confined to areas of dilation, i.e. dilational jogs. During early shear zone development, zones of dilation were important in controlling the location of Stage I veins and Stage I pyrite. As the structures were reactivated, the Stage II fluids were focused through microfractures in the system, and Stage II gold was precipitated within the pyrite rich portions

of Stage I veins. Thus, by understanding the above controls on ore distribution explorationist can focus their efforts on areas (as sited above) of greater potential, and ignore other areas of low potential.

This study has a few implications for general gold exploration. They are summarized as follows:

- (1) The Stage I event, although not economic at Seabee, still represents a major fluid event depositing its own distinctive mineral assemblage. There is no reason why this fluid could not have contained auriferous components, and precipitated a significant deposit under more favourable conditions elsewhere. In a lower temperature metamorphic terrane the Stage I fluid could have been a significant ore-forming fluid.
- (2) The late Stage II ca. 360 °C fluid event is of primary importance to explorationists, given that fluids produced the gold deposit. Detailed studies and regional programs should focus on constraining the pressure, timing, and isotopic composition of this fluid event, and delineate where this fluid was focused.
- (3) The exact nature of the precipitation mechanism should be studied further. If gold precipitation is due to interactions with pyrite, then other phases that would behave in a similar fashion should also be the focus of exploration. Comparable exploration targets would include any Fe-rich material, i.e. areas that contain mafic host rock and iron formations, or geological units that contain high concentrations of Ti-Fe oxides.

REFERENCES

- Ansdell, K.M., and Kyser, T.K., 1992, Proterozoic mesothermal gold mineralization in a Proterozoic greenstone belt; Western Flin Flon Domain, Saskatchewan, Canada. *Economic Geology*, Vol. 87, p. 1496-1525.
- Ansdell, K.M., 1992, Evolution of the Western Flin Flon Domain with special reference to epigenetic gold mineralization. unpublished Ph.D thesis, Geological Science Department, University of Saskatchewan, Canada, 306p.
- Ansdell, K.M., and Kyser, T.K., 1990, Age of granitoids from the western Flin Flon Domain: an application of the single-zircon Pb-evaporation technique. *in* Summary of Investigations 1990, Saskatchewan Geological Survey; Saskatchewan Energy and Mines, Miscellaneous Report 90-4, p. 138-142.
- Bellevantsev, V.I., Peshchevskii B.I., and Shamovskaya, G.I., 1981, Gold(I) complexes in aqueous solutions. *Isvest. Sib. Otd. Akad. Nauk SSSR, Ser. Khim.* 1, p. 81-87.
- Bell, K., and Macdonald, R. 1982. Geochronological calibration of the Precambrian Shield in Saskatchewan. *in* Summary of Investigations 1982. Saskatchewan Geological Survey, Miscellaneous Report 84-4, p. 17-22.
- Bickford, M.E., Collerson, K.D., Lewry, J.F., Van Schmus, W.R. and Chiarenzelli, J.R., 1990, Proterozoic collisional tectonism in the Trans-Hudson Orogen, Saskatchewan. *Geology*, v.18, p. 14-18.
- Bigeleisen, J., Pearlman, M.L., and Prosser, H.C., 1952, Conversion of hydrogenic material to hydrogen for isotope analysis. *Analytical Chemistry*, v. 24, p. 1356-1357.
- Brown, P.E., and Lamb, W.M., 1986, Mixing of H₂O-CO₂ in fluid inclusions: geobarometry and Archean gold deposits. *Geochimica et Cosmochimica Acta*, v. 50, p. 847-852.
- Brown, P.E., and Lamb, W.M., 1989, P-V-T properties of fluid in the system H₂O+CO₂+NaCl: new graphical presentation and implications for fluid inclusion studies. *Geochimica et Cosmochimica Acta*, v. 27, p. 43-52.
- Bottinga, Y., and Javoy, M., 1973, Comments on oxygen isotope geothermometry. *Earth Planet. Sci. Lett.*, v. 20, p. 250-265

- Bowers, T.S., 1991, The deposition of gold and other metals: pressure-induced fluid immiscibility and associated stable isotope signatures. *Geochimica et Cosmochimica Acta*, v. 55, p. 2417-2434.
- Burrows, D.R., Wood, P.C., and Spooner, E.T.C., 1986, Carbon isotope evidence for a magmatic origin for Archean gold quartz vein deposits. *Nature*, v. 321, p. 851-854.
- Cambell, S.W., 1986, Petrographic Study of Samples from Seabee. Placer Development Limited, internal report.
- Cameron, E.M., and Hattori, K., 1987, Archean gold mineralization and oxidized hydrothermal fluids. *Econ. Geol.*, v. 82, p. 1177-1191.
- Chiarenzelli, J.R., Lewry, J.F., and Landon, M., 1987, Bedrock geology, Iskatikan Lake area: evidence for Hudsonian juxtaposition of Proterozoic and Archean rocks along a ductile detachment surface. Saskatchewan Geological Survey, Miscellaneous Report 87-4, p.46-51
- Chiarenzelli, J.R., 1989, The Nistowiak and Guncoat Gneises: implications for tectonics of the Glennie and La Ronge Domains, northern Saskatchewan, Canada. unpubl. Ph.D. Thesis, Univ. Kansas, 229p.
- Collins, L.F., 1979, Gas hydrates in CO₂- Bearing fluid Inclusions and the use of freezing data for estimation of Salinity. *Economic Geology*, Vol. 74, p. 1435-1449.
- Colvine, A.C., 1988, An empirical model for the formation of Archean gold deposits: products of final cratonization of the Superior Province Canada. *in* Keays R.R Ramsay W.R.H and Groves D.I (eds), *The Geology of Gold Deposits: The Perspective in 1988: Economic Geology Monograph 6*, p. 37-53.
- Clayton, R.N., and Mayeda, T.K., 1963, The use of brominepentafluoride in the extraction of oxygen from oxides and silicates for isotopic analyses. *Geochimica et Cosmochimica Acta*, v.27, p. 4352
- Clayton, R.N., O'Neil, J.R., and Mayeda, T.K., 1972, Oxygen isotope exchange between quartz and water. *J. Geophys. Res.* 77, p. 3057-3067.
- Craig, L., 1989, Geology of the Pelican Narrows area. Unpub. thesis, Univ. Saskatchewan, 268p.

- Crawford, M.L., 1981, Fluid inclusions in metamorphic rocks - low and medium grade. in Hollister, L.S., and Crawford, M.L. (eds)., Fluid inclusions, applications to petrology: Min. Assoc. Can. Short Course, v.6, p. 157-181
- Delaney, G.D., 1986, Bedrock geological mapping, Laonil Lake area. in Summary of Investigations 1986, Saskatchewan Geological Survey, Sask. Energy & Mines, Misc. Rep. 86-4, p. 32-41.
- Delaney, G.D., 1992, Gold in the Glennie Domain. Saskatchewan Energy and Mines, Misc. Rep. 93-5, 71p.
- Delaney, G.D., and Cuttler, S.A., 1992, Geological setting of the 'Santoy Lake' gold camp (part of NTS 63M-11 and -12). in Summary of Investigations 1992, Saskatchewan Geological Survey, Sask. Energy and Mines, Misc. Rep. 92-4, p. 30-40.
- Durocher, K.E, Cutler, S., Delaney, G.D and Kyser, T.K., 1992, Gold Occurrences in the Santoy Lake Area, Glennie Domain, Trans-Hudson Orogen. in Summary of Investigations 1992, Saskatchewan Geological Survey, Sask. Energy Mines, Misc. Rep. 92-4, p. 41-50
- Durocher, K.E, Kyser, T.K., and Delaney, G.D., 1993, The pressure-temperature-time history of the Santoy Lake Area, Glennie Domain, Trans-Hudson Orogen: Preliminary petrogenetic, geothermometric results and $^{207}\text{Pb}/^{206}\text{Pb}$ zircon ages. in Summary of Investigations 1993, Saskatchewan Geological Survey, Sask. Energy Mines, Misc. Rep. 93-4, p. 67-103.
- Faure, G., 1986, Principles of Isotope Geology. John Wiley and Sons, p. 115-140.
- Fayek, M., Kyser, T.K., Kusmirski, R.T., Sopuck, V., and Chan, D., 1993, Contrasting styles of alteration with barren and auriferous quartz veins from Contact Lake lode gold deposit. in Summary of Investigations 1993, Saskatchewan Geological Survey, Sask. Energy Mines, Misc. Rep. 93-4, p. 153-160.
- Fedorowich, J., Stauffer, M., and Kerrich, R., 1991, Structural setting and fluid characteristics of the Proterozoic Tartan Lake gold deposit, Trans-Hudson Orogen, northern Manitoba. Economic Geology, v.86, p. 1434-1467.

- Groves, D.I., Barley, M.E., And Ho, S.E., 1988, Nature, genesis and tectonic setting of mesothermal gold mineralization in the Yilgarn Block, Western Australia. in Keays, R.R., Ramsay W.R.H. and Groves D.I. (eds), Economic Geology Monograph 6, The Geology of Gold Deposits: The Perspective in 1988, p. 71-85.
- Gummer, P.K., 1986, Geology of the Seabee Gold Deposit, Tabernor Lake Belt, Saskatchewan. in Gold in the Western Shield, Loyd A. Clark (ed.), The Canadian Institute of Mining and Metallurgy, Sp. Vol. 28, p. 272-284.
- Hanes, J.A., 1991, K-Ar and $^{40}\text{Ar}/^{39}\text{Ar}$ Geochronology: Methods and Applications. in Mineralogical Association of Canada Short Course on Radiogenic Isotope Systems, v. 19, p.27-57.
- Hayashi, K.I., and Ohmoto, H., 1991, Solubility of gold in NaCl- and H₂S- bearing aqueous solutions at 250-350. *Geochimica et Cosmochimica Acta*, V. 55, p. 2111-2126.
- Helmstaedt, H., 1986, Report on the geology and structure of the Seabee and Currie Rose Properties, Laonil Lake Saskatchewan. Placer Developments Limited, internal report, 14p.
- Helmstaedt, H., 1987, Report on geology of the No.2 Zone on the Seabee Property Laonil Lake, Saskatchewan. Placer Developments Limited, internal report, 13p.
- Hodgson, C.J., and Hamilton, J.V., 1988, Gold mineralization in the Abitibi Greenstone Belt: end-stage result of Archean collisional tectonism?. in Keays R.R Ramsay W.R.H and Groves D.I (eds.), The Geology of Gold Deposits: The Perspective in 1988: Economic Geology Monograph 6, p. 37-53.
- Hoffman, P.F., 1981, Autopsy of the Athapuscow Aulacogen: a failed arm affected by three collisions. in Campbell, F.H.A (ed.), Proterozoic Basins of Canada: Geological Survey of Canada, Paper 81-10. p. 97-101.
- Hoffman, P.F., 1990, Subdivision of the Churchill Province and extent of the Trans-Hudson Orogen. in Lewry, J.F., and Stauffer (eds.), The Early Proterozoic Trans-Hudson Orogen of North America. Geol. Assoc. Can., Special Paper 37, p.15-39.
- Hoefs, J., 1987, Stable isotope geochemistry, 3rd ed. New York, Springer-Verlag, 241p.

- Hrdy, F., 1994, The Jasper Lode gold deposit. unpublished M.Sc., Geological Science Department, University of Saskatchewan, Canada, 120p.
- Hutchinson, R.W., and Burlington, J.L., 1984, Some broad characteristics of greenstone belt lodes. *in* Gold '82: The geology, geochemistry and genesis of gold deposits, R.P. Foster (ed.), Balkema, Rotterdam, p. 339-372.
- Ibrahim, M.S., and Kyser, K., 1991, Fluid inclusion and stable isotope systematics of the high-temperature Proterozoic Star Lake Deposit, Northern Saskatchewan, Canada. *Economic Geology*, v. 86, p. 1468-1490.
- Jenner, G.A., Longerich, H.P., Jackson, S.E., and Fryer, B.J., 1990, ICP-MS: A powerful tool for high-precision trace-element analysis in earth sciences: evidence from analysis of selected U.S.G.S. reference samples. *Chem. Geol.*, v. 83, p. 133-148.
- Kajiwara, Y. and Krouse, H.R., 1971, Sulfur isotope partitioning in metallic sulfide systems. *Can. J. Earth Sci.* V. 8, p. 1397-1408.
- Kerrich, R., 1987, Stable isotope geochemistry of Au-Ag vein deposits in metamorphic rocks. *in* Kyser T.K. (ed.), Mineralogical Association of Canada, Short Course Notes, v. 6, p. 129-198.
- Kerrich, R., 1989a, Geochemical evidence on the sources of fluids and solutes for shear zone hosted mesothermal Au deposits. *in* Bursnal J.T (ed.), Mineralization and Shear Zones, Geological Association of Canada, short course notes, v. 6, p. 89-128.
- Kerrich, R., 1989b, Geodynamic setting and hydraulic regimes: shear zone hosted mesothermal gold deposits. *in* Bursnal J.T (ed.), Mineralization and Shear Zones, Geological Association of Canada, short course notes, v. 6, p. 89-128.
- Kerrich, R., and Allison I., 1978, Flow mechanisms in rocks, *Geoscience Canada*. v. 5-3, p. 109-118.
- Kerrich, R., and Fyfe, W.S., 1981, The gold-carbonate association: source of CO₂ and CO₂-fixation reaction in Archean lode gold deposits. *Chem Geol.*, v. 33, p. 265-294.
- Kerrich, R., and Kamineni, D.C., 1988, Characteristic chronology of fracture-fluid infiltration in the Archean, Eye Dashwa Lake Pluton, Superior Province: evidence from H, C, O - isotope and fluid inclusions. *Contributions to Mineralogy and Petrology*, v. 99, p. 430-445.

- Kober, B., 1986, Whole-grain evaporation for $^{207}\text{Pb}/^{206}\text{Pb}$ age investigations on single zircons using a double-filament thermal ion source. *Contrib. Mineral. Petro.*, v. 93, p. 482-490.
- Kober, B., 1987, Single-grain evaporation combined with Pb^+ emitter bedding for $^{207}\text{Pb}/^{206}\text{Pb}$ investigations on single zircons using thermal ion mass spectrometry, and a double-filament thermal source. *Contrib. Mineral. Petro.*, v. 96, p. 63-71.
- Kotzer T.G., Kyser, K., King, R.W., Kerrich, R., 1994, An empirical oxygen- and hydrogen- isotope geothermometer for quartz-tourmaline and tourmaline-water. *Geochimica et Cosmochimica Acta*, v. 57, p. 3421-3426.
- KRTA Inc., 1986, Fluid Inclusion Study of nine quartz samples from Seabee Gold Property, Saskatchewan. Placer Development Limited, internal report, 27p.
- Kyser, T.K., 1986, Stable isotope variations in the mantle. *in* *Stable Isotopes in High Temperature Geological Processes*, Valley, J.W., Taylor, H.P., Jr. and O'Neil, J.R. (eds.), *Mineral. Soc. Am., Rev. Mineral.*, v. 16, Bookcrafters Inc., Michigan, p. 141-184.
- Kyser, T.K., Fayek, M., and Sibbald, T.I.I., 1992, Geochronologic Studies in the La Ronge and Glennie Domains. *in* *Summary of Investigations 1992*, Saskatchewan Geological Survey, Sask. Energy Mines, Misc. Rep. 92-4, p. 130-133.
- Kyser, T.K., Janser, B.W., Wilson, M.R., and Hattie, I., 1986, Stable isotope geochemistry related to gold mineralization and exploration in the western shield. *in* Clark, L.A. (ed.), *Gold in the western shield*, CIM Special Vol. 38, p. 470-498.
- Kyser, K., and Kerrich, 1991, Retrograde exchange of hydrogen isotopes between hydrous minerals and water at low temperatures. *in* *Stable Isotope Geochemistry: A Tribute to Samuel Epstein*, H.P. Taylor, J.R. O'Neil and I.R. Kaplan (eds.) Special Publication No. 3, The Geochemical Society, p. 409-422.
- Kyser, T.K., and O'Neil, J.R., 1984, Hydrogen isotope systematics of submarine basalts. *Geochimica et Cosmochimica Acta*, v.48, p. 2123-2133.
- Lewry, J.F., 1977, The geology of the Glennie Lake area. Sask. Dep. Miner. Resour., Rep.143, 59p.

- Lewry, J.F., and Sibbald, T., 1977, Variation in lithological and tectonometamorphic relationships in the Precambrian basement of northern Saskatchewan. *Can. J. Earth Sciences.*, v. 14, p. 1453-1467.
- Lewry, J.F., Collerson, K.D., 1990, The Trans-Hudson Orogen: extent, subdivision, and problems. *in* Lewry, J.F. and Stauffer, M.R., (eds.), *The Early Proterozoic Trans-Hudson Orogen of North America*. Geol. Assoc. Cam., Spec. Pap. 37. p. 1-15.
- Lewry, J.F., Thomas, D.J., Macdonald, R., and Chiarenzelli, J., 1990, Structural relations in accreted terranes of the Trans-Hudson Orogen, Saskatchewan: Telescoping in a collisional regime?. *in* Lewry, J.F. and Stauffer, M.R., (eds.), *The Early Proterozoic Trans-Hudson Orogen of North America*. Geol. Assoc. Cam., Spec. Pap. 37. p. 147-166.
- Lister, G.S. and Snoke, A.W., 1984, S-C Mylonites. *Journal of Structural Geology*. v.6, No.6, p. 617-638.
- Matthews, A., Goldsmith, J.R. and Clayton, R.N., 1983, Oxygen isotope fractionation involving pyroxenes: the calibration of mineral pairs geothermometers. *Geochim. Cosmochim. Acta* 50, p. 1667-1678.
- McLeod, J.A., 1983, Seabee Petrographic Study (Job V82:697R). Cominco Limited, internal report.
- McNicoll, V.J., Delaney, G.D., Parrish, R.R., and Heaman, L.H., 1992, U-Pb sphene and zircon ages from the Glennie Domain, Trans-Hudson Orogen, Saskatchewan. *in* Radiogenic Age and isotopic Studies, Rep.6, Geol. Surv. Can., Pap. 92-2, p. 57-72.
- Mikucki, E.J., and Groves, D.I., 1990, Constraints on genesis of primary gold deposits: Mineralogical constraints. *in* Ho S.E., Groves D.I., Bennett J.M. (eds.), *Gold Deposits of the Archean Yilgarn Block, Western Australia: Nature, Genesis and Exploration Guides*. Geol. Department and University Extension, The University of Western Australia, Publications 20, p. 212-220.
- The Northern Miner, 1985, Placer joins Claude Resources on the La Ronge gold belt. Sept. 9, p.19.
- The Northern Miner, 1987, Major underground effort set by Placer for Seabee. Jan. 26, p. 1.

- Ohomoto, H., and Rye, R.O., 1979, Isotopes of sulfur and carbon. in Barnes H.L. (ed.), Geochemistry of Hydrothermal ore deposits: New York, Wiley Intersci., p. 509-567.
- O'Neil, J.R., Clayton, R.N., and Mayeda, T.K., 1969, Oxygen isotope fractionation in divalent metal carbonates. *Journal of Chemistry, and Physics*, v. 51, p. 5547-5558.
- Potts, P.J., 1987, *A Handbook of Silicate rock analysis*. Blackie & Son Limited, Glasgow/London, p. 47-48.
- Rafter, T.A., 1965, Recent sulfur isotope measurements on a variety of specimens examined in New Zealand. *Bull. of Volcanol.*, v.28, p. 3-20.
- Rees, C.J., 1982, Metamorphism in the Canadian Shield of northern Saskatchewan. *Sask. Miner. Resour.*, Open File Rep. 82-2, 136p.
- Renders, P.J., and Seward, T.M., 1989, The stability of hydrosuphido- and sulphido-complexes of Au(I) and Ag(I) at 25 °C. *Geochim. Cosmochim. Acta*, v.53, p. 245-253.
- Rock, N.M.S., and Groves. D.I., 1988, Can lamprophyres resolve the genetic controversy over mesothermal gold deposits ?. *Geology*, v. 16, p. 538-541.
- Roedder, E., 1979, Fluid inclusions as samples of ore fluids. in Baren's H.L (ed.), Geochemistry of hydrothermal ore deposits, Wiley, New York, second ed., v. 12, p. 684-737.
- Roedder, E., 1984, Fluid inclusions. *Min. Soc. Amer.*, *Reviews in Mineral.*, v. 12, p. 646.
- Rye, D.M., and Rye, R.O., 1974 Homestake gold mine, South Dakota: I. Stable isotope studies. *Econ. Geol.*, v. 69, p. 293-317
- Schultz, D.j, 1990, Reconnaissance geological study of the Seabee gold deposit, Glennie Domain. in Summary of investigations 1990, Saskatchewan Geological Survey, Saskatchewan Energy and Mines, Miscellaneous Report 90-4, p. 70-73.
- Schultz, D.j. and Kerrich, R., 1991, Structural controls and geochemical character of the Seabee Gold Mine, Laonil Lake, Glennie Domain. in Summary of Investigations 1991, Saskatchewan Geological Survey, Sask. Energy Mines, Misc. Rep. 91-4, p. 101-108.

- Seward, T.M., 1984, The transportation and deposition of gold in hydrothermal systems. in Gold '82: The Geology, Geochemistry, and Genesis of Gold Deposits (ed. R.P. Foster), p. 165-181.
- Shenberger, D.M., and Barnes, H.L., 1989, Solubility of gold in aqueous sulfide solutions from 150 to 350 °C. *Geochimica et Cosmochimica Acta*, v. 53, p. 269-278.
- Shepherd, T.T., 1985, A practical guide to fluid inclusions studies. Blakie, Glasgow, 239p.
- Stauffer, M.R., 1984, Manikewan: an early Proterozoic ocean in central Canada, its igneous history and orogenic closure. *Precambrian Res.*, v.25, p. 257-281.
- Taylor, H.P. Jr, and Sheppard, S.M.F., 1987, Igneous rocks: I. Processes of isotopic fractionation and isotope systematics. in Valley, J.W., Taylor, H.P. Jr. and O'Neil, J.R., (eds.), Stable isotope in high temperature geological processes. *Mineral. Soc. Amer. Reviews in Mineral.*, v.16, p. 227-272.
- Thomas, D.J., 1993, Geology of the Star-Otter Lake portion of the Central Metavolcanic Belt, La Ronge Domain. *Sask. Energy Mines, Rep.* 236, p. 1-132.
- Van Schums, W.R., Bickford, M.E., Lewry, J.F., and Macdonald, R., 1987, U-Pb zircon geochronology in the Trans-Hudson Orogen, Northern Saskatchewan, Canada, *Can. J. Earth Sci.*, v.24, p. 407-424.
- White, D.J, Lucas, S.B, Hajnal, Z., Green, A.G., Lewry, J.F., Weber, W., Bailes, A.H, Syme, E.C., Ashton, K., 1994, Paleo-Proterozoic thick skinned tectonics; Lithoprobe seismic reflection results from the eastern Trans-Hudson Orogen. *Can. J. of Earth Sci.*, v.31, p.458-469.
- Wyman, D., and Kerrich, R., 1988, Alkaline magmatism, major structures, and gold deposits: Implications for greenstone belt gold metallogeny. *Econ. Geol.*, v.83, p. 454-461.

Appendix A: List of samples and locations

List of Samples and Locations

Sample#	Description	Zone	Location		Analysis
S109	Ore Sample	2	DDH S109	664.5'	Probe
Z2#8a	Qtz-tourm vein	2	Surface		Probe
Z5-15	MetaSediment	5	Surface		WR
Z2-Porph	Qtz-Porphyry	2	Surface		WR
Z2-12	Mafic Dyke	2	Surface		WR
GD-CB	Mafic Dyke	2	Surface		WR
Z2-14	Porphyry	2	Surface		WR
PORPHZII	Porphyry	2	Surface		WR
Z210	Diorite	2	Surface		WR
D1-CB	Qtz Diorite	2	Surface		WR
14ZMS	Metasediment	5	Surface		WR
Z51	Metasediment	5	Surface		WR,Ar/Ar
BSLT-CB	Basalt	EB	Surface		WR
Z514	Mylonite	5	Surface		WR
RD-CB	Intermediate Dyke	2	Surface		WR
UM-CB	Ultramafic		Surface		WR
6BCB	Gabbro	2	Surface		WR
cb2(R)	Gabbro	2	1175N	950E	WR
cb6	Gabbro	2	1165N	950E	WR,Ar/Ar
cb7	Gabbro	2	1110N	1000E	WR
cb4	Gabbro	2	1015N	960E	WR
cb3(R)	Gabbro	2	1145N	990E	WR
cb5	Gabbro	2	1175N	990E	WR
cb1	Gabbro	2	1125N	1000E	WR
cb2	Gabbro	2	1175N	950E	WR
cb3	Gabbro	2	1145E	990E	WR
S120-1	Mylonite	2	DDH S-120	45.49m	WR
S120-17(R of S120-1)	Mylonite	2	DDH S-120	45.49m	WR
S120-2	Mylonite	2	DDH S-120	45.98m	WR
S120-3	Mylonite	2	DDH S-120	47.07m	WR
S120-4	Mylonite	2	DDH S-120	48.02m	WR
S120-18(R of S120-4)	Mylonite	2	DDH S-120	48.02m	WR
S120-5	Mylonite	2	DDH S-120	49.39m	WR
S120-6	Mylonite	2	DDH S-120	50.09m	WR
S120-7	Mylonite	2	DDH S-120	51.52m	WR
S120-8	Mylonite	2	DDH S-120	52.50m	WR
S120-9	Mylonite	2	DDH S-120	53.51m	WR
S120-10	Mylonite	2	DDH S-120	54.12m	WR
S120-11	Mylonite	2	DDH S-120	54.19m	WR
S120-12	Mylonite	2	DDH S-120	54.42m	WR
S120-19(R of S120-12)	Mylonite	2	DDH S-120	54.42m	WR
S120-13	Mylonite	2	DDH S-120	55.37m	WR
S120-14	Mylonite	2	DDH S-120	56.77m	WR
S120-15	Mylonite	2	DDH S-120	57.32m	WR
S120-20(R of S120-15)	Mylonite	2	DDH S-120	57.32m	WR
S120-16	Mylonite	2	DDH S-120	58.23m	WR
2b-100stp	Carbonate	2	2b-100 stope		ICP
2b-100stp	Chalcopyrite	2	2b-100 stope		ICP
2b-100stp	Pyrite	2	2b-100 stope		ICP
2b-100stp	Pyrrhotite	2	2b-100 stope		ICP
Z2-7	Qtz-tourm vein	2	Surface		FI
S-133	Qtz-tourm vein	2	DDH S-133	281.0m	FI
Z5-4	Qtz-tourm vein	5	Surface		FI
2B Ore Zone	Qtz-tourm vein	2	DDH S-223	219.6m	SI
2H Ore Zone	Qtz-tourm vein	2	DDH S-236	321.5m	SI
2C Barren	Qtz-tourm vein	2	DDH S-236	521.8m	SI
2H Barren	Qtz-tourm vein	2	DDH S-236	539.6m	SI
2B Barren	Qtz-tourm vein	2	DDH S-236	543.9m	SI

Sample#	Description	Zone	Location	Analysis
2H Dp#4	Carbonate vein	2	H-vein	SI
100stp	Qtz-tourm vein	2	2b100 stope	SI,Sr,ICP
325stp	Carbonate vein	2	2b325 stope	SI
Z2-1,2	Qtz-tourm vein	2	Surface	SI,Sr
Z2-9	Qtz-tourm vein	2	Surface	SI
S-133 281.0	Qtz-tourm vein	2	DDH S-133 281.0m	SI
S-133 268.4	Qtz-tourm vein	2	DDH S-133 268.4m	SI
S-124 243.5	Qtz-tourm vein	2	DDH S-124 243.5m	SI
S-126 299.5	Qtz-tourm vein	2	DDH S-126 299.5m	SI
S-126 293.5	Qtz-tourm vein	2	DDH S-126 293.5m	SI,Sr
S-128 120.1	Qtz-tourm vein	2	DDH S-128 120.1	SI
S-128 50	Qtz-tourm vein	2	DDH S-128 50.0m	Ar/Ar
Z5-2	Qtz-tourm vein	5	Surface	SI
S-237 28.7	Qtz-tourm vein	2	DDH S-237 28.7m	SI
Z10-1	Qtz-tourm vein	10	Surface	SI
S-231 158.7	Qtz-tourm vein	2	DDH S-231 158.7m	SI
S-215 65	Qtz-tourm vein	5	DDH S-215 65.0m	SI
S-196 98.3	Qtz-tourm vein	2	DDH S-196 98.3m	SI
S-196 44.0	Qtz-tourm vein	EB	DDH S-196 44.0m	SI
S-196 102.4	Qtz-tourm vein	EB	DDH S-196 102.4m	SI
H-36	Qtz-tourm vein	2	DDH H-36	Sr
Cpy-4	Chalcopyrite	2	2b100 stope	Sr
Au8	Gold	2	2b100 stope	Sr
Z161-B	Qtz-tour vein	161	DDH S-161 170m	SI

Note: WR=whole rock XRF; ICP=ICP-MS analysis; SI=stable isotope analysis; FI=Fluid inclusions thermometry; Sr=radiogenic Sr analysis; Ar/Ar=radiogenic argon analysis; EB=East Boundary Zone; 2=Zone 2; 5= Zone 5; (R) Repeat analysis; DDH=diamond drill hole

Appendix B: Fluid inclusion data from KRTA inc

Table1 (Data from Appendix A of KRTA ltd., 1986)

<u>Sample No.</u>	<u>Th °C</u>	<u>Tm °C</u>
S123 221.1	150, 150, 180, 220, 230 250, 260, 280, 340	
S133 263.3	190, 210, 255, 260, 270 285	-7.0
S133 267.35	210, 210, 210, 210	
S133 268.8	190, 220, 230, 230, 240	-52.7*, -52.7* -54.8*, -55.8*
S133 272.4	24-26*, 210, 210, 210 255	-54.9*, -56.0*
S143 178.15	20-30*, 230, 230, 250, 255	-54.9*, -56.0*
S143 180.1	110, 150, 150, 250, 280	-54.9*
S161 73.6	27*, 150, 160, 170, 180, 210, 280	-55.2*, -7.7, -6.5, -6.6, -6.5
S161 76.4	130, 190, 220, 240	-54.3*, -55.1*

* Type Ia (CO₂ inclusions), all other inclusions are Type Ib

Appendix C: Analytical procedures

Fieldwork: Fieldwork was carried out over two four week periods within the 1990 and 1991 field seasons. During these times numerous outcrops were sampled. Underground exposures allowed sampling of ore material that contained significant mineralization. Samples from drill-core (S-120) were collected every few metres (corrected for horizontal distance) through a mineralized structure (45.49 to 58.28 metres) to test the extent of alteration and for protolith discrimination studies. Repeat analyses of selected samples were conducted for various technique to verify analytical reproducibility.

Petrography: Polished thin sections were cut from host rocks and quartz vein sample, and were prepared "in house" using the standard cutting and polishing techniques as described by Potts, (1987).

Petrographic examination was done by making textural observations on polished thin sections from quartz veins, thereby identifying samples having inclusions suitable for microthermometric analysis. After identifying suitable samples, doubly polished quartz wafers of 70 to 150 μ in thickness were prepared.

The quartz wafers were inspected using the petrographic microscope for identification of fluid inclusions suitable for measurement. Areas containing the appropriate inclusions were marked and broken into 5-to-10mm sized chips such that the samples could fit into the sample chamber of the heating-cooling stage.

Fluid inclusions: Microthermometric data were obtained using a Fluid Inc.-adapted U.S. Geological Survey-type gas-flow freezing-heating stage which was calibrated to have low temperature error of $\pm 0.1^\circ\text{C}$, high temperature error of $\pm 0.4^\circ\text{C}$, and $\pm 1.0^\circ\text{C}$ maximum error for other measurements. Microthermometric measurements were obtained from fluid inclusions on: (1) the final melting temperature of the CO_2 (T_{mCO_2}), from which the CO_2 purity can be determined; (2) the initial melting temperature of ice (T_{e}), where an estimation of the type of salt present can be made; (3) the temperature of final ice melting ($T_{\text{m}_{\text{ice}}}$), from which fluid salinities can be estimated; (4) the temperature at which the clathrate disappears ($T_{\text{m}_{\text{clath}}}$); also a measure of the salinity, and (5) the temperature of bulk homogenization of the inclusion (T_{h}), from which the minimum fluid trapping temperature is derived. Thermometric data were collected on inclusions that demonstrated no petrographic evidence of necking.

Mineral separates: Samples were categorised petrographically prior to obtaining mineral separates. This ensured that minerals selected for isotopic analysis were constrained in

terms of textural equilibrium. Minerals were separated by crushing samples of ore, or host rock, and wet sieving hand-sized volumes of the sample. Hand picking was done on samples which contained larger grain sizes. Many samples required the use of heavy liquids, and a Frantz electromagnetic separator to concentrate larger quantities desired phases. Chalcopyrite, microfracture quartz, pyrrhotite, pyrite, and carbonate were drilled out from hand samples with a dental drill.

Stable isotopes: Oxygen was obtained from silicates using the BrF_3 extraction method of Clayton and Mayeda (1963). Hydrogen was extracted using the uranium technique of Bigeleisen et al., (1952) as modified by Kyser and O'Neil (1984). Sulphur was liberated from sulphide minerals by oxidizing with CuO (Rafter, 1965).

Isotopic data are reported as δ -values in units of per mil relative to a standard. Both oxygen and hydrogen isotope values are reported relative to Vienna Standard Mean Ocean Water (VSMOW), sulphur isotopes to the Canyon Diablo troilite (CDT), and carbon isotopes to Pee Dee Belemnite (PDB). Isotopic ratio measurements were made with a Finnigan-Mat 251 and a VG 602C isotope ratio mass spectrometers. Reproducibilities (2 sigma) of δ values in per mil are ± 0.2 for oxygen, ± 3 for hydrogen, and ± 0.3 for sulphur.

Radiogenic lead ($^{207}\text{Pb}/^{206}\text{Pb}$) evaporation: Individual zircons were wrapped in Re filaments and mounted in a Finnigan Mat 261 mass spectrometer. Carousel preparation and zircon mounting is described by Ansdell (1992). Pb is measured in single-collector mode using a secondary electron multiplier (SEM). Dilute 982 Pb standard is used to centre each Pb mass in the SEM, and two blocks are acquired at 1200°C to constrain mass fractionations. Zircons are cleaned by elevating the evaporation filament to 1.8 A (1200°C) for 10-15 minutes. This step removes low temperature Pb from the surface, cracks and metamorphic zones. Then the ionization filament is cleaned by heating to high temperature (2220°C), and is done after each analysis. This prevents Pb contamination between evaporation steps. In the initial step, Pb is transferred from the evaporation filament to the cool ionization filament at 2.2 A (1450°C). After Pb transfer, the evaporation filament is reduced to 1.2 A, and the acquisition sequence is started. Following the acquisition and prior to the next Pb transfer step, the ionization filament is cleaned by elevating the current to 3.5 A. In subsequent evaporation steps the evaporation filament current is increased at 0.5 A (a temperature increase of 25 to 50°C) increments. Transfer and acquisition steps continue until no Pb remains in the zircon.

Radiogenic strontium: Chalcopyrite, pyrrhotite, and tourmaline separates were prepared for Rb-Sr isotope measurement through

standard dissolution procedures in teflon vials, and Rb and Sr were separated by conventional cation-exchange techniques (Potts, 1987). Samples were spiked with the appropriate amounts for ^{84}Sr and ^{87}Rb . Isotope ratio analyses were performed on a Finnigan MAT 261 solid source mass spectrometer. The mass spectrometer, in isotopic ratio mode at high resolution, was optimized and calibrated on Rb and Sr, using blanks (0.2N HNO_3 acid) and standards (NBS987 for Sr, NBS984 for Rb) to correct for background levels of Rb and Sr and instrumental drift.

Radiogenic argon: $^{40}\text{Ar}/^{39}\text{Ar}$ isotopic analyses were performed on biotite and amphiboles from auriferous vein and host rock mineral separates at Queens University by J. Fedorowich using irradiation, extraction, mass spectroscopic and correction procedures described by Hanes(1991).

Microprobe: Microprobe analysis were determined by wavelength-dispersive electron microscopy using a fully automated JEOL JXA-8600 X-ray microanalyzer. The accelerating voltage for silicates were 15Kv, whereas for sulphides, tellurides and gold 20Kv was applied. Standards used for silicate analysis were Si, Mn, Ca (bustamite), Ti (benitoite), Al, Fe (almandine), Mg (olivine), Na (jadeite), F (fluorite), and standards used for sulphides, telluride and gold analysis were Zn, S (sphalerite), Mn (bustamite), Cu (cuprite), Fe, Ni (pentlandite), As, Co (cobaltite), Sb (stibnite), Ag (iodyrite), Bi (synthetic BiSe) Au, $\text{Ag}(\text{Au}_{68}\text{Ag}_{32})$, Hg, Te (Pb_3HgTe_3 -Cabri-451), Pb, S (galena). The data were corrected and reduced using ZAF and Phi-Rho-Z correction programs provided by Noram Instruments, for silicates and sulphides respectively. Major element oxide wt% are generally precise to $\pm 1\%$ of the total, and minor elements are precise to about 10%. Textural information was derived by backscatter and secondary electron imagery.

Major and trace element analysis: Whole-rock samples were sent to X-ray Assay Laboratories, Don Mills, Ontario for XRF analysis. The samples were crushed and milled in an agate mortar prior to being fused with lithium tetraborate. Major and trace elements (Cr, Rb, Sr, Y, Zr, Nb, Ba) were determined using a Phillips PW1600 simultaneous X-ray fluorescence spectrometer with detection limits for major elements of ± 0.01 wt%, and ± 10 ppm for trace elements. Replicate analyses of the same powders indicate that precision is variable, ranging from about 1% for major elements to 20% for traces elements, and is a function of element concentration, sample heterogeneity, and analytical error.

Trace element and rare earth element concentrations of whole-rock samples were measured on a Perkin Elmer Sciex Elan 5000 ICP-MS, operating at a power setting of 1000 watts, nebulizer

flow rate of 0.08 L/min, B, P, E1, and S2 lens settings of 45, 45, 25, and 38 respectively, and argon supply of 55 psi. A total counting time per mass of 10s with a dwell time per mass of 0.05s were used. The calibration strategy employed was that of Jenner et al., (1990), wherein pure elemental standards (supplied by Inorganic Ventures Inc.) were used for external calibration. The following is a list of elements analyzed and their corresponding detection limits (detection limits in ppm): Be(1.2), Rb(0.36), Sr(0.28), Ba(0.07), Cs(0.02), Ta(0.01), Th(0.02), U(0.01), Zr(0.02), Hf(0.03), Nb(0.01), Y(0.02), Sc(1.5), V(0.08), La(0.04), Ce(0.03), Pr (0.03), Nd (0.03), Sm(0.03), Eu(0.01), Gd(0.03), Tb(0.01), Dy(0.02), Ho(0.01), Er(0.01), Tm(0.01), Yb(0.02), and Lu (0.01).

Appendix D: Summary of microprobe data

Sulphide Mineral Analyses**Zone 2 S109 644.5 Auriferous Quartz Vein**

Mineral	Po	Cpy	Py	Cpy	Py	Py	Po	Py	Bite	BiTe	Au
S	54.0	35.2	39.0	35.0	39.2	37.4	53.8	37.3	0.07	0.04	0.07
Fe	46.6	30.0	60.3	30.1	60.3	62.3	47.9	58.3	0.16	0.30	0.56
Ni	0.05	0.01	0.11	0.02	0.11	.04	0.02	0.10	0.04	0.01	0.01
Cu	0.01	34.0	0.01	34.2	0.02	0.01	0.01	0.01	0.01	0.01	0.03
Zn	0.06	0.01	0.01	0.01	0.04	0.05	0.01	0.02	0.04	0.04	0.02
As	0.01	0.01	0.01	0.01	0.01	0.01	0.01	0.01	0.02	0.01	0.01
Se	0.01	0.01	0.13	0.01	0.01	0.01	0.01	0.09	0.01	0.01	1.92
Ag	0.01	0.01	0.01	0.05	0.01	0.01	0.01	0.01	0.01	0.01	4.01
Sb	0.01	0.01	0.01	0.01	0.02	0.01	0.01	0.01	0.18	0.03	0.01
Te	0.02	0.02	0.07	0.03	0.04	0.01	0.01	0.01	47.9	48.1	0.03
Au	0.01	0.01	0.01	0.01	0.01	0.88	0.01	0.01	0.55	0.62	93.3
Pb	0.01	0.01	0.01	0.01	0.01	0.01	0.01	0.01	0.01	0.01	0.01
Bi	0.13	0.15	0.08	0.06	0.09	0.18	0.16	0.14	48.1	48.7	0.77
TOTAL	100.8	99.5	99.7	99.4	99.8	100.5	101.8	96.0	97.0	97.8	100.7

Cpy=Chalcopyrite; Py=Pyrite; Po=Pyrrhotite; Au=Native Gold; BiTe=Tellurobismuthite

Unaltered Tourmaline Analyses**Zone #2 Sample - #8 Quartz-tourmaline Vein**

Grain Point#	A #1	A #2	A #3	B #4	B #5	B #6	C #7	C #8	C #9	E #10	E #11
SiO ₂	35.46	35.75	35.07	35.33	35.10	34.98	35.45	35.41	35.32	35.69	34.69
TiO ₂	0.33	0.38	0.51	0.79	0.53	0.37	0.15	0.11	0.19	0.24	0.23
B ₂ O ₃	10.27	10.35	10.16	10.23	10.17	10.13	10.27	10.26	10.23	10.34	10.05
Al ₂ O ₃	30.00	29.93	29.79	29.70	28.23	29.13	28.55	30.36	29.05	29.14	28.29
FeO	8.83	8.92	9.44	8.94	9.37	8.89	9.04	9.14	9.29	9.35	9.19
MnO	0.00	0.03	0.03	0.02	0.03	0.00	0.05	0.00	0.01	0.00	0.00
MgO	7.17	7.44	6.45	6.75	7.90	7.06	7.30	6.72	7.48	7.27	7.16
CaO	0.45	1.02	0.39	0.77	1.08	0.48	0.33	0.18	0.29	0.28	0.30
Na ₂ O	2.24	1.95	2.19	2.04	2.22	2.23	2.40	2.12	2.42	2.37	2.28
K ₂ O	0.00	0.00	0.00	0.00	0.00	0.00	0.00	0.00	0.00	0.00	0.00
F	0.00	0.00	0.00	0.00	0.00	0.00	0.00	0.00	0.00	0.00	0.00
TOTAL	94.75	95.77	94.03	94.57	94.62	93.27	93.54	94.30	94.28	94.68	92.19

Reported data is in weight percent oxides for silicates and total elemental percent for sulphides

Appendix E: Summary of major and trace element whole rock data

Meta Gabbro (XRF)

Elements	UNITS	cb2(R) Gabbro	cb6 Gabbro	cb7 Gabbro	cb4 Gabbro	cb3(R) Gabbro	cb5 Gabbro	cb1 Gabbro	cb2 Gabbro	cb3 Gabbro
SiO2	wt %	50.2	49.3	50.5	50.1	49.1	49.7	50.5	49.9	49.8
TiO2	wt %	0.37	0.34	0.48	0.46	0.44	0.27	0.53	0.35	0.42
Al2O3	wt %	20	17.6	15.9	16.7	18.2	19.5	18.1	19.1	18.1
Fe2O3	wt %	6.09	7.29	8.64	8.63	7.92	6.07	8.34	6.5	7.39
MnO	wt %	0.1	0.13	0.14	0.13	0.13	0.1	0.13	0.11	0.12
MgO	wt %	5.99	8.15	7.66	7.41	7.22	7.83	8.17	6.95	7.04
CaO	wt %	12.8	12.4	11.8	11.3	12.8	12.5	11.6	12.1	12.7
K2O	wt %	0.62	0.58	0.41	0.57	0.31	0.42	0.37	0.55	0.31
Na2O	wt %	1.57	1.86	1.73	2.17	1.9	2.16	2	2.08	1.93
P2O5	wt %	0.09	0.06	0.07	0.06	0.1	0.07	0.06	0.08	0.08
LOI	wt %	1.31	1.23	0.85	1.08	1.16	1.31	1.18	1.39	1.16
SUM	wt %	99.26	99.06	98.27	98.68	99.4	100.02	99.04	99.21	99.17
Cr	ppm	230	349	241	107	415	237	183	215	396
Rb	ppm	23	24	5	5	5	14	17	5	17
Sr	ppm	361	348	339	294	334	337	340	370	352
Y	ppm	B/D	B/D	18	B/D	14	19	B/D	17	B/D
Zr	ppm	38	33	22	23	17	25	36	36	28
Nb	ppm	18	19	16	31	19	10	17	B/D	11
Ba	ppm	290	117	73	98	78	81	88	161	74

Meta Gabbro (ICP-MS)

ICP-MS										
Be	ppm	N/A	B/D	B/D	B/D	N/A	B/D	B/D	B/D	B/D
Sc	ppm	N/A	16.2	23.5	24.6	N/A	16.7	20.3	18.8	20.7
V	ppm	N/A	97.99	171.14	152.32	N/A	90.21	183.27	96.14	141.74
Rb	ppm	N/A	5.11	1.66	3.96	N/A	2.85	2.31	5.15	2.08
Sr	ppm	N/A	269.65	244.19	251.11	N/A	266.01	280.23	294.68	270.19
Y	ppm	N/A	4.76	8.43	7.11	N/A	4.18	5.47	5.27	5.49
Zr	ppm	N/A	19.33	13.47	14.56	N/A	16.63	23.3	18.7	13.33
Nb	ppm	N/A	1.54	1.58	1.47	N/A	1.17	1.42	1.95	1.20
Ce	ppm	N/A	0.28	0.08	0.22	N/A	0.30	0.11	0.30	0.14
Ba	ppm	N/A	115.64	74.41	89.72	N/A	66.00	61.90	151.46	65.74
La	ppm	N/A	3.23	3.37	3.80	N/A	2.69	2.74	3.39	2.98
Ce	ppm	N/A	6.85	8.32	8.68	N/A	6.39	6.68	8.21	7.14
Pr	ppm	N/A	0.95	1.20	1.15	N/A	0.85	0.91	1.08	1.00
Nd	ppm	N/A	4.18	6.16	5.41	N/A	4.10	4.63	5.01	4.62
Sm	ppm	N/A	0.95	1.60	1.49	N/A	0.94	1.14	1.16	1.25
Eu	ppm	N/A	0.33	0.56	0.57	N/A	0.40	0.46	0.44	0.46
Gd	ppm	N/A	1.11	1.98	1.75	N/A	1.06	1.34	1.23	1.26
Tb	ppm	N/A	0.17	0.28	0.24	N/A	0.14	0.18	0.19	0.20
Dy	ppm	N/A	1.11	1.88	1.66	N/A	0.93	1.29	1.25	1.33
Ho	ppm	N/A	0.21	0.39	0.31	N/A	0.19	0.25	0.24	0.27
Er	ppm	N/A	0.66	1.10	0.91	N/A	0.59	0.67	0.71	0.77
Tm	ppm	N/A	0.08	0.17	0.13	N/A	0.08	0.11	0.10	0.11
Yb	ppm	N/A	0.55	1.03	0.79	N/A	0.50	0.68	0.61	0.65
Lu	ppm	N/A	0.08	0.15	0.14	N/A	0.07	0.09	0.08	0.09
Hf	ppm	N/A	0.83	0.46	0.60	N/A	0.57	0.72	0.56	0.83
Ta	ppm	N/A	0.11	0.11	0.11	N/A	0.10	0.12	0.14	0.09
Th	ppm	N/A	0.50	0.37	0.49	N/A	0.26	0.28	0.44	0.56
U	ppm	N/A	0.14	0.19	0.16	N/A	0.10	0.11	0.16	0.12

Meta Gabbro (ICP-AES)

Ba	ppm	280	120	70	90	70	70	60	160	70
Be	ppm	0.5	0.25	0.25	0.25	0.25	0.25	0.25	0.25	0.25
Bi	ppm	1	1	1	1	1	1	1	1	1
Cd	ppm	0.25	0.5	0.25	0.5	0.5	0.5	0.5	0.5	1
Co	ppm	26	32	34	37	29	27	36	28	30
Cr	ppm	260	388	259	126	336	236	168	261	401
Cu	ppm	51	33	67	76	24	44	128	47	52
Ag	ppm	0.25	0.25	0.25	0.25	0.25	0.25	0.25	0.25	0.25
Mn	ppm	670	920	960	925	810	660	890	785	790
Mo	ppm	0.5	0.5	0.5	0.5	0.5	0.5	0.5	0.5	0.5
Ni	ppm	157	116	93	85	82	122	101	159	79
P	ppm	530	440	430	410	540	440	390	500	510
Pb	ppm	48	1	32	1	1	1	110	1	56
Sr	ppm	302	322	298	270	293	288	299	319	303
V	ppm	85	90	150	132	129	79	170	89	128
W	ppm	5	5	10	5	5	5	5	5	5
Zn	ppm	54	56	70	68	54	48	58	60	52

Host Rock (XRF)

Elements	UNITS	Z5-15 Sediment ?	Z2-PORPH Porphyry	Z2-12 Mafic dyke	GDCB Mafic dyke	Z2-14 Porphyry	POPPH-ZII Porphyry	Z210 Diorite	D1-CB Qtz diorite
SiO2	wt %	54.1	67.9	48.9	52.6	68.3	67.2	53.7	63.4
TiO2	wt %	0.98	0.39	0.67	0.71	0.38	0.39	0.85	0.6
Al2O3	wt %	14.7	16.1	15.5	14	15.8	16.2	16.5	17.8
Fe2O3	wt %	11.9	2.93	10.1	8.26	2.36	3.08	9.13	4.49
MnO	wt %	0.25	0.03	0.17	0.15	0.05	0.05	0.15	0.05
MgO	wt %	4.43	1.62	7.31	9.07	1.53	1.67	4.39	1.63
CaO	wt %	10	1.98	10.7	8.57	2.86	2.39	8.45	4.97
K2O	wt %	0.73	1.69	1.07	0.56	2.17	1.71	0.86	1.51
Na2O	wt %	0.69	5.83	2.44	2.93	5.06	5.89	3.24	4.68
P2O5	wt %	0.4	0.13	0.1	0.23	0.12	0.13	0.24	0.16
LOI	wt %	1.08	1.16	1.7	0.93	1.39	1.31	1	0.93
SUM	wt %	99.36	99.9	98.76	98.16	100.13	100.17	98.6	100.41
Cr	ppm	58	34	288	438	31	33	43	23
Pb	ppm	12	38	18	32	36	36	14	32
Sr	ppm	440	602	278	431	243	611	328	432
Y	ppm	19	B/D	16	19	B/D	12	20	18
Zr	ppm	21	107	43	92	103	101	53	384
Nb	ppm	11	13	B/D	B/D	12	12	23	17
Ba	ppm	232	409	131	195	562	474	260	676

Host Rock (ICP-MS)

Be	ppm	1.3	1.6	B/D	B/D	1.3	2.1	1.5	B/D
Sc	ppm	23.89	2.42	23.27	20.19	2.40	7.63	18.50	6.25
V	ppm	286.45	55.65	199.79	93.63	53.38	52.47	180.23	61.56
Pb	ppm	12.79	8.04	7.08	5.08	9.70	26.41	5.93	26.05
Sr	ppm	492.38	238.48	227.61	370.42	269.55	468.09	272.95	346.84
Y	ppm	15.33	1.57	13.14	7.79	2.79	7.06	11.63	12.03
Zr	ppm	16.66	102.53	17.69	11.17	107.88	105.71	16.01	114.84
Nb	ppm	3.00	4.16	2.49	1.43	3.96	4.53	5.59	6.99
Os	ppm	0.28	0.30	0.20	0.42	0.06	0.34	0.25	0.51
Ba	ppm	281.90	369.92	104.76	132.31	267.55	442.32	207.58	594.29
La	ppm	13.22	6.55	3.96	5.42	7.69	17.32	10.06	14.35
Ce	ppm	30.73	14.75	10.02	11.21	24.74	43.94	23.84	28.91
Pr	ppm	4.33	2.20	1.45	1.47	2.66	4.81	2.99	3.52
Nd	ppm	20.62	9.13	7.23	6.50	11.00	19.64	13.60	14.16
Sm	ppm	4.39	1.65	1.99	1.48	2.13	3.50	3.05	2.67
Eu	ppm	1.86	0.50	0.72	0.69	0.60	0.91	0.83	1.01
Gd	ppm	4.37	1.29	2.53	1.56	1.71	2.90	3.13	2.87
Tb	ppm	0.56	0.17	0.40	0.24	0.18	0.30	0.46	0.34
Dy	ppm	3.64	1.01	2.84	1.58	0.92	1.55	2.88	2.27
Ho	ppm	0.68	0.16	0.57	0.31	0.14	0.25	0.56	0.42
Er	ppm	1.83	0.47	1.68	0.78	0.37	0.70	1.56	1.39
Tm	ppm	0.26	0.07	0.25	0.13	0.06	0.10	0.22	0.20
Yb	ppm	1.76	0.46	1.55	0.85	0.31	0.62	1.33	1.32
Lu	ppm	0.23	0.05	0.24	0.13	0.05	0.10	0.21	0.23
Hf	ppm	0.81	4.90	0.54	0.52	3.24	3.14	0.60	2.78
Ta	ppm	0.20	0.39	0.18	0.09	0.23	0.27	0.39	0.48
Th	ppm	0.97	0.85	0.58	0.29	1.09	2.95	0.92	1.38
U	ppm	0.23	0.92	0.13	0.25	1.06	1.14	0.24	0.83

Host Rock (ICP-AES)

Ba	ppm	220	310	110	N/A	0.12	400	220	N/A
Be	ppm	0.25	1	0.5	N/A	0.1	1	0.5	N/A
Bi	ppm	1	1	1	N/A	0.52	1	1	N/A
Cd	ppm	0.25	0.25	0.5	N/A	0.25	0.25	0.5	N/A
Co	ppm	25	7	32	N/A	10	6	26	N/A
Cr	ppm	66	28	287	N/A	24	24	58	N/A
Cu	ppm	252	8	29	N/A	10	3	84	N/A
Ag	ppm	0.25	0.25	0.25	N/A	0.25	0.25	0.25	N/A
Mn	ppm	1675	180	1155	N/A	285	300	990	N/A
Mo	ppm	1	0.5	0.5	N/A	0.5	0.5	0.5	N/A
Ni	ppm	64	17	75	N/A	21	20	40	N/A
P	ppm	2070	670	570	N/A	700	700	1290	N/A
Pb	ppm	1	82	1	N/A	30	2	16	N/A
Sr	ppm	439	402	255	N/A	178	437	305	N/A
V	ppm	205	44	164	N/A	45	44	152	N/A
W	ppm	20	5	B/D	N/A	B/D	5	B/D	N/A
Zn	ppm	104	22	78	N/A	10	26	90	N/A

Host Rock (XRF)

Elements	UNITS	14Z5MS Sediment	Z51 Metsed	BSLT-CB Basalt	Z514 Mylonite	ID-CB Int. Dyke	RD-CB Ruptured Dyke	UM-CB Ultramafic	6BCB Gabbro
SiO2	wt %	55.2	52.3	51.2	55.7	61.1	51.9	40.3	54.9
TiO2	wt %	0.86	0.87	1.19	0.87	0.67	1.1	0.26	0.29
Al2O3	wt %	22	21.9	15.3	22.3	16.6	15.8	4.92	19.2
Fe2O3	wt %	12.2	13.3	12.7	11.4	6.05	12.5	13.9	5.67
MnO	wt %	0.05	0.09	0.2	0.06	0.08	0.19	0.15	0.09
MgO	wt %	1.79	1.94	4.81	1.51	3.34	5.39	27.7	5.23
CaO	wt %	0.99	1.06	10.5	0.93	6.2	9.88	2.89	9.56
K2O	wt %	3.68	4.14	0.65	3.53	1.01	0.37	0.02	0.55
Na2O	wt %	0.99	0.94	3.15	0.95	3.97	2.64	0.17	3.41
P2O5	wt %	0.42	0.45	0.28	0.44	0.26	0.26	0.05	0.1
LOI	wt %	1.7	1.93	0.54	1.93	0.77	0.54	9.39	0.93
SUM	wt %	100.05	99.11	100.63	99.8	100.23	100.63	100.14	100.04
Cr	ppm	22	23	69	20	67	59	2550	224
Pb	ppm	47	50	32	59	37	B/D	16	B/D
Sr	ppm	193	201	262	201	787	218	15	426
Y	ppm	B/D	14	14	B/D	B/D	12	B/D	B/D
Zr	ppm	34	10	52	53	118	47	22	56
Nb	ppm	23	17	13	20	29	B/D	18	17
Ba	ppm	1180	1320	498	1210	463	165	111	152

Host Rock (ICP-MS)

Be	ppm	N/A	B/D	B/D	B/D	B/D	B/D	N/A	B/D
Sc	ppm	N/A	19.4	36.8	12.6	12.9	30.4	N/A	12.8
V	ppm	N/A	263.96	307.71	204.98	107.77	229.16	N/A	149.59
Pb	ppm	N/A	31.58	5.29	11.94	22.01	3.06	N/A	3.81
Sr	ppm	N/A	141.85	281.44	132.66	656.10	228.66	N/A	325.75
Y	ppm	N/A	5.38	25.36	1.91	10.36	19.11	N/A	8.00
Zr	ppm	N/A	15.36	21.82	34.90	110.37	13.31	N/A	86.80
Nb	ppm	N/A	2.82	4.46	3.27	5.62	6.19	N/A	3.76
Cs	ppm	N/A	0.48	0.14	0.95	2.66	0.10	N/A	0.20
Ba	ppm	N/A	882.54	465.71	1793.60	395.27	125.06	N/A	143.94
La	ppm	N/A	2.68	12.28	5.63	19.20	11.43	N/A	22.35
Ce	ppm	N/A	6.13	28.77	15.71	42.16	24.92	N/A	49.74
Pr	ppm	N/A	0.87	4.01	2.40	5.39	3.27	N/A	6.26
Nd	ppm	N/A	4.22	18.45	11.44	21.96	14.48	N/A	25.54
Sm	ppm	N/A	1.14	4.24	2.64	4.01	3.23	N/A	4.38
Eu	ppm	N/A	0.49	1.43	0.87	1.18	0.89	N/A	1.14
Gd	ppm	N/A	1.30	4.63	2.18	3.30	3.87	N/A	3.27
Tb	ppm	N/A	0.18	0.72	0.29	0.41	0.55	N/A	0.39
Dy	ppm	N/A	1.07	5.01	1.71	2.24	3.55	N/A	2.23
Ho	ppm	N/A	0.23	1.00	0.31	0.39	0.77	N/A	0.41
Er	ppm	N/A	0.56	3.01	0.82	1.11	2.23	N/A	1.07
Tm	ppm	N/A	0.08	0.40	0.10	0.15	0.33	N/A	0.15
Yb	ppm	N/A	0.58	2.85	0.73	0.95	2.28	N/A	0.91
Lu	ppm	N/A	0.08	0.39	0.09	0.14	0.32	N/A	0.13
Hf	ppm	N/A	0.48	1.01	2.43	2.84	0.77	N/A	2.37
Ta	ppm	N/A	0.11	0.25	0.35	0.28	0.37	N/A	0.20
Th	ppm	N/A	0.52	0.66	0.58	2.17	0.77	N/A	1.82
U	ppm	N/A	0.13	0.45	0.26	1.86	0.40	N/A	1.62

Host Rock (ICP-AES)

Ba	ppm	980	1090	N/A	N/A	N/A	N/A	N/A	N/A
Be	ppm	0.25	0.25	N/A	N/A	N/A	N/A	N/A	N/A
Bi	ppm	1	1	N/A	N/A	N/A	N/A	N/A	N/A
Cd	ppm	0.25	0.25	N/A	N/A	N/A	N/A	N/A	N/A
Co	ppm	8	11	N/A	N/A	N/A	N/A	N/A	N/A
Cr	ppm	13	15	N/A	N/A	N/A	N/A	N/A	N/A
Cu	ppm	30	53	N/A	N/A	N/A	N/A	N/A	N/A
Ag	ppm	0.25	0.25	N/A	N/A	N/A	N/A	N/A	N/A
Mn	ppm	185	400	N/A	N/A	N/A	N/A	N/A	N/A
Mo	ppm	2	0.5	N/A	N/A	N/A	N/A	N/A	N/A
Ni	ppm	20	24	N/A	N/A	N/A	N/A	N/A	N/A
P	ppm	2120	2260	N/A	N/A	N/A	N/A	N/A	N/A
Pb	ppm	10	1	N/A	N/A	N/A	N/A	N/A	N/A
Sr	ppm	178	186	N/A	N/A	N/A	N/A	N/A	N/A
V	ppm	149	187	N/A	N/A	N/A	N/A	N/A	N/A
W	ppm	20	10	N/A	N/A	N/A	N/A	N/A	N/A
Zn	ppm	12	16	N/A	N/A	N/A	N/A	N/A	N/A

Core(XRF)

Elements	UNITS	S120-1	S120-17	S120-2	S120-3	S120-4	S120-18	S120-5	S120-6	S120-7	S120-8
Distance	metre	45.49	45.49	45.98	47.07	48.02	48.02	49.39	50.09	51.52	52.50
	feet	149.2	149.2	150.8	154.4	157.5	157.5	162	164.3	169	172.2
SiO2	wt %	44.3	47	55.3	56	59.3	51.3	40.6	42.2	71.6	50.5
TiO2	wt %	0.53	0.56	0.52	0.54	0.48	0.58	1.02	0.79	0.47	0.72
Al2O3	wt %	21.4	20.7	17.6	17.8	16.8	19.8	17.1	21.8	6.98	18.7
Fe2O3	wt %	9.27	8.42	7.5	7.04	5.62	7.15	9.45	8.37	4.39	8.02
MnO	wt %	0.17	0.14	0.11	0.1	0.1	0.12	0.17	0.17	0.09	0.14
MgO	wt %	6.2	5.54	3.8	3.81	3.59	4.7	6.59	5.63	2.84	4.46
CaO	wt %	9.45	7.84	7.14	7.88	6.91	8.07	12.8	10.6	6.54	8.78
K2O	wt %	3.69	4.61	3.06	2.28	2.84	3.58	4.45	4.04	1.43	2.37
Na2O	wt %	1.47	1.79	2.23	2.55	2.8	2.8	0.35	1.48	0.26	2.59
P2O5	wt %	0.17	0.17	0.14	0.14	0.13	0.14	0.18	0.21	0.11	0.2
LOI	wt %	1.62	1.23	1.31	0.54	1.31	1.23	7.16	3.85	3.62	2.39
SUM	wt %	98.27	98	98.71	98.68	99.88	99.47	99.87	99.14	98.33	98.87
Cr	ppm	89	34	14	11	13	25	193	13	12	16
Pb	ppm	55	44	45	39	29	42	56	60	25	31
Sr	ppm	352	324	304	415	306	295	229	346	110	376
Y	ppm	11	5	5	5	5	5	29	5	5	5
Zr	ppm	88	100	94	86	75	97	111	102	78	105
Nb	ppm	11	5	13	5	16	19	26	24	21	16
Ba	ppm	304	526	317	193	253	332	206	229	130	270

Core (ICP-MS)

Be	ppm	2.2	N/A	1.3	B/D	1.2	N/A	B/D	B/D	B/D	B/D
Sc	ppm	11.5	N/A	9.4	8.6	8.0	N/A	21.2	23.7	9.0	13.0
V	ppm	178.35	N/A	142.18	127.43	116.01	N/A	208.09	198.57	72.78	143.79
Pb	ppm	14.89	N/A	15.15	9.48	12.67	N/A	22.77	56.75	13.96	9.06
Sr	ppm	217.19	N/A	219.87	268.11	188.50	N/A	195.41	362.73	83.82	262.64
Y	ppm	5.66	N/A	4.94	3.99	4.03	N/A	18.38	10.55	6.39	5.23
Zr	ppm	76.24	N/A	56.88	56.97	36.45	N/A	61.65	46.11	36.93	42.00
Nb	ppm	3.55	N/A	3.46	3.77	3.15	N/A	6.84	5.34	1.59	6.21
Ce	ppm	0.42	N/A	0.27	0.18	0.25	N/A	0.61	2.09	0.39	0.28
Ba	ppm	268.28	N/A	250.61	131.90	210.59	N/A	241.35	294.39	116.75	302.75
La	ppm	8.41	N/A	6.14	4.99	4.26	N/A	8.89	6.32	3.63	6.32
Ce	ppm	21.82	N/A	14.26	12.28	10.75	N/A	21.21	13.95	7.05	14.40
Pr	ppm	2.63	N/A	1.72	1.32	1.24	N/A	2.87	1.81	0.88	1.78
Nd	ppm	11.51	N/A	7.71	5.81	5.73	N/A	13.91	8.30	4.09	7.64
Sm	ppm	2.13	N/A	1.48	1.23	1.26	N/A	3.00	1.87	0.83	1.62
Eu	ppm	0.79	N/A	0.63	0.52	0.43	N/A	0.99	0.76	0.46	0.63
Gd	ppm	2.01	N/A	1.54	1.33	1.20	N/A	3.42	2.17	1.03	1.72
Tb	ppm	0.26	N/A	0.22	0.18	0.16	N/A	0.56	0.33	0.14	0.26
Dy	ppm	1.54	N/A	1.26	1.11	1.10	N/A	3.86	2.36	1.11	1.84
Ho	ppm	0.30	N/A	0.26	0.21	0.21	N/A	0.76	0.44	0.27	0.36
Er	ppm	0.85	N/A	0.71	0.61	0.60	N/A	2.30	1.42	0.86	1.05
Tm	ppm	0.12	N/A	0.10	0.08	0.09	N/A	0.35	0.18	0.14	0.14
Yb	ppm	0.73	N/A	0.64	0.56	0.54	N/A	2.02	0.98	0.89	0.77
Lu	ppm	0.10	N/A	0.09	0.08	0.07	N/A	0.29	0.16	0.15	0.12
Hf	ppm	1.97	N/A	1.47	1.87	0.94	N/A	1.55	1.05	1.31	1.82
Ta	ppm	0.28	N/A	0.26	0.23	0.18	N/A	0.37	0.28	0.18	0.50
Th	ppm	0.90	N/A	0.48	0.73	0.59	N/A	0.66	0.53	0.60	0.54
U	ppm	0.59	N/A	0.30	0.29	0.31	N/A	0.57	0.38	0.24	0.41

Core(ICP-AES)

Ba	ppm	310	500	260	160	240	310	230	260	110	240
Be	ppm	0.25	0.25	0.25	0.25	0.25	0.25	0.25	0.25	0.25	0.25
Bi	ppm	1	1	1	1	1	1	1	1	1	1
Cd	ppm	0.5	0.5	0.25	0.5	0.25	0.25	0.5	0.5	0.25	0.25
Co	ppm	27	14	28	23	13	12	12	19	22	43
Cr	ppm	100	44	19	20	20	26	241	33	18	26
Cu	ppm	46	32	159	45	2	0.5	0.5	21	21	55
Ag	ppm	0.25	0.25	0.25	0.25	0.25	0.25	0.25	0.25	0.25	0.25
Mn	ppm	1045	910	700	655	650	780	1210	1100	620	930
Mo	ppm	0.5	1	1	0.5	2	3	3	1	0.5	1
Ni	ppm	79	67	40	40	33	50	58	42	23	72
P	ppm	840	880	740	740	740	810	950	1120	590	1080
Pb	ppm	1	4	2	1	4	2	1	4	1	8
Sr	ppm	298	277	253	361	260	261	220	322	87	319
V	ppm	139	137	114	110	106	122	170	167	64	122
W	ppm	60	20	10	5	10	20	30	30	5	5
Zn	ppm	48	84	34	52	30	36	56	38	28	46

Core(XRF)

Elemets	UNITS	S120-9	S120-10	S120-11	S120-12	S120-19	S120-13	S120-14	S120-15	S120-20	S120-16
Distance	metre	53.51	54.12	54.19	54.42	54.42	55.37	56.77	57.32	57.32	58.23
	feet	175.5	177.5	177.75	178.5	178.5	181.6	186.2	188	188	191
SIC2	wt %	26	51.2	49.7	50.6	49.8	45.3	55.3	47.8	54.6	51.5
TiO2	wt %	0.8	0.65	0.63	0.88	0.72	0.57	0.41	0.76	0.43	0.66
AL2O3	wt %	16.4	15	16.5	15.3	15.1	13.3	12.2	14.1	10.2	12.4
FE2O3	wt %	13	9.49	10.1	10.6	10.6	11.5	9.74	11.3	12.2	10.7
MNO	wt %	0.21	0.14	0.16	0.17	0.18	0.18	0.14	0.17	0.18	0.16
MGO	wt %	9.91	7.27	7.92	7.75	8.63	13.5	9.73	11.8	10.9	11.2
CAO	wt %	13.4	9.5	10.5	10.1	10.4	8.92	7.26	9.61	7.31	9.03
K2O	wt %	6.21	3.21	1.59	0.76	0.63	2	0.31	0.49	0.27	0.34
NA2O	wt %	0.19	1.5	1.58	2.37	2.5	1.06	2.53	1.68	1.91	1.54
P2O5	wt %	0.13	0.09	0.09	0.13	0.12	0.09	0.04	0.12	0.04	0.1
LOI	wt %	11.6	1.7	0.7	0.77	0.7	1.62	0.85	1.08	0.7	0.93
SUM	wt %	97.85	99.75	99.47	99.43	99.38	98.04	98.51	98.91	98.74	98.56
Cr	ppm	420	245	255	285	333	1090	999	896	1140	826
Pb	ppm	62	33	41	28	26	43	14	5	5	24
Sr	ppm	138	205	253	222	212	94	164	170	81	120
Y	ppm	14	5	5	25	21	35	28	11	37	10
Zr	ppm	39	63	53	61	65	33	141	36	344	38
Nb	ppm	5	15	5	17	16	5	15	20	15	22
Ba	ppm	517	269	225	274	251	408	142	112	148	96

Core (ICP-MS)

	B/D	B/D	B/D	B/D	N/A	B/D	B/D	B/D	N/A	B/D
Be	ppm	B/D	B/D	B/D	N/A	B/D	B/D	B/D	N/A	B/D
Sc	ppm	27.1	32.3	29.0	27.2	N/A	14.0	21.4	24.6	N/A
V	ppm	163.17	176.71	164.06	233.55	N/A	131.41	105.75	176.34	N/A
Pb	ppm	32.10	34.19	20.22	4.78	N/A	7.81	2.05	2.75	N/A
Sr	ppm	125.32	206.25	246.82	180.70	N/A	51.48	158.61	134.29	N/A
Y	ppm	15.00	16.79	13.77	17.57	N/A	6.78	22.57	13.42	N/A
Zr	ppm	36.24	38.69	28.78	42.71	N/A	27.23	58.94	32.46	N/A
Nb	ppm	3.75	2.90	2.08	3.79	N/A	1.49	3.09	2.33	N/A
Cs	ppm	0.99	0.66	0.52	0.08	N/A	0.34	0.09	0.14	N/A
Ba	ppm	595.16	241.24	259.37	274.97	N/A	345.42	104.59	80.09	N/A
La	ppm	3.04	5.19	3.68	4.90	N/A	2.03	5.94	3.33	N/A
Ce	ppm	5.16	12.37	9.14	12.82	N/A	6.17	15.06	9.38	N/A
Pr	ppm	0.67	1.71	1.30	1.88	N/A	0.91	2.29	1.45	N/A
Nd	ppm	3.39	8.25	6.70	9.31	N/A	4.71	11.83	7.31	N/A
Sm	ppm	0.89	2.24	1.80	2.67	N/A	1.24	3.57	2.06	N/A
Eu	ppm	0.32	0.75	0.67	0.88	N/A	0.43	0.81	0.60	N/A
Gd	ppm	1.76	2.71	2.49	3.27	N/A	1.61	4.27	2.56	N/A
Tb	ppm	0.32	0.45	0.40	0.53	N/A	0.25	0.67	0.42	N/A
Dy	ppm	2.77	3.29	2.79	3.75	N/A	1.67	4.68	2.87	N/A
Ho	ppm	0.62	0.70	0.58	0.77	N/A	0.34	0.94	0.59	N/A
Er	ppm	1.87	2.11	1.72	2.30	N/A	0.99	2.89	1.74	N/A
Tm	ppm	0.27	0.32	0.26	0.34	N/A	0.15	0.41	0.26	N/A
Yb	ppm	1.71	2.08	1.76	2.07	N/A	0.84	2.53	1.59	N/A
Lu	ppm	0.23	0.32	0.26	0.32	N/A	0.13	0.36	0.24	N/A
Hf	ppm	1.08	1.44	0.82	1.29	N/A	0.96	1.84	1.03	N/A
Ta	ppm	0.26	0.26	0.20	0.23	N/A	0.11	0.26	0.17	N/A
Th	ppm	0.40	0.67	0.59	0.42	N/A	0.36	2.01	0.37	N/A
U	ppm	0.26	0.28	0.24	0.26	N/A	0.12	0.75	0.21	N/A

Core(ICP-AES)

Ba	ppm	530	220	250	250	210	370	100	80	80	60
Be	ppm	0.25	0.25	0.25	0.25	0.25	0.25	0.25	0.25	0.25	0.25
Bi	ppm	1	1	1	1	1	1	1	1	1	1
Cd	ppm	0.25	0.25	0.25	1	0.25	0.5	0.25	0.25	0.25	0.25
Co	ppm	14	33	37	37	38	56	42	51	48	47
Cr	ppm	420	262	277	304	359	1231	1026	1187	920	881
Cu	ppm	225	15	28	165	52	0.5	16	258	5	22
Ag	ppm	0.25	0.25	0.25	0.25	0.25	0.25	0.25	0.25	0.25	0.25
Mn	ppm	1445	960	995	1095	1180	1270	940	1225	1115	1070
Mo	ppm	2	0.5	1	0.5	1	0.5	2	1	1	0.5
Ni	ppm	128	97	123	113	144	389	333	408	299	282
P	ppm	690	530	540	690	630	490	250	250	600	540
Pb	ppm	1	52	1	2	1	1	12	10	1	24
Sr	ppm	138	191	244	206	196	84	157	93	160	125
V	ppm	130	150	141	179	173	125	89	108	150	137
W	ppm	20	10	10	5	10	5	5	10	10	5
Zn	ppm	94	76	98	94	94	134	86	114	90	84

Note: N/A=not available; B/D=Below Detection

**Appendix F: Summary of trace element data for mineral
seperates**

ICP-MS Analyses on selected Minerals

Elements	units	Chalcopyrite	Pyrite	Pyrrhotite
Be	ppm	B/D	B/D	B/D
Sc	ppm	B/D	B/D	B/D
V	ppm	6.11	8.67	9.71
Rb	ppm	B/D	B/D	B/D
Sr	ppm	0.58	B/D	0.61
Y	ppm	0.02	0.04	0.05
Zr	ppm	0.11	0.12	0.09
Nb	ppm	0.03	0.04	0.03
Cs	ppm	0.06	B/D	B/D
Ba	ppm	0.16	0.07	0.09
La	ppm	B/D	0.15	B/D
Ce	ppm	0.03	0.28	B/D
Pr	ppm	B/D	0.03	B/D
Nd	ppm	0.03	0.1	B/D
Sm	ppm	B/D	B/D	B/D
Eu	ppm	B/D	B/D	B/D
Gd	ppm	B/D	B/D	B/D
Tb	ppm	B/D	B/D	B/D
Dy	ppm	B/D	B/D	B/D
Ho	ppm	B/D	B/D	B/D
Er	ppm	B/D	B/D	B/D
Tm	ppm	B/D	B/D	B/D
Yb	ppm	0.06	0.03	0.02
Lu	ppm	B/D	B/D	B/D
Hf	ppm	0.05	B/D	B/D
Ta	ppm	B/D	B/D	B/D
Th	ppm	0.02	B/D	B/D
U	ppm	0.01	0.04	0.01

Note: all samples are from 2B 100 stope
 B/D=Below Detection

Appendix G: Summary of fluid inclusion data

Fluid inclusion measurements for vein quartz from the Seabee gold deposit. Temperatures are in °C, and salinities are in % eq.NaCl

Sample no.	Origin	Type	Degree of filling	Vol percent CO ₂	T _{mCO₂}	T _{m_{ice}} T	Salinity	T _{hCO₂}	Density CO ₂	T _h	Bulk density	X _{H₂O}	X _{CO₂}	X _{NaCl}
Zone 2 (Z2-7) Surface														
Z2-7(1)	SP/S	Ia		100	?			33.6	?					
Z2-7(2)	SP/S	Ia		100	-59.2			?						
Z2-7(3)	SP/S	Ic		80	-54.2	-2.0*	3.3*	27.7	.663		.734	.437	.522	.005
Z2-7(4)	SP/S	Ia		100	-55.2			24.3	.773					
Z2-7(5)	SP/S	Ic		75	-55.2	-1.5*	2.5*	27.0	.678		.946	.426	.533	.004
Z2-7(6)	SP/S	Ic		70	-55.2	-1.6*	2.6*	27.7	.663		.950	.525	.471	.004
Z2-7(8)	SP/S	Ic		75	-55.2	-1.7*	2.8*	27.6	.665		.971	.443	.533	.024
Z2-7(9)	SP/S	Ia		100	-57.0			24.4	.720					
Z2-7(10)	SP/S	Ib	75			-2.8	4.5							
Zone 2 (S-133 281.0) Drill Core														
S-133(1)	SP/S	Ib	80			-1.3	2.1				209			
S-133(2)	SP/S	Ib	75			-1.2	2.0				235			
S-133(3)	SP/S	Ib	75			-1.2	2.0				316			
S-133(4)	SP/S	Ib	80			-0.9	1.5				366			
S-133(5)	SP/S	Ib	95			-1.4	-6.9 2.3				271			
S-133(6)	SP/S	Ib	97			-1.5	-10.0 2.5				354			
S-133(7)	SP/S	Ia		100	-54.0			27.7	.663					
S-133(8)	SP/S	Ib	86			-1.2	2.0				354			
Zone 5 (Z5-4) Surface														
Z2-5(1)	SP/S	Ia		100	-57.8			24.4	.720					
Z2-5(2)	SP/S	Ib	80			-4.2	6.7							
Z2-5(3)	SP/S	Ia		100	-58.0			22.0	.747					
Z2-5(4)	SP/S	Ib	75			-3.0	4.9							
Z2-5(5)	SP/S	Ib	78			-3.0	4.9							
Z2-5(6)	SP/S	Ib	73			-4.8	7.5							
Z2-5(7)	SP/S	Ib	83			-4.8	7.5							
Z2-5(8)	SP/S	Ia		100	-58.8			19.4	.781					
Z2-5(9)	SP/S	Ia		100	?			?						
Z2-5(10)	SP/S	Ia		100	-56.9			18.5	.791					
Z2-5(11)	SP/S	Ia		100	-56.8			18.0	.795					
Z2-5(12)	SP/S	Ia		100	-56.7			18.0	.795					
Z2-5(13)	SP/S	Ia		100	-56.6			18.2	.793					
Z2-5(14)	SP/S	Ib	90			-3.8	6.0							
Z2-5(15)	SP/S	Ib	86			-4.0	6.4							
Z2-5(16)	SP/S	Ib	74			-3.6	5.8							

* T_m ice may represent T_m clath, thus calculated salinities may be significantly higher.

Appendix H: Summary of stable isotope data

Table of stable isotopic values of various mineral phases from the Seabee deposit

Sample no.	$\delta^{18}\text{O}$ (quartz)	$\delta^{18}\text{O}$ (mineral)	$\delta\text{D}_{(\text{tourm})}$ (wt % H_2O)	$\delta^{13}\text{C}$ (mineral)	$\delta^{34}\text{S}$ (sulfide)	Equilibration Temperature ($^{\circ}\text{C}$)	Calculated $\delta^{18}\text{O}(\text{H}_2\text{O})$	Calculated $\delta\text{D}(\text{H}_2\text{O})$
Zone 2								
100stp-Vein	9.8(ore)	6.7(tour-unalt)	-50(3.28)		-0.9(py)	334(1)	4.0(2)	-13(3)
	9.4(ore)	7.8(tour-alt)		2.4(py)	636(1)	8.7(2)	-54(3)	
	9.5(ore)	6.5(tour-unalt)		2.3(py)	345(1)	4.1(2)	-16(3)	
	9.5(ore)	6.9(tour-unalt)		2.7(po)	399(1)	5.4(2)	-27(3)	
				2.5(py)				
		2.8(po)						
100stp-Micro	10.6(ore)	21.6(cal-white)		-11.2(cal)	3.7(cpy)			
		21.6(cal-white)		-11.2(cal)	3.6(cpy)			
		21.7(cal-white)		-11.3(cal)	2.6(cpy)			
		21.6(cal-white)	-11.3(cal)	3.5(cpy)				
			3.7(cpy)					
		2.5(cpy)						
		3.5(cpy)						
325stp		8.5(cal-pink)		-7.7(cal)				
		8.4(cal-pink)		-7.8(cal)				
		8.7(cal-pink)		-7.8(cal)				
		8.4(cal-pink)		-7.5(cal)				
Z2-1	10.0(ore)	7.2(tour-alt)	-61(3.31)			371(1)	5.3(2)	-24(3)
		7.6(tour-alt)	-66(3.30)			432(1)	6.6(2)	-40(3)
		7.2(tour-alt)				371(1)	5.3(2)	-24(3)
Z2-9	9.3(ore)							
S-133 281.0	9.8(ore)							
S-133 268.4					3.5(po)			
					2.4(po)			
					3.4(po)			
S-143 180.5	9.8(ore)							
S-124 243.5	9.5(ore)				3.6(po)			
S-126 299.5	9.7(ore)				2.8(py)			
293.5					3.4(po)			
S-129 141.7					1.2(py)			
S-128 120.1					3.2(py)			
H-36					3.3(po)			

Note: tour=tourmaline; alt=altered; unalt=unaltered; cal=calcite; po=pyrrhotite; py=pyrite; cpy=chalcopyrite; 1= temperature calculated from fractionation factor derived by Kotzer et al., 1994; 2= $\delta^{18}\text{O}_{\text{water}}$ calculated from quartz-water fractionation factor derived by Bottinga and Javoy, 1973; 3= $\delta\text{D}_{\text{water}}$ calculated from tourmaline-water fractionation factor derived by Kotzer et al., 1994.

Table of stable isotopic values of various mineral phases from the Seabee deposit

Sample no.	$\delta^{18}\text{O}$ (quartz)	$\delta^{18}\text{O}$ (mineral)	$\delta^{13}\text{C}$ (mineral)	$\delta\text{D}_{(\text{tourm})}$ (wt % H_2O)	Equilibration Temperature ($^{\circ}\text{C}$)	Calculated $\delta^{18}\text{O}_{(\text{H}_2\text{O})}$	Calculated $\delta_{(\text{H}_2\text{O})}$
Zone 2							
2B S-223 219.6-220.1	9.0(ore)						
2HS-236 321.5-322	10.5(ore)						
2C S-236 521.8-522.2	9.2(sub)	7.5(tour-alt)			600(1)	8.2(2)	
	9.3(sub)						
2H S-236 539.6-543.8	9.5(sub)						
2B S-236 539.6-543.6	9.3(sub)	7.2(tour-alt)			491(1)	6.9(2)	
2H Dp#4		8.5(cal-pink)	-7.5(cal-pink)				
		8.9(cal-pink)	-5.9(cal-pink)				
Zone 5							
Z5-2	10.2(ore)						
S-237 28.7-32.8	9.7 (ore)	7.6(tour-alt)		-80(2.2)	491(1)	7.3(2)	-62(3)
Zone 10							
Z10-1	9.7(ore)						
Zone 11							
S-231 83.7	9.0(sub)	9.5(feld)					
		9.6(feld)					
Zone 14							
S-231 158.7-159.2	9.0(sub)	8.9(feld)					
Zone 15							
S-215 65.0 67.0	9.3(sub)						
Zone 666							
S-236 98.3-99.3	8.9(bar)						
East boundary Zone							
Splay A							
S-196 44.04-44.4	10.6(unt)						
	10.4(unt)						
Splay C							
S-196 102.4-102.8	8.4(bar)						

Note: bar=barren; unt=untested; sub=subeconomic; tour=tourmaline; alt=altered; unalt=unaltered; feld=feldspar; cal=calcite; 1= temperature calculated from fractionation factor derived by Kotzer et al., 1994; 2= $\delta^{18}\text{O}_{\text{water}}$ calculated from quartz-water fractionation factor derived by Bottinga and Javoy, 1973; 3= $\delta\text{D}_{\text{water}}$ calculated from tourmaline-water fractionation factor derived by Kotzer et al., 1994.

Appendix I: Summary of radiogenic isotope data

Lead evaporation data on zircons for feldspar porphyry

Sample	Step	Pb ²⁰⁷ /Pb ²⁰⁶ 2σ	Age +/-	Fillament (amp)	Temp. (C°)
FP#2	1	0.1147945 80	1877 13	1.7750	1200
	2	0.1150263 32	1866 4	2.2830	1460
FP#1	2	0.1143554 116	1870 19	2.2850	1460
	3	0.1145278 171	1872 28	2.5000	1500
FP#3	2	0.1146460 116	1874 19	2.2000	1425
	3	0.1146885 110	1875 18	2.3000	1460
FP#10	3	0.1159106 129	1894 21	2.4000	1475
	4	0.1169792 86	1911 14	2.5000	1500

⁸⁷Sr/⁸⁶Sr ratios of selected mineral separates

Sample	Mineral	⁸⁷ Sr/ ⁸⁶ Sr	+/- (2σ)
S-126 293.6	pyrrhotite	0.711093	87
H-36	pyrrhotite	0.707155	108
Z2-2	dark tourmaline	0.701911	23
Cpy-4 (100stp)	chalcopyrite	0.709213	74
Au 8 (100stp)	gold	0.70462	1252